

UNIVERSITY OF OKLAHOMA
GRADUATE COLLEGE

QUANTIFYING PARTICLE TRANSPORTATION FOR UNCONVENTIONAL
RESERVOIR CHARACTERIZATION

A DISSERTATION
SUBMITTED TO THE GRADUATE FACULTY
in partial fulfillment of the requirements for the
Degree of
DOCTOR OF PHILOSOPHY

By
WEI TIAN
Norman, Oklahoma
2017

QUANTIFYING PARTICLE TRANSPORTATION FOR UNCONVENTIONAL
RESERVOIR CHARACTERIZATION

A DISSERTATION APPROVED FOR THE
MEWBOURNE SCHOOL OF PETROLEUM AND GEOLOGICAL ENGINEERING

BY

Dr. Xingru Wu, Chair

Dr. Jeffrey H. Harwell

Dr. Bor-Jier (Ben) Shiau

Dr. Ahmad Jamili

Dr. Rouzbeh G. Moghanloo

© Copyright by WEI TIAN 2017
All Rights Reserved.

DEDICATION

I dedicate this dissertation to my wonderful parents Lun Tian and Wanqin Zhang,

my perfect wife Tong Shen

my beloved dog Ginger.

For all your companion, love, support and patience.

Acknowledgements

My foremost gratitude goes to my advisor Dr. Xingru Wu for his inspiration, encouragement, patience and instruction in my research and daily life. He directed me to grow up in academia and become a professional researcher. It was my great pleasure to work with Dr. Wu. His guidance benefited me in the past and will lead me in the years to come. I would also like to thank Dr. Rouzbeh G. Moghanloo for friendship, experience and knowledge. I do appreciate his advice and creative thinking.

My gratitude also extends to other committee members, Dr. Jeffrey Harwell, Dr. Benjamin Shaiu and Dr. Ahmad Jamili as well as former committee member Dr. Maysam Pournik. I thank you all for taking time to supervise my research work and provide insightful comments and suggestions.

I am indebted to Dr. Carl Sondergeld for offering the opportunity to work with your group in my radon project. It cannot succeed without your input. Thanks also goes to Dr. Junrong Liu and Dr. Kegang Ling for collaborating on various research projects.

I want to express my sincere gratitude to my colleagues. Thank you Sumeer Kalra, Zhenyu Zhang, Changlong Chen, Amanda Knaup, and Ali Tinni for their significant contributions to my research. I would also like to thank my friends for making my journey at University of Oklahoma enjoyable and memorable.

My special thank goes to my wife Tong Shen. Her accompany, support and love made this dissertation possible. She took good care of my daily life so that I can concentrate on my research work. I also want to thank my parents and family for their endless love and support.

Table of Contents

Acknowledgements	iv
Table of Contents	v
List of Tables	ix
List of Figures.....	x
Abstract.....	xvi
Chapter 1. Introduction	1
1.1 Research Motivations	1
1.2 Research Objectives	2
1.3 Chapter Layout	3
Chapter 2. Improved Method of Moments to Determine Mobile Phase Saturations with Single Well Chemical Tracer Test	5
2.1 Introduction	5
2.2 Modified SWCTT and MoM.....	8
2.2.1 Modified Procedure of SWCTT.....	8
2.2.2 Movement of Tracers	9
2.2.3 Modified MoM.....	13
2.3 Method Validation and Comparison	15
2.3.1 Model Description	15
2.3.2 Analysis Procedure.....	19
2.3.3 Saturation Estimation	21
2.3.4 Comparison with Conventional Interpretation Methods	22
2.3.5 Comparison with Conventional SWCTT Procedure	24

2.4	Impacting Factor Analysis.....	26
2.4.1	Impact of Variable Production Rate	26
2.4.2	Impact of Heterogeneous Permeability	31
2.4.3	Impact of Heterogeneous Oil Saturation	32
2.4.4	Impact of Dispersion	34
2.5	Conclusions	35
	Nomenclature	36
Chapter 3.	Estimation of Hydraulic Fracture Volume utilizing Partitioning Chemical Tracer in Shale Gas Formation.....	38
3.1	Introduction	38
3.2	Methodology.....	39
3.2.1	Swept Volume Calculation.....	40
3.2.2	Exponential Decline	41
3.3	Validation and Discussion.....	41
3.3.1	Hydraulic Fracture Volume Estimation.....	41
3.3.2	Matrix Impact	48
3.3.3	Impact of Partition Coefficient (K)	56
3.3.4	Impact of Adsorption.....	61
3.4	Conclusion.....	64
	Nomenclature	66
Chapter 4.	Random Walk Algorithm to Track Partitioning Tracer Movement	68
4.1	Introduction	68
4.2	Algorithm Description.....	68

4.3	Program Validation and Result	71
4.3.1	Model Description	71
4.3.2	Validation	73
4.3.3	Partitioning Tracer Movement with Two Mobile Phases.....	75
	Nomenclature	76
Chapter 5.	Quantitative Estimation of Radon Production from Marcellus Shale Gas Reservoirs.....	78
5.1	Introduction	78
5.2	Marcellus Shale	81
5.2.1	Porous Media.....	81
5.2.2	Experimental Methods.....	83
5.2.3	Pore Characterization	84
5.3	Radon Generation in Pore Space	87
5.3.1	Recoil Range	87
5.3.2	Slit Shape Pores	87
5.3.3	Spherical Pores	89
5.4	Radon Transport	93
5.5	Model Description	94
5.6	Result and Discussion.....	98
5.6.1	In-situ Radon Concentration.....	98
5.6.2	Wellhead Radon Concentration.....	99
5.6.3	Impact of Spatial Distribution of Pore Size.....	102
5.6.4	Impact of Natural Fracture	104

5.6.5	Sensitivity Analysis	105
5.6.6	Discussion.....	111
	Nomenclature	115
Chapter 6.	Conclusions and Recommendations.....	117
6.1	Conclusions	117
6.2	Recommendations for Future Work	119
	References	120
	Appendix A: Derivation of Modified MoM.....	129
	Appendix B: Simulation Input File for SWCTT	135

List of Tables

Table 2-1. Input parameters in the numerical simulation.....	18
Table 2-2. Proposed approach verification through modified SWCTT procedure	21
Table 2-3. Result comparison with conventional interpretation methods.....	24
Table 2-4. Oil saturation evaluated through conventional SWCTT procedure and conventional methods.....	26
Table 2-5. Sensitive analysis results of Case 13 to Case 17, compared with base case (Case 3).....	30
Table 3-1. Generic Hydraulic Fracture Properties	42
Table 3-2. Well Constraints and Fluid Properties	44
Table 3-3. Model Dimensions and Matrix Properties	49
Table 3-4. Swept Volume Comparison	52
Table 3-5. Comparison of Swept Volume with Different Partition Coefficient	57
Table 3-6. Comparison of Swept Volume with Different Adsorption Parameter	62
Table 4-1. Input parameters of base case	72
Table 5-1. Uranium Concentration in Different Rocks (Andrews and Wood 1972).	80
Table 5-2. Simulation input parameters of base case	97
Table 5-3. Radon in-situ concentration	100
Table 5-4. Radon in-situ concentration in near fracture zone and far formation zone for Case D and Case E.	103
Table 5-5. Varied parameters for sensitivity analysis	106

List of Figures

Figure 2-1. Procedure of conventional SWCTT.....	6
Figure 2-2. At the end of injection of pusher. Alcohol moves faster than ester so that alcohol travels farther than ester.....	11
Figure 2-3. At the end of shut in period. Ester reacts with water generating alcohol. Both of ester and alcohol remains stationary.	12
Figure 2-4. During the production period. Alcohol travels faster than ester and its production will be observed at first.	12
Figure 2-5. A schematic illustration of concentration of alcohol and ester in water at the end of shut in. Alcohol concentration peak position collapsed with ester concentration peak.....	13
Figure 2-6. Cylindrical domain of reservoir. Injector and producer are located at the center. Saturation is spatially constant.	16
Figure 2-7. Relative Permeability Curve.....	16
Figure 2-8. Production history of tracers for Case 1.	19
Figure 2-9. Water production rate and tracer production history for Case 7. Conventional SWCTT and initial oil saturation was 0.9.....	25
Figure 2-10. Water production rate and tracer production history for Case 13. Variable liquid production rate under a constant BHP constraint.....	28
Figure 2-11. Heterogeneous permeability field, zoom in near wellbore. Mean=1000 md, $V_{Dp}=0.5$	32
Figure 2-12. Heterogeneous oil saturation field, zoom in near wellbore. Mean = 0.7, std=0.15.	33

Figure 2-13. Oil production rate and tracer production history for Case 15. Heterogeneous oil saturation.	34
Figure 2-14. Conservative tracer (alcohol) production history comparison.....	35
Figure 3-1. Illustration of hydraulic fracture configuration. Each grid is 1 ft long. There are 300 grids and the well perforates at one end.	42
Figure 3-2. The four steps of well plan	43
Figure 3-3. Relative permeability curves in matrix and hydraulic fracture (modified from Cheng (2012)).....	45
Figure 3-4. Tracer concentration vs. cumulative gas production. The dashed line is the best fitted line. Its R-square is 0.983, indicating the tracer tail is almost a straight line.	46
Figure 3-5. Tracer distribution inside fracture at the end of shut in.....	47
Figure 3-6. Synthetic model configuration with hydraulic fracture and matrix. The hydraulic fraction is on the right side with red color. The horizontal well perforates in the upper right grid. The matrix is in the blue color.....	49
Figure 3-7. Partitioning tracer production in gas.....	50
Figure 3-8. Partitioning tracer production data in gas. Solid lines are simulation output. The dashed lines are the extrapolation based on the first linear section. x axis is normal scale and y axis is in log scale.....	54
Figure 3-9. The volume contacted with tracer at the end of shut in. R=200000.	54
Figure 3-10. The volume contacted with tracer at the end of shut in. R=20000.	55
Figure 3-11. The volume contacted with tracer at the end of shut in. R=2000.	55

Figure 3-12. Partitioning chemical tracer production data in gas. Solid lines are simulation output. The dashed lines are the extrapolation based on the first linear section. This figure shows the difference between the cases with different partition coefficient (K). x axis is normal scale and y axis is in log scale. 57

Figure 3-13. The tracer distribution profile inside domain at the end of shut in. K=2.5.58

Figure 3-14. The tracer distribution profile inside domain at the end of shut in. K=25. 58

Figure 3-15. The tracer distribution profile inside domain at the end of shut in. K=250. 59

Figure 3-16. Fracking fluid (water) distribution at the end of shut in. Inside hydraulic fracture grid column (x=18). 61

Figure 3-17. Partitioning chemical tracer production data in gas. Solid lines are simulation output. The dashed lines are the extrapolation based on the first linear section. This figure shows the difference between the cases with different adsorption. 62

Figure 3-18. The tracer distribution profile inside domain at the end of shut in. Medium adsorption. 63

Figure 3-19. The tracer distribution profile inside domain at the end of shut in. High adsorption. 63

Figure 4-1. Particle movement is consisted by advection and diffusion (Yi et al. 1994). 69

Figure 4-2. Linear interpolation to calculate particle velocity (modified from LaBolle et al. 1996). 70

Figure 4-3. Configuration of 1D model. The partitioning chemical tracer is injected from left to right. Its concentration is recorded at the outlet. 71

Figure 4-4. Relative permeability curve. 72

Figure 4-5. Comparison of RWPT with analytical solution and finite-difference. Peclet number is infinity (base case). Immobile oil. 74

Figure 4-6. Comparison of RWPT with analytical solution and finite-difference. Peclet number is 45. Immobile oil. 74

Figure 4-7. Comparison of RWPT with finite-difference. Peclet number is 45. Mobile oil. 75

Figure 5-1. Radioactive decay process from Uranium to Lead (modified from Allthingsradon (2009)) 79

Figure 5-2. Gas is stored in spherical pores (the red color) and water is in slit pores (the blue color) (Passey et al. 2010). 82

Figure 5-3. Backscattered SEM images for Marcellus shale. (a) Shows organic and inorganic pores at 3 μm . The inorganic pores show slit shape and organic pores shows spherical shape. In (b), the image shows more slits and sheets of illite. Illite is the dominant matrix mineral and is more visible as sheets in (c) and (d), creating inorganic pores around the sample. 84

Figure 5-4. Pore size distribution for Marcellus shale. Case A and Case B are calculated through DFT using the adsorption measurements. Case C is obtained from literature (Chalmers et al. 2012). 86

Figure 5-5. Radon escapes from pores into grains. The pore diameter is d and radon recoil length is R_f . When radon particle is ejected into the section of ABC or EFD, it is regarded as being escaped into grains from pore space. 89

Figure 5-6. Schematic cross-section view of spherical pore shape. The radon generated from radium in grains may enter the pore space. O_2A section has length of a . AB section has length of b . O_2C section has length of x 91

Figure 5-7. Schematic cross-section view. Radon generated from radium in pore space may remain in pore space. 92

Figure 5-8. Radon transport process from porous media to residential users. Green dots represent radon particles. 94

Figure 5-9. Model configuration. (a) is for the base case. (b) is the case with manually created natural fractures. The black color represents hydraulic fracture and natural fractures. The gray color represents the wellbore. 96

Figure 5-10. Radon total in-situ concentration for the three cases. 99

Figure 5-11. Wellhead radon concentration with multiple initial radon in-situ concentrations. Wellhead radon concentration is directly related with the in-situ concentration 101

Figure 5-12. Synthetic model configuration. The horizontal well is located at the top. It is perforated at hydraulic fracture at the left side. The stimulate reservoir is divided into two sections: near fracture zone and far formation zone. 102

Figure 5-13. Wellhead radon concentration to investigate heterogeneity impact. Near fracture zone determines the early radon production. 104

Figure 5-14. Radon wellhead concentration from simulation output..... 105

Figure 5-15. Relative permeability curves. Modified from Cheng (2012).....	107
Figure 5-16. Sensitive tornado charts after 5 days of production. Black color represents the high value and gray color stands for the low value.	108
Figure 5-17. Sensitive tornado charts after 7.5 years of production. Black color represents the high value and gray color stands for the low value.	108
Figure 5-18. Diffusion impact on radon wellhead concentration.....	111
Figure 5-19. Gas production rate of two cases	112

Abstract

The objectives of this research dissertation include: (1) develop a novel procedure of single well chemical tracer test (SWCTT) and modification of method of moments (MoM) to estimate mobile oil saturation; (2) apply partitioning tracer to evaluate hydraulic fracture in unconventional reservoir; (3) develop a random walk particle tracking algorithm to simulate partitioning tracer transport in two-mobile-phase condition; (4) evaluate radon wellhead concentration associated with shale gas production to assess its danger to the public health.

A novel procedure of SWCTT is developed and method of moments is modified accordingly after investigating the movement of partitioning tracer. These modifications provide a simple and robust way to use SWCTT to estimate mobile oil saturation. Sensitivity analysis is also conducted to study the impacting reservoir properties that may affect result reliability.

Partitioning tracer is also introduced into the hydraulic fracture diagnosis. Partitioning tracer is proposed to be injected along with the fracking fluid and record tracer flow back data. Within one to two days' production, sufficient tracer production data will be obtained to estimate fracture volume. Tracer selection criteria for this purpose are proposed.

A random walk particle tracking algorithm is developed to track the movement of partitioning tracer particles in the two-mobile-phase condition, which accounts for the contributions from advection and dispersion. Its result is compared with finite-difference based method, showing the advantage of less numerical dispersion.

Lastly, radon wellhead concentration from shale gas reservoir is estimated by integrating its generation, transport and decay process. Impacts of pore geometry and pore size distribution on radon in-situ concentration are investigated. Sensitivity analysis is also carried out to demonstrate which operation or stimulation parameters will affect radon production. The research outcome shows that the radon wellhead concentration can be above the safety level and it requires appropriate monitor and control.

Overall, this dissertation quantifies the particle movement in unconventional reservoirs. It studies particles' transport properties, considering its dispersion, partitioning and reaction features. The ultimate goal of this dissertation is to provide an improved reservoir characterization.

Chapter 1. Introduction

1.1 Research Motivations

Reservoir characterization is one essential component in reservoir exploration and development. Understanding the movement of chemical particles, such as partitioning tracer, will help engineers achieve a better understanding about the ‘black-box’ subsurface.

The SWCTT has been applied for decades and many successes have been declared in estimating residual oil saturation in near wellbore locations. The information obtained from SWCTT is critical for designing enhanced oil recovery (EOR). However, a key assumption in conventional SWCTT is that only single phase (water) is mobile. This is often not the case in real practices, and significant error can occur if the conventional SWCTT analysis method is used when multiple phases flow at the same time. Therefore, it is imperative to resolve this issue so that SWCTT can be applied for two-mobile-phase condition.

Hydraulic fracturing is applied in shale gas development to increase well productivity. The knowledge of hydraulic fracture volume is essential in determining the stimulation treatment effectiveness. However, the fracture volume diagnosis is very challenging because of the complexities of rock property and fracturing process. Davis (2009) summarized capabilities and limitations of numerous fracture diagnostic technologies, including tiltmeters, microseismic mapping and radioactive tracers. Among them, only surface tilt mapping is able to determine the hydraulic fracture volume, while its resolution decreases with depth. As a reservoir characterization tool, chemical tracer can be used to evaluate the swept volume. Hence, the application of

chemical tracer in hydraulic fracture diagnosis, especially in determining fracture volume, is of the interest. It will provide a simple and cost-effective approach for post stimulation evaluation.

Reservoir simulation is an applied approach to interpret the particles' movement. Finite difference and streamline are two major simulation techniques. However, they both have drawbacks. Finite difference method solves the advection-dispersion equation numerically, introducing significant numerical dispersion. On the other hand, streamline simulation assumes no interaction between streamlines, which means no transverse transport is considered. Random walk particle tracking (RWPT) is an alternative algorithm. It simulates both transverse and longitudinal dispersion with less numerical dispersion. Nevertheless, current RWPT is not able to track the movement of partitioning particles under two-mobile-phase condition. To complete the application of RWPT, this dissertation discusses a solution to it.

Naturally occurred hazardous material is of the interest in oil and gas industry. It is important to understand their movement in subsurface and evaluate their threat to the environment and the public. Radon associated with shale gas production is one concern that recently goes into the scrutiny. Therefore, for a sustainable development of shale gas, understanding the migration of radon and evaluating its production are crucial.

1.2 Research Objectives

This dissertation attempts to quantify the movement of particles and address the following objectives:

- Propose a novel procedure of SWCTT and modify MoM to estimate mobile oil saturation
- Investigate the partitioning tracer movement in hydraulic fractures and utilize partitioning tracer as a fracture diagnostic tool. Tracer selection criteria will be studied as well.
- Develop a modified RWPT to track partitioning tracer movement under two-mobile-phase condition
- Comprehensively study the radon migration process and quantitatively evaluate radon wellhead concentration.

1.3 Chapter Layout

Chapter 2 proposes an innovative procedure of SWCTT and modify the method of moments (MoM), aiming at the two-mobile-phase condition. The intention of this chapter is to improve the accuracy and precision of SWCTT interpretation in multi-phase flow condition.

Chapter 3 employs partitioning chemical tracer to estimate hydraulic fracture volume. It discusses the unique feature observed in tracer production data and introduces the interpretation procedure. A sensitivity analysis is carried out to understand the tracer selection criteria.

Chapter 4 proposes a modified RWPT program to simulate the partitioning tracer's movement under two-mobile-phase condition. Its result is compared with finite-difference based method showing less numerical dispersion from RWPT.

Chapter 5 quantitatively evaluates the radon concentration from fractured shale gas wells. It proposes mathematical formulations to calculate the radon generation in both slit shape pores and spherical pores. Numerical simulation is utilized on model radon transport process in the subsurface formation system considering the laboratory measured pore size distribution. A sensitivity analysis about operation and stimulation parameters is carried out to study their impacts on radon wellhead concentration.

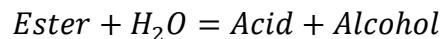
Chapter 6 presents the conclusions and detailed recommendations for future research.

Chapter 2. Improved Method of Moments to Determine Mobile Phase Saturations with Single Well Chemical Tracer Test

2.1 Introduction

Chemical tracer test is a well-established technique to characterize reservoirs by injecting chemical tracers into the subsurface formation (Shen et al. 2016; Shen et al. 2017). Single well chemical tracer test (SWCTT) is one type of chemical tracer tests classified by its well configuration. One major application of SWCTT is to estimate residual oil saturation before and after Enhanced Oil Recovery (EOR) operations. The application was first presented by Tomich et al. (1973) and many successful tests were conducted in the fields (Sheely Jr and Baldwin Jr 1982; Denney 2011). It was also reported that SWCTT was able to evaluate residual gas saturation (Bragg et al. 1976) and connate water saturation (Deans and Shallenberger 1974). This chapter focuses on SWCTT in oil-water reservoirs.

Partitioning (primary) tracer, normally an ester, is the chemical component used in SWCTT to determine the residual oil saturation. It is soluble in both oil and water and reaches equilibrium in both phases based on the partition coefficient of the ester. Ester is also able to react with water generating acid and alcohol (secondary tracer), and the product alcohol is only soluble in water (Deans and Carlisle 1988), so that it functions as a conservative tracer.



The hydrolysis in SWCTT is assumed to be a first-order reaction. The reaction rate is dependent on not only ester concentration, but also many other factors such as pH, temperature, and salinity (Wellington and Richardson 1994). The ester will start to

generate alcohol once it is mixed with water. Moreover, all these parameters should be considered carefully in SWCTT design and analysis.

A typical SWCTT consists of four steps (Figure 2-1). First, an aqueous ester solution slug is injected into the target zone at a low concentration. Second, chasing water is injected to push the ester farther into the formation about five to fifteen feet away from the wellbore. Third, the well is shut in for several days to allow the ester to react with water sufficiently. Fourth, the well is open to produce the tracers back. During the production stage, concentrations of ester and alcohol will be recorded carefully. More detailed descriptions of the SWCTT procedure are available in the literatures (Jerauld et al. 2010; Deans and Mut 1997).

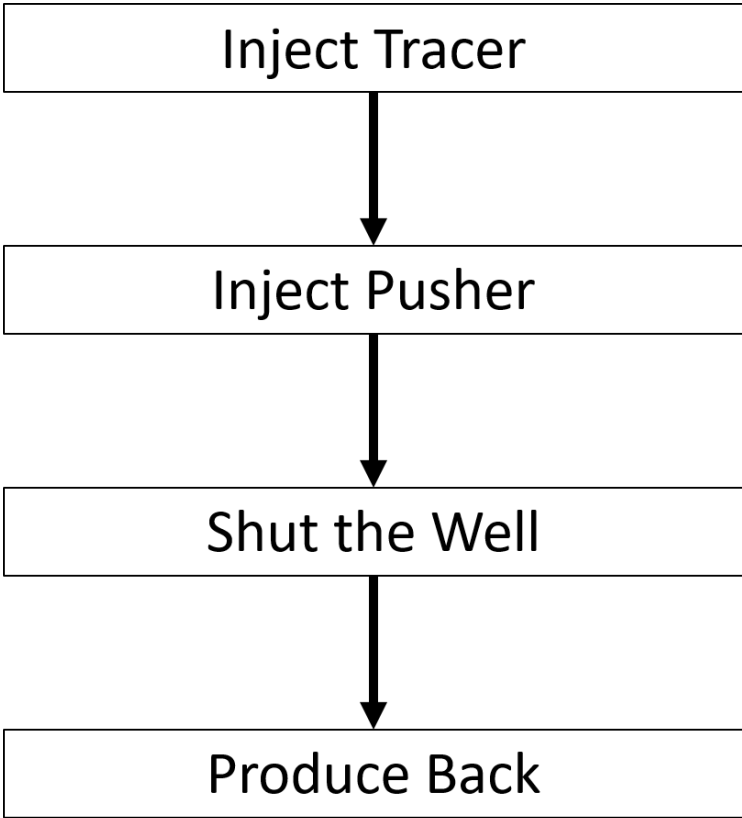


Figure 2-1. Procedure of conventional SWCTT

Compared with alternative methods to determine oil saturation, such as core analysis and well logging, SWCTT has several advantages. First, SWCTT reflects saturation in a larger volume than core analysis or well logging (Tomich et al. 1973). Second, the SWCTT provides a more direct measurement of oil saturation than well logging (Jin et al. 2015). Furthermore, SWCTT does not bring any further formation damage, which means formation would return to its original condition after the test (Bu et al. 2014).

Method of moments (MoM) is a quick and robust method to analytically estimate residual oil saturation based on SWCTT results. Compared against inverse modeling, an alternative method to interpret SWCTT (Cockin et al. 2000), MoM requires less reservoir information. Given the production history of primary and secondary tracers (i.e., ester and alcohol production history), the first moments can be calculated to determine the average residual oil saturation (Oyerinde 2004; Shook et al. 2004).

A key assumption in using conventional SWCTT is that only one phase is mobile. However, this is often not the case in reality, and significant error of saturation estimation can occur if the analysis algorithm MoM is used when multiple phases flow at the same time. Therefore, the objective of this research is to improve the accuracy and precision of SWCTT interpretation under the condition of multi-phase flow.

MoM can also be used to estimate the average residual oil saturation through a Partitioning Interwell Tracer Test (PITT) (Shook et al. 2009; Cooke 1971; Tang 1995). In PITT analysis, in order to estimate saturations properly using MoM, the oil phase should remain immobile as it is assumed in SWCTT. Asakawa (2005) relaxed this

assumption for PITT by accounting for two-phase flow in MoM. However, the estimation of average oil saturation obtained by his method should be close to the residual oil saturation, because most mobile oil was produced before tracer production (Tang and Zhang 2000; Asakawa 2005); when the oil saturation is much higher than the residual oil saturation, the modified MoM may yield a large error.

This chapter focuses on the development of an innovative procedure of SWCTT for the condition of two mobile phases. A mixture of oil and water is injected in new SWCTT instead of a pure aqueous phase solution. In addition, when developing the modification of MoM, a ratio parameter is introduced to adjust the swept water volume difference between the primary tracer and the secondary tracer. Using this new scheme of SWCTT and interpretation approach, saturations of two mobile phases can be determined.

2.2 Modified SWCTT and MoM

2.2.1 Modified Procedure of SWCTT

For the oil-water reservoir with two mobile phases, conventional SWCTT will displace the oil far into the formation and the water saturation near the wellbore can be attained from fractional flow theory (Buckley and Leverett 1942). As the result, the reservoir volume contacted by the tracer would have average oil saturation different from the initial oil saturation. Therefore, to maintain the initial saturation during the tracer test, a new modified SWCTT procedure is proposed as follows:

1. Get the oil/water rate ratio from the production data when the production is stable.

2. Inject the primary tracer along with a mixture of oil and water at the ratio obtained in the first step. The primary tracer is a partitioning tracer and it will generate a secondary conservative tracer in the aqueous phase. The injected oil and water mixture is preferred to be from the target formation and it can be collected from the production in real practice.
3. Inject pusher: the mixture of oil and water with no partitioning tracer. The ratio of oil and water is kept the same with step 2. This step is to push the partitioning tracer into the reservoir.
4. Shut in the well for the partitioning tracer hydrolysis reaction.
5. Produce back all the tracers at a stable rate and measure the primary tracer concentration in the oil and water mixture accordingly as well as the secondary tracer concentration in water at the surface

2.2.2 Movement of Tracers

The primary tracer is an ester. Once the ester is injected, it partitions between oil and water, and the partition coefficient, K , is defined below.

$$K = \left(\frac{C_{\text{ester,o}}}{C_{\text{ester,w}}} \right)_{\text{eq}} \quad (2-1)$$

The ester is travelling at a weighted average velocity, V_{ester} , determined by the velocities of oil, V_o , and water, V_w , since it partitions into both phases (Deans and Carlisle 1988):

$$V_{\text{ester}} = fV_w + (1 - f)V_o \quad (2-2)$$

Where f is the fraction of time that ester spends in water with expression (Deans and Carlisle 1988):

$$f = \frac{1}{1 + KS_o/S_w} \quad (2-3)$$

Where S_o and S_w stand for oil and water saturation respectively.

To achieve a better result, the partition coefficient should be constrained within the optimum range ((Deans and Majoros 1980):

$$0.5 \cdot \frac{(1-S_{or})}{S_{or}} < K < 1.5 \cdot \frac{(1-S_{or})}{S_{or}} \quad (2-4)$$

If residual oil saturation varies from 0.2 to 0.5, for example, the partition coefficient used in SWCTT should be within the range of 0.5-6 based on Eq. 2-4. The secondary tracer is alcohol as the result of ester hydrolysis and is solely soluble in water. Thus, it travels with the velocity of water. Alcohol doesn't occur naturally and is conservative in most reservoirs. These characteristics of alcohol make the measurement of oil saturation feasible. Acid is the other product of ester hydrolysis reaction. However, it might be consumed by other existing components in formation and might not be produced back (Deans and Carlisle 1988).

Figure 2-2 is the tracer concentration profile at the end of the injection of the pusher. Because the hydrolysis reaction starts simultaneously when the ester is injected, there would be a small amount of alcohol being generated during the injection step. This figure shows that water saturation is greater than oil saturation and water mobility is assumed to be higher. Consequently, water moves faster than oil. Based on Eq. 2-2 and Eq. 2-3, Ester is retarded because of its partition, and it needs to travel back and forth between the oleic phase and aqueous phase.

Figure 2-3 shows the shut-in period. The shut-in duration should be long enough to allow the ester to react sufficiently, so that the product alcohol should have a concentration peak collapsed with ester in location, as illustrated in Figure 2-5.

When the well is open to produce back, the alcohol will flow back faster than ester because of the higher water velocity. At the wellhead, the breakthrough of alcohol would be observed first. The production step is shown in Figure 2-4.

If the oil velocity is higher than water, the relative position of ester and alcohol is reversed. In such a case, ester will travel faster and it will be produced back first as well. The shut-in time still needs to be long enough for the same reason.

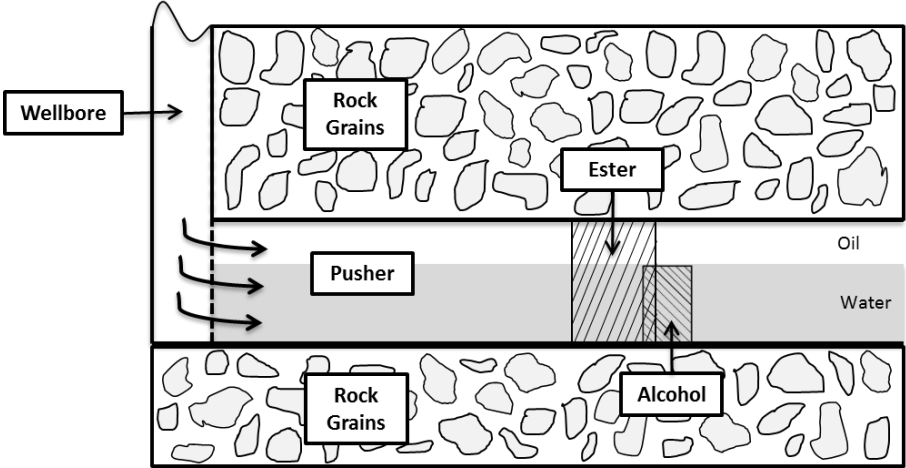


Figure 2-2. At the end of injection of pusher. Alcohol moves faster than ester so that alcohol travels farther than ester.

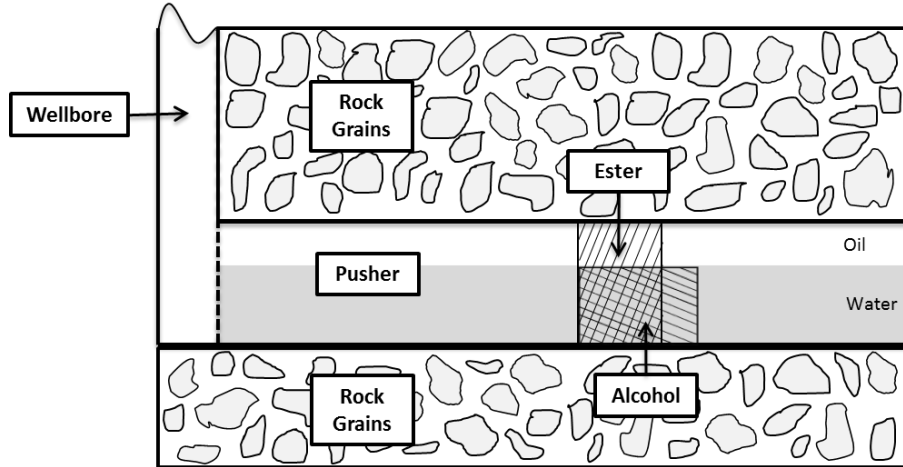


Figure 2-3. At the end of shut in period. Ester reacts with water generating alcohol. Both of ester and alcohol remains stationary.

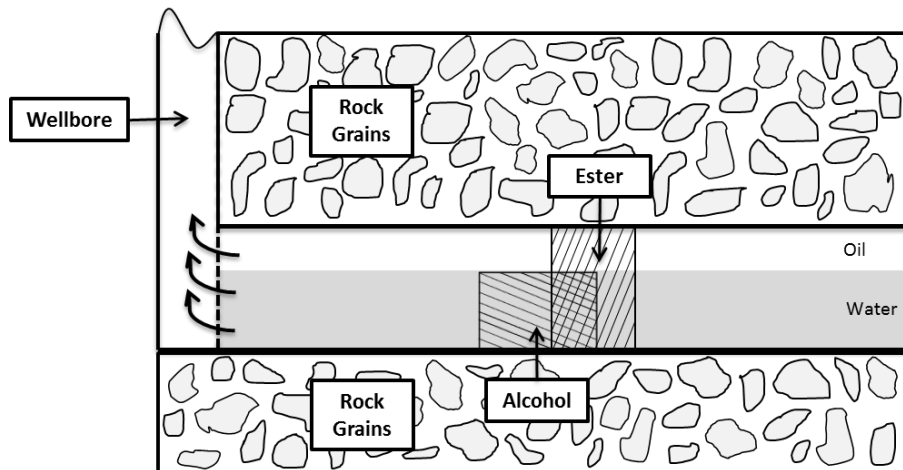


Figure 2-4. During the production period. Alcohol travels faster than ester and its production will be observed at first.

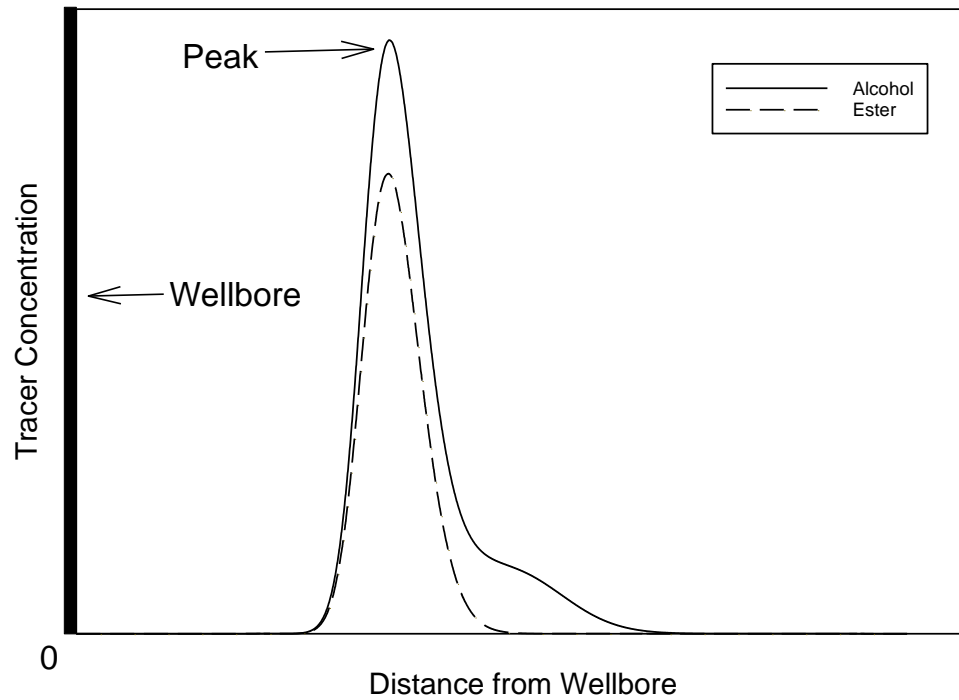


Figure 2-5. A schematic illustration of concentration of alcohol and ester in water at the end of shut in. Alcohol concentration peak position collapsed with ester concentration peak.

2.2.3 Modified MoM

Appendix A presents a detailed derivation of the proposed MoM. Residence time \bar{t} , which is calculated from the first moment, is modified by including two-phase flow:

$$\bar{t}_k = \frac{\int_0^{\infty} t(\sum_{l=w}^o f_l C_{kl}) dt}{\int_0^{\infty} f_w C_{kw} dt} \quad (2-5)$$

Where C is the concentration of tracer k , f is the volumetric fraction of phase w , subscript k represents the tracer k , w indicates water and o indicates oil. Hence, for two tracers that partition coefficients, which are K_1 and K_2 , their swept volumes are expressed respectively:

$$\widehat{V}_{w,1} + K_1 \widehat{V}_{o,1} = q \bar{t}_1 \quad (2-6)$$

$$\widehat{V}_{w,2} + K_2 \widehat{V}_{o,2} = q \bar{t}_2 \quad (2-7)$$

Where q is the constant production rate, \widehat{V} is the volume swept by the tracer, subscript 1 and 2 stands for two different tracers.

As shown in Figure 2-5, two tracers with different partitioning preferences might have a different contacted volume of water as well as oil. The contacted volume could be calculated as the area beneath the curve. To get accurate saturation estimation from MoM, such difference needs to be adjusted. Hence, a parameter R is introduced as the ratio of contacted volume of tracer 1 to contacted volume of tracer 2 in either water or oil. It can be expressed by:

$$R = \frac{\widehat{V}_{w,1}}{\widehat{V}_{w,2}} = \frac{\widehat{V}_{o,1}}{\widehat{V}_{o,2}} \quad (2-8)$$

Eq. 2-6 can be rewritten by substituting Eq. 2-8:

$$R \cdot \widehat{V}_{w,2} + R \cdot K_1 \widehat{V}_{o,2} = q \bar{t}_1 \quad (2-9)$$

Solving Eq. 2-9 and Eq. 2-7 together, the average oil saturation is:

$$S_o = \frac{R \cdot \bar{t}_2 - \bar{t}_1}{(K_2 - 1) \bar{t}_1 - R \cdot (K_1 - 1) \bar{t}_2} \quad (2-10)$$

For the modified SWCTT, the partition coefficient of tracer 1 in the above equation is zero. Thus, Eq. 2-10 can be simplified for the specific case:

$$S_o = \frac{R \cdot \bar{t}_{\text{ester}} - \bar{t}_{\text{alcohol}}}{(K_{\text{ester}} - 1) \bar{t}_{\text{alcohol}} + R \cdot \bar{t}_{\text{ester}}} \quad (2-11)$$

2.3 Method Validation and Comparison

2.3.1 Model Description

The proposed method was validated through numerical simulation on synthetic cases with known input parameters. Numerical simulation was carried out using Stars software from the Computer Modeling Group (CMG). The model was a cylindrical domain with a single vertical well in the center (Figure 2-6), and the reservoir had homogeneous and isotropic petrophysical parameters. Two mobile phases existed and their saturations were uniform spatially. Grid size could affect the simulation output. To minimize the numerical dispersion, the grids near the wellbore were 0.1 ft. This selection of grid size is justified in section 2.4.4. The relative permeability curve is given in Figure 2-7 and residual oil saturation was 0.87. In the simulated models, ethyl formate is injected as the primary tracer (ester). Its partition coefficient was assumed as 1.5. The model included the first order hydrolysis reaction. Appendix B shows one input file for the simulation with initial oil saturation of 0.9.

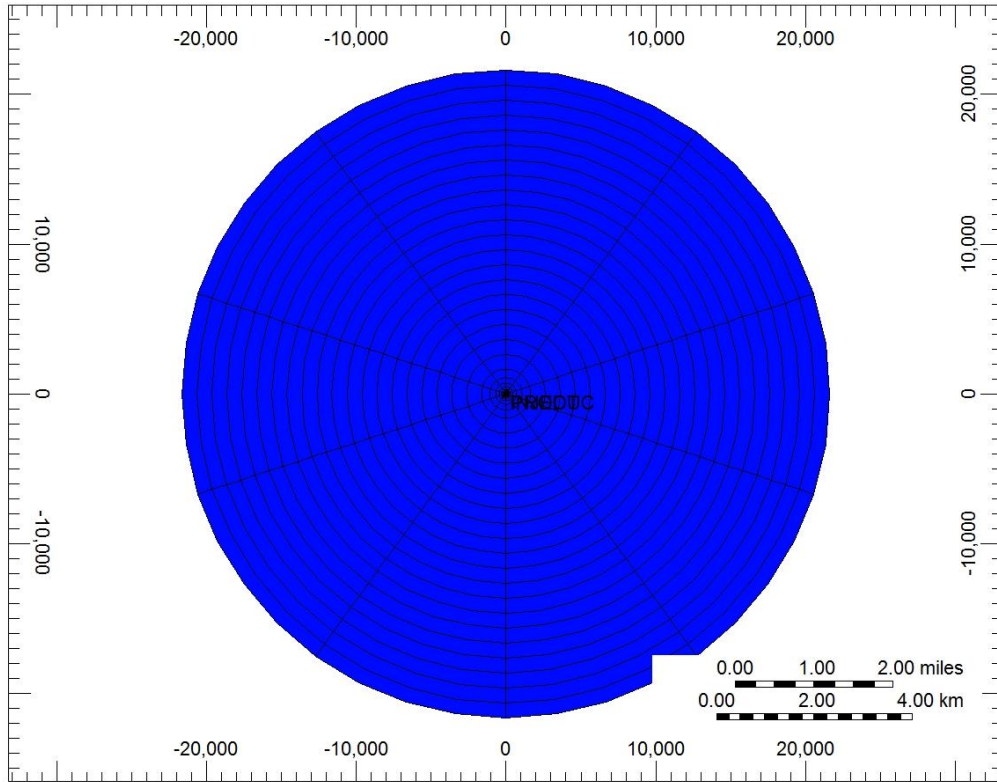


Figure 2-6. Cylindrical domain of reservoir. Injector and producer are located at the center. Saturation is spatially constant.

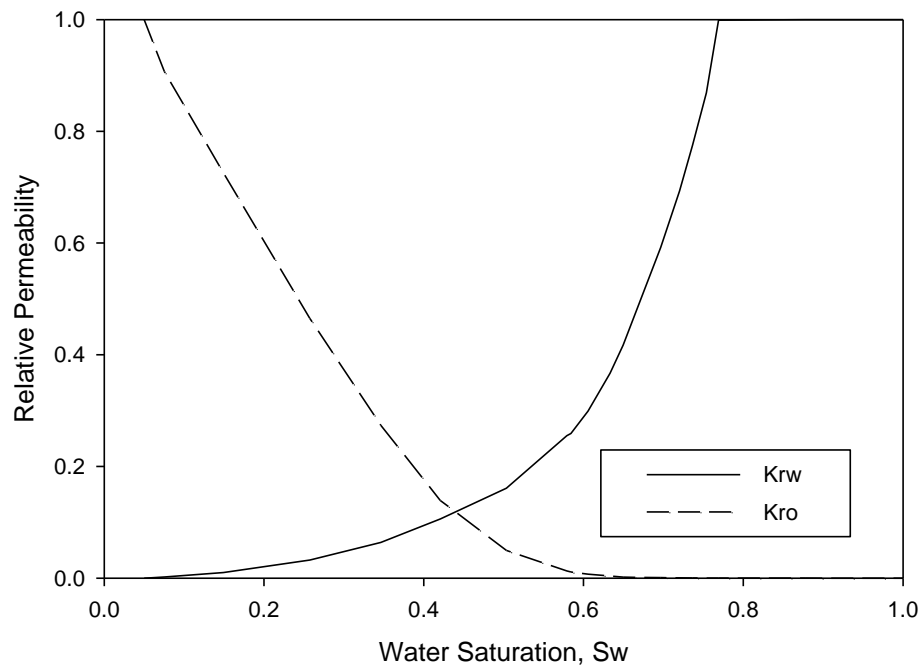


Figure 2-7. Relative Permeability Curve

The well injected a mixture of oil and water with the partitioning tracer for 0.08 days at a low concentration – the mole fraction of ethyl formate was 0.0025. The constant injection rate was 550 bbl/day (no constraints on bottom-hole pressure (BHP)). The well continued to inject the pusher without the partitioning tracer until 0.5 days. The next step was to shut in the well for 1 day to allow the tracer to react and generate a conservative tracer - alcohol. The well was open to produce back after shut-in at a constant production rate of 820 bbl/day. More input parameters are listed in Table 2-1.

Table 2-1. Input parameters in the numerical simulation		
Reservoir and Fluid Properties		
Parameter	Value	Unit
Number of Reservoir Girds	(737,10,1)	(r,θ,z)
Reservoir Radius	21624	ft
Reservoir Thickness	16	ft
Porosity	0.19	fraction
Permeability	1000	md
Temperature	219	°F
Initial Reservoir Pressure	4925	psi
Water Compressibility	2.9E-6	psi ⁻¹
Oil Compressibility	3.5E-6	psi ⁻¹
Partition Coefficient	1.5	-
Well Constraints (No constrains on BHP)		
Well Controls	Value	Unit
Injection Rate	550	bbl/day
Production Rate	820	bbl/day

2.3.2 Analysis Procedure

In this section, a systematic analysis is demonstrated as an example to illustrate the calculation procedure using the modified method. The case with an initial oil saturation of 0.9 is used.

1. Plot the tracer production history, i.e., tracer concentration vs. time as shown in Figure 2-8. This graph should contain the primary tracer (ester) in both oil and water and the secondary tracer (alcohol) in water.

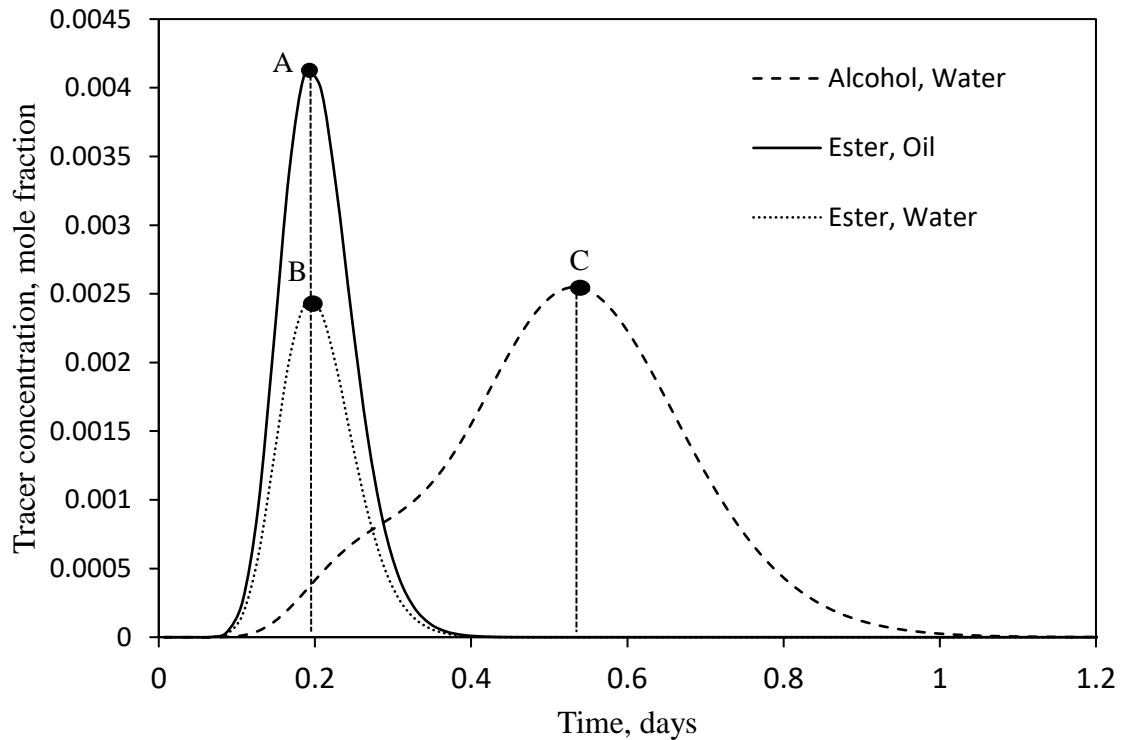


Figure 2-8. Production history of tracers for Case 1.

2. Find the time of the concentration peak as the points A, B & C indicated in Figure 2-8.

$$t_{\text{ester}} = t_{A/B} = 0.17 \text{ day}$$

$$t_{\text{alcohol}} = t_C = 0.52 \text{ day}$$

Ester in water and oil has the same residence time, but different concentrations. This is because of its partitioning behavior in the oil and water. The peak time of alcohol is different from that of ester because the travel velocity is different. Alcohol is conservative in water, therefore its velocity is water velocity V_w , and ester velocity V_{ester} is expressed in Eq. 2-2.

- From the peak time, the velocity ratio can be estimated because the peaks are located at the same distance from the wellbore after shut in.

$$\frac{V_w}{V_{ester}} = \frac{t_{ester}}{t_{alcohol}} = \frac{0.17}{0.52} = 0.33$$

- Calculate the residence time of ester and alcohol only in water according to the following equation:

$$\bar{t}_{k,w} = \frac{\int_0^{\infty} t C_{kw} dt}{\int_0^{\infty} C_{kw} dt} \quad (2-12)$$

In this specific case:

$$\bar{t}_{ester,w} = 0.2 \text{ day} \quad \text{and} \quad \bar{t}_{alcohol,w} = 0.53 \text{ day}$$

- From above parameters (velocity ratio and residence times), the ratio parameter R is calculated.

$$R = \frac{\hat{V}_{alcohol,w}}{\hat{V}_{ester,w}} = \frac{V_w \bar{t}_{alcohol,w}}{V_{ester} \bar{t}_{ester,w}} = 0.33 * \frac{0.53}{0.2} = 0.86$$

- Obtain the flow fraction from the production data:

$$f_w = 4\% \text{ and } f_o = 96\%$$

- Use Eq. 2-5 to calculate the residence time of ester and alcohol:

$$\bar{t}_{alcohol} = 0.53 \text{ day and } \bar{t}_{ester} = 8.8 \text{ days}$$

- Substitute all the parameters into Eq. 2-11, the oil saturation is:

$$S_o = 0.9$$

And subsequently, $S_w = 1 - S_o = 0.1$.

2.3.3 Saturation Estimation

Previous section used one case as an example to demonstrate the procedure of modified SWCTT and interpretation of tracer production data using the proposed formulas. Five more cases with different initial in-situ oil saturations were carried out. Their water flow fractions were calculated as shown in the last row in Table 2-2. Saturations estimated based on tracer production history following proposed approach are shown in Table 2-2 as well. From the results, it is seen that the analysis from modified SWCTT matched the input values very well.

Table 2-2. Proposed approach verification through modified SWCTT procedure						
	Case 1	Case 2	Case 3	Case 4	Case 5	Case 6
Input Initial S_o	0.9	0.8	0.7	0.5	0.25	0.1
Calculated S_o through Modified MoM	0.9	0.81	0.69	0.53	0.26	0.1
Water Flow Fraction	4%	18%	45%	95%	99%	100%

During the shut-in period, the peak of alcohol needs to be significantly higher than the rest. Otherwise, it is hard to clearly locate the point C in Figure 2-8 in production history, which will result in inaccurate estimation. Hence, a careful design of the tracer test before installment is imperative.

The major concerns of applying the proposed SWCTT in real fields would be its mixture injection. The injected oil phase property may differ from its original condition because solution gas would come out in the separators. Also, gravity and immiscibility would separate oil and water. However, it is also necessary to keep in mind that the injection volume is relatively small compared to the entire reservoir and these issues may only limitedly affect the saturation distribution. Nevertheless, further investigations into the details would be necessary to resolve these concerns, and attentive operation and analysis are essential to the success of SWCTT.

2.3.4 Comparison with Conventional Interpretation Methods

Currently, there are two analysis approaches: landmark comparison and conventional MoM. Tang and Harker (1990) proposed the landmark comparison approach to estimate residual oil saturation based on chromatographic transformation of the two tracer curves (i.e., production history of partitioning tracer and conservative tracer). After normalizing the tracer concentration, Tang and Harker (1990) concluded that the two curves can be collapsed together by multiplying a factor $(1 + \beta)$ to the arrival time of conservative tracer. In common practices, operators select the peak time to quickly find the parameter β (Deans and Carlisle 1988). Maroongroge (1994) derived an equation to calculate residual oil saturation using MoM. First moment is used to calculate the residence time. Asakawa (2005) further extended MoM so that it could handle two-mobile-phase condition. The detailed procedure of each method can be found in the references, which will not be discussed more here.

In this section, both the landmark comparison method (Tang and Harker 1990) and the conventional MoM (Asakawa 2005) were used to analyze the same tracer production data (i.e. obtained from the modified SWCTT procedure) and compared their results with the proposed modified MoM. Table 2-3 shows the results. Comparisons show that the proposed new approach could provide a more accurate estimation of oil saturation than the other two methods. The landmark comparison even gave the negative oil saturation when oil mobility was large. Its estimation became rational when oil mobility approached to zero. This is because this method does not consider the partitioning tracer production in oil. In addition, the proposed approach is also applicable to immobile oil saturation. For example, oil was stationary when its saturation was 0.1. At this situation, the proposed SWCTT procedure becomes the conventional SWCTT procedure. Consequently, Asakawa's equations (Asakawa 2005) for two-mobile-phase condition were identical with Maroongroge (1994) and the MoM for single-mobile-phase was utilized. Based on the result in Table 2-3, the modified MoM improved the accuracy of saturation estimation from conventional MoM. The improvement mainly attribute to the swept volume correction factor R . In SWCTT, the partitioning tracer and conservative tracer may locate at different distances from wellbore determined by the phase mobility, which was not considered in conventional MoM. Therefore, it is recommended to use the proposed MoM in the replacement of the conventional MoM (i.e., formulas proposed by Maroongroge (1994)) to interpret SWCTT when there is only one mobile phase.

Table 2-3. Result comparison with conventional interpretation methods.						
	Case 1	Case 2	Case 3	Case 4	Case 5	Case 6
Input So	0.9	0.8	0.7	0.5	0.25	0.1
Landmark Comparison	-0.83	-0.03	0.27	0.44	0.26	0.1
Conventional MoM	0.91	0.8	0.67	0.4	0.19	0.07
Modified MoM	0.9	0.81	0.69	0.53	0.26	0.1

2.3.5 Comparison with Conventional SWCTT Procedure

Six more cases following conventional SWCTT procedure were simulated and the production data through conventional interpretation methods were analyzed. Unlike the modified SWCTT procedure, conventional SWCTT injects water, not oil/water mixture, into the formation. Other model parameters are kept same with the prior description. Figure 2-9 shows the water production rate and tracer concentration history. The analysis of conventional SWCTT is shown in Table 2-4.

The results in Table 2-4 indicate that oil saturation estimated from conventional SWCTT is far different from the input oil saturation when oil mobility is significant (i.e., high oil saturation). On the other hand, for cases in which oil is stationary, a reliable evaluation of oil saturation can be obtained. It is known that tracer informs the petrophysical properties where it sweeps. In conventional SWCTT, the injected water displaces the mobile oil near wellbore and change the oil saturation distribution. Figure 2-9 demonstrates the initial water production rate is 820 bbl/day (oil production rate is zero since producer is constrained by liquid production rate of 820 bbl/day), which proves the previous statement. Since tracer is injected along with such water, only the

knowledge of oil saturation that has already been affected by the injection during SWCTT can be learned from the test. This explains why conventional SWCTT fails to work if oil is mobile. However, for immobile oil, the injected water does not have impact on saturation distribution so that the conventional SWCTT is sufficient to capture the residual oil saturation.

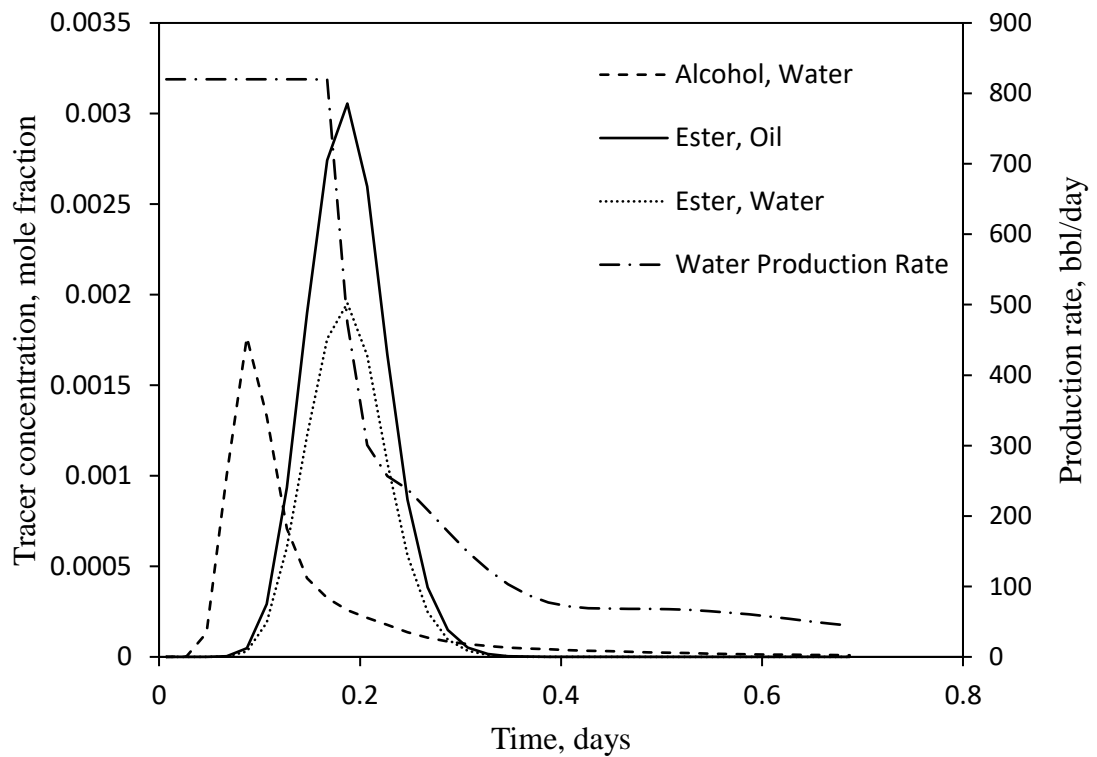


Figure 2-9. Water production rate and tracer production history for Case 7. Conventional SWCTT and initial oil saturation was 0.9.

Table 2-4. Oil saturation evaluated through conventional SWCTT procedure and conventional methods.							
		Case 7	Case 8	Case 9	Case 10	Case 11	Case 12
Input S_o		0.9	0.8	0.7	0.5	0.25	0.1
Calculated S_o	Landmark Comparison	0.44	0.45	0.45	0.46	0.25	0.11
	Conventional MoM	0.58	0.53	0.47	0.37	0.2	0.07
Water Flow Fraction		4%	18%	45%	95%	99%	100%

2.4 Impacting Factor Analysis

2.4.1 Impact of Variable Production Rate

The previous derivation is based on the assumption of constant production rate. This section will discuss how to estimate saturation if production rate varies. It is known that the conservative tracer flows at the same velocity with water, while the partitioning tracer's velocity is determined by both mobile phases. The saturation as well as the ratio of oil velocity over water velocity is constant. Eq. 2-2 can be casted into:

$$V_{\text{ester}} = FV_w \quad (2-13)$$

Eq. 2-13 shows that the velocity of partitioning tracer (ester) can be equivalent to a certain fraction (F) of water velocity. The factor F is independent of absolute

production rate, but is determined by partition coefficient and fractional flow of aqueous phase.

Furthermore, since production rate is not constant, Eq. 2-6 and Eq. 2-7 need to be modified as:

$$\widehat{V}_{w,1} + K_1 \widehat{V}_{o,1} = \widehat{V}_1 \quad (2-14)$$

$$\widehat{V}_{w,2} + K_2 \widehat{V}_{o,2} = \widehat{V}_2 \quad (2-15)$$

Where,

$$\widehat{V}_k = \frac{\int_0^\infty qt(\sum_{l=w}^o f_l C_{kl}) dt}{\int_0^\infty f_w C_{kw} dt} \quad (2-16)$$

Consequently, the new expression for S_o is:

$$S_o = \frac{R \cdot \widehat{V}_2 - \widehat{V}_1}{(K_2 - 1) \widehat{V}_1 - R \cdot (K_1 - 1) \widehat{V}_2} \quad (2-17)$$

Case 13 was created in which producer was constrained by constant BHP of 4700 psi. The initial water saturation was 0.3. Case 3 is the base case for comparison. Figure 2-10 is the simulation output. The calculation procedure is given as follows:

1. Plot the tracer production history, i.e., tracer concentration vs. time as shown in Figure 2-10.

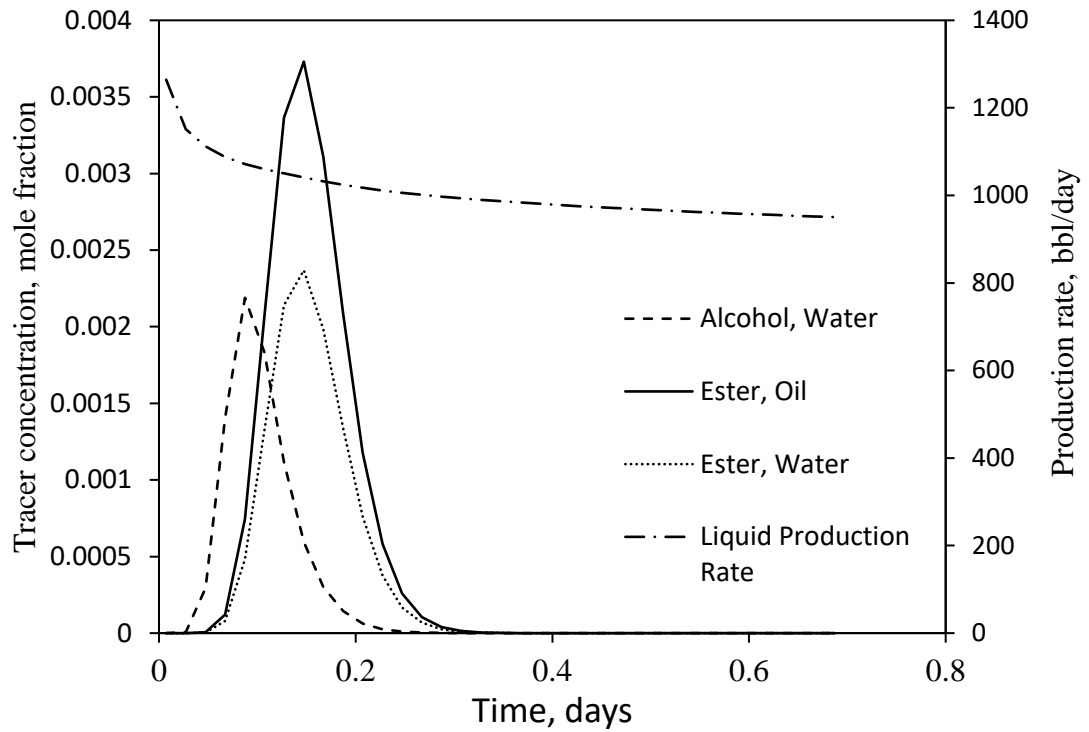


Figure 2-10. Water production rate and tracer production history for Case 13. Variable liquid production rate under a constant BHP constraint.

2. Find the time of the concentration peak.

$$t_{\text{ester}} = 0.147 \text{ day}$$

$$t_{\text{alcohol}} = 0.087 \text{ day}$$

3. Average liquid production rate at each peak time is calculated by cumulative liquid production volume over peak time:

$$\bar{q}_{\text{ester,peak}} = \frac{Q_{\text{ester,peak}}}{t_{\text{ester}}} = 1112 \text{ bbl/day}$$

$$\bar{q}_{\text{alcohol,peak}} = \frac{Q_{\text{alcohol,peak}}}{t_{\text{alcohol}}} = 1152 \text{ bbl/day}$$

4. Estimate the factor F:

$$F = \frac{\bar{V}_{\text{w,alcohol,peak}} t_{\text{alcohol}}}{\bar{V}_{\text{w,ester,peak}} t_{\text{ester}}} = \frac{\bar{q}_{\text{alcohol,peak}} t_{\text{alcohol}}}{\bar{q}_{\text{ester,peak}} t_{\text{ester}}} = \frac{1152 \cdot 0.087}{1112 \cdot 0.147} = 0.61$$

5. Calculate the residence time Using Eq. 2-12:

$$\bar{t}_{ester,w} = 0.15 \text{ day} \quad \text{and} \quad \bar{t}_{alcohol,w} = 0.10 \text{ day}$$

6. The average liquid production rate at each residence time:

$$\bar{q}_{ester,res} = \frac{Q_{ester,res}}{\bar{t}_{ester,w}} = 1106 \text{ bbl/day}$$

$$\bar{q}_{alcohol,res} = \frac{Q_{alcohol,res}}{\bar{t}_{alcohol,w}} = 1135 \text{ bbl/day}$$

The ratio parameter R is calculated:

$$R = \frac{\bar{v}_{alcohol,w}}{\bar{v}_{ester,w}} = \frac{\bar{v}_{w,alcohol,res} \bar{t}_{alcohol,w}}{F \bar{v}_{w,ester,res} \bar{t}_{ester,w}} = \frac{1135 * 0.1}{0.61 * 1106 * 0.15} = 1.12$$

7. Use Eq. 2-16 and Eq. 2-17 to calculate the oil saturation is:

$$S_o = 0.69$$

$$\text{And subsequently, } S_w = 1 - S_o = 0.31.$$

To conclude, when production rate varies, average production velocity should be used to find the ratio parameter R and include production rate into the integration term as Eq. 2-16. Compared with the base case (Table 2-5), following these modified formulas, a reliable saturation estimation could still be obtained. Additional research is needed to further investigate the error embedded for cases with variable production rate. Nevertheless, it is recommended to maintain a constant production rate during SWCTT operation. Considering the short production time, this operation is not difficult to achieve.

Table 2-5. Sensitive analysis results of Case 13 to Case 17, compared with base case (Case 3)						
	Case 13	Case 14	Case 15	Case 16	Case 17	Base Case (Case 3)
Investigating Subject	Variable Production Rate	Heterogeneous permeability	Heterogeneous Oil Saturation	Dispersion		-
Controlling Parameter	Constant BHP at 4700 psi	Vdp=0.5 Mean=1000	Mean=0.7 Std=0.15	Grid Size=0.5 ft	Grid Size=1 ft	-
Calculated S_o through Modified MoM	0.69	0.68	0.67	0.68	0.68	0.69

2.4.2 Impact of Heterogeneous Permeability

Case 14 had a heterogeneous permeability field. The average permeability is same with the base case (Case 3) as 1000 md. Dykstra-Parson coefficient V_{Dp} is assumed as 0.5. Other parameters were the same with the base case. V_{Dp} can be expressed by:

$$V_{Dp} = 1 - \exp(-\sigma) \quad (18)$$

Where, σ is the standard deviation of $\ln(k)$. In other words, in logarithm scale, permeability was assumed to follow a normal distribution with mean of 6.91 (mean = $\ln(1000)$) and standard deviation of 0.69 (std = $-\ln(1 - V_{Dp}) = -\ln(0.5)$). Each grid was assigned with a permeability following such distribution (Figure 2-11) and run the simulation. The calculated saturation is displayed in Table 2-5. It shows that the proposed approach also works in the heterogeneous permeability field. Tracers are pushed farther in larger permeability zone due to the high velocity. However, they will return to the producer at the same time with the tracers injected into lower permeability zone. The reversibility is desirable in SWCTT as just explained (Dean and Carlisle 1988), which makes the heterogeneous permeability not a big problem.

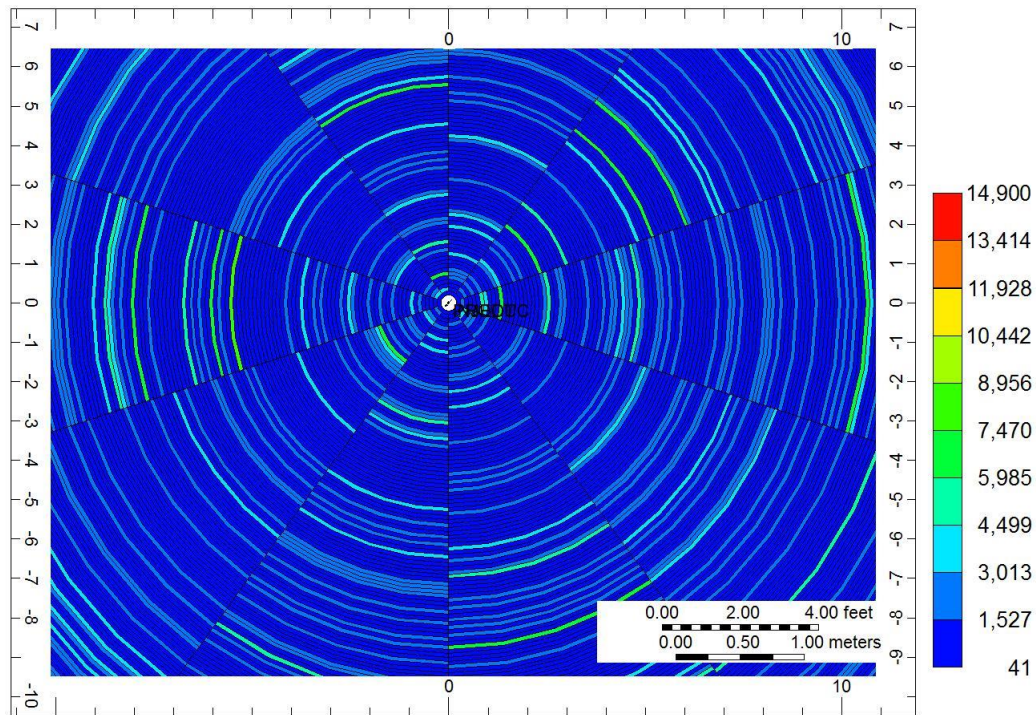


Figure 2-11. Heterogeneous permeability field, zoom in near wellbore. Mean=1000 md, $V_{Dp}=0.5$.

2.4.3 Impact of Heterogeneous Oil Saturation

Similar to the heterogeneous permeability case, a heterogeneous oil saturation field was created in Case 15. It follows normal distribution with mean of 0.7 and standard deviation of 0.15 (Figure 2-12). The permeability was homogeneous and the fraction of injected oil/mixture was identical with the base case. Figure 2-13 demonstrates that the oil production rate was constant at the beginning because the injection of oil/water mixture had a constant ratio. After about 0.2 day, fluctuation in oil production is observed since oil distribution in reservoir was heterogeneous. The result of Case 15 in Table 2-5 illustrates that the oil saturation estimation was close to the input mean value, suggesting saturation from SWCTT is on a volume-averaged basis

(Shook et al. 2004). On the other hand, the difference between input mean value and estimation was larger than the base case. Tracers that were produced in the non-constant oil rate period influenced the calculation of MoM, which resulted in the larger difference. In addition, the injection oil/water ratio is critical. Because most tracers were produced back at the constant oil rate stage, these tracers will reflect the saturation corresponding to the specific injected oil/mixture ratio. Therefore, even though heterogeneous oil distribution is unfavorable to SWCTT, the proposed MoM is still able to get a rough estimation of the average oil saturation over the inspected zone by careful design.

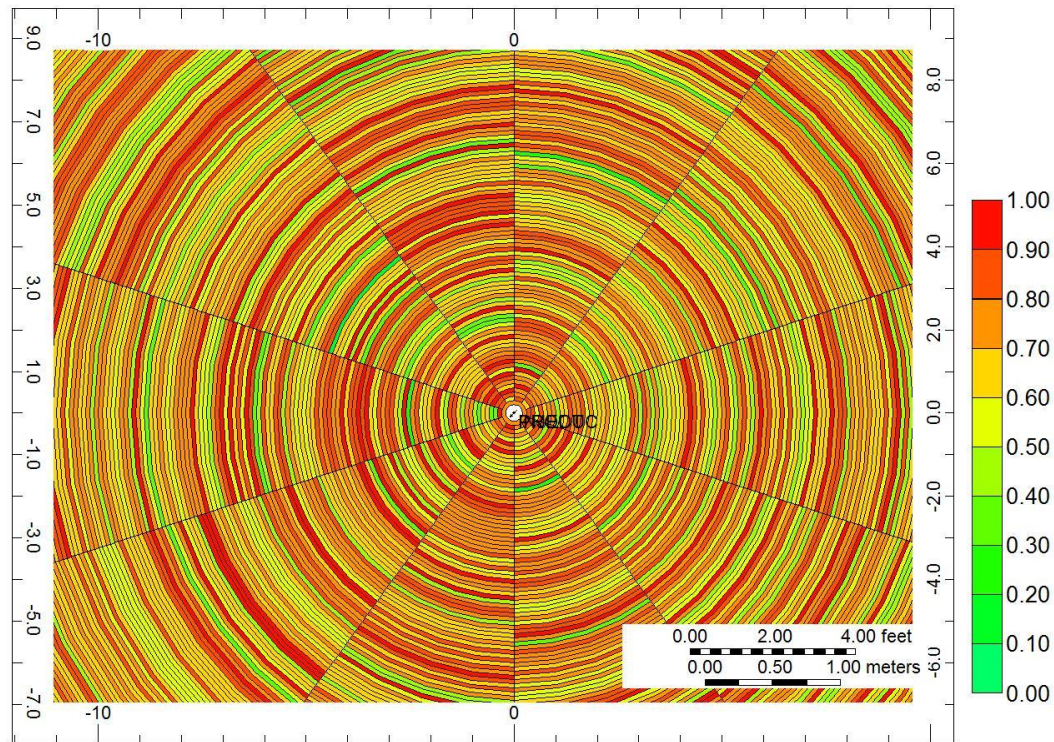


Figure 2-12. Heterogeneous oil saturation field, zoom in near wellbore. Mean = 0.7, std=0.15.

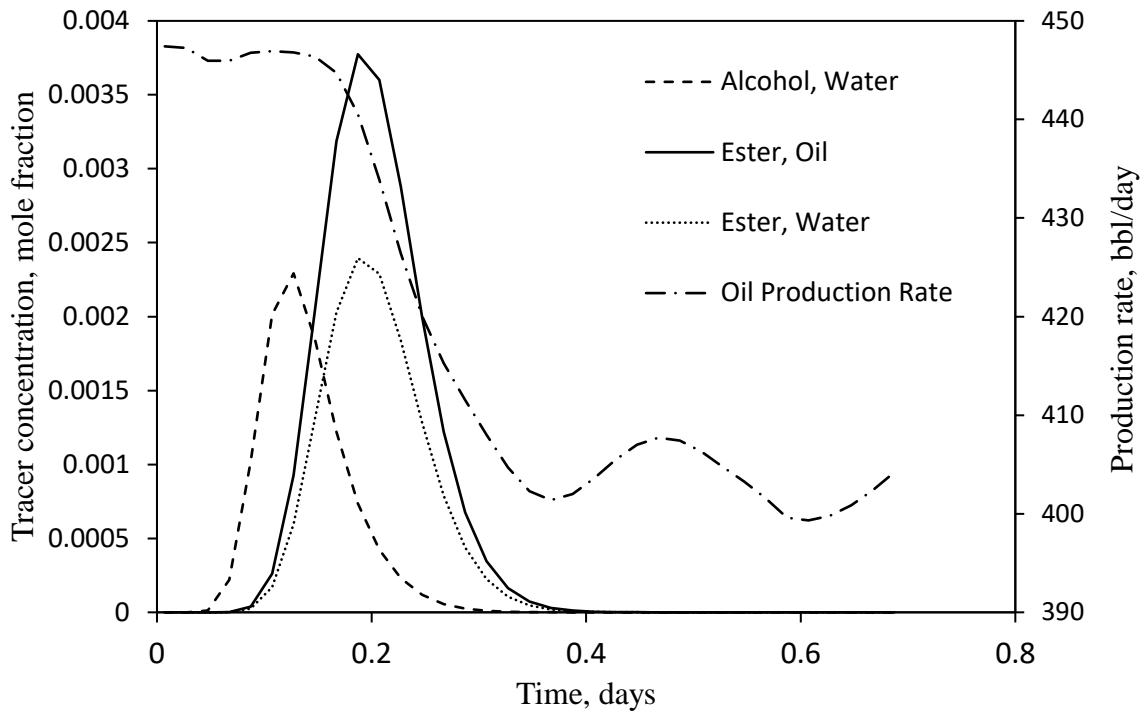


Figure 2-13. Oil production rate and tracer production history for Case 15. Heterogeneous oil saturation.

2.4.4 Impact of Dispersion

The equation derivation and previous simulation models neglected the dispersion. However, in field application, dispersion is inevitable. This section varies the grid size near wellbore to mimic the dispersion. The base case had the grid size of 0.1 ft. Case 16 and Case 17 had grid size of 0.5 ft and 1 ft near wellbore respectively. To maintain the same reservoir pore volume, the grid number was modified correspondingly. Figure 2-14 shows the conservative tracer (alcohol) production history for all three cases. Along with the increase of grid size, the tracer history is more dispersed due to dispersion. The partitioning tracer production history had the similar change with the conservative tracer. Table 2-5 shows the saturations calculated using the proposed approach. The estimation of saturation did not vary a lot when the grid

size as well dispersion became larger. The dispersion does not alter the basic mechanism of tracer velocity affected by oil and water. Thus, although tracer could be more dispersed in the formation, which will be reflected in the production, the answer from proposed approach is trustworthy. In addition, this observation justifies that the selection of 0.1 ft as grid size near the wellbore is reasonable.

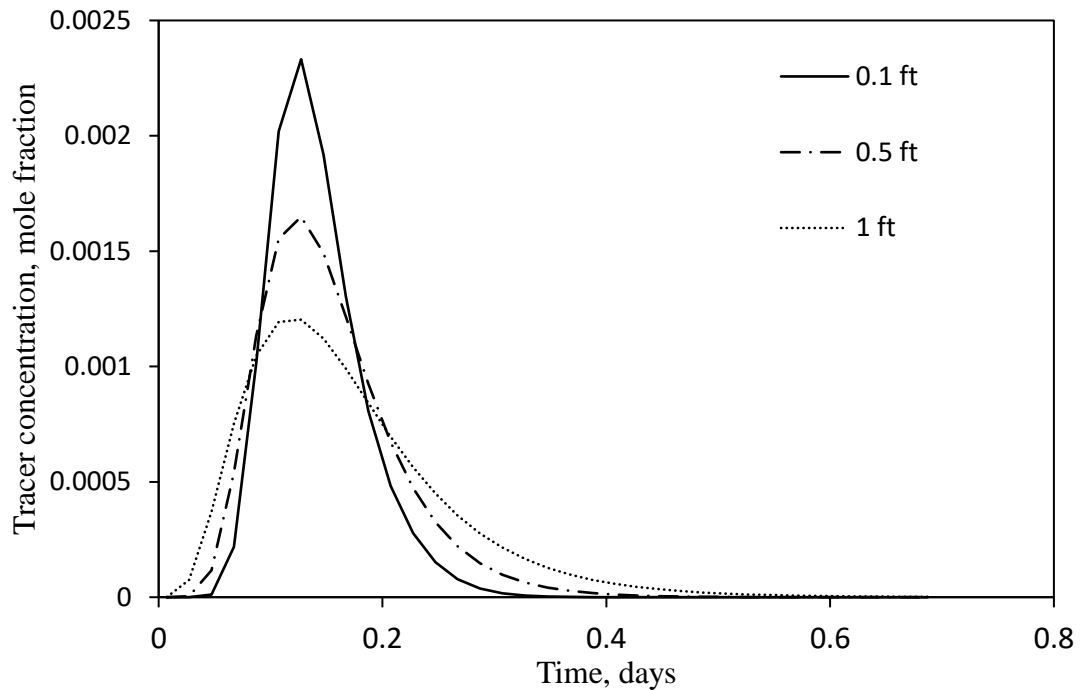


Figure 2-14. Conservative tracer (alcohol) production history comparison.

2.5 Conclusions

Based on the above results and discussion, the following conclusion can be drawn:

1. An innovative SWCTT is developed. MoM is modified to estimate mobile oil saturation from the innovative SWCTT.

2. The new tracer method has been proved using numerical simulations and it provides a reasonably precise measurement of mobile saturations.
3. The new modified MoM is applicable in conventional SWCTT to measure immobile oil saturation and improved the accuracy of conventional MoM.
4. The new tracer method is an easy and robust in-situ way to measure oil and water saturations near the wellbore at any time of production, without the limitation of conventional SWCTT analysis. The new modified SWCTT can better assist engineers to monitor the reservoirs and determine the best time to start EOR operations.

Nomenclature

Normal

C	=tracer concentration, M/L^3
F	=velocity factor, dimensionless
f	=fraction of time partitioning tracer spends in water, dimensionless
K	=partition coefficient, dimensionless
Q	=Cumulative production, L^3
q	=production rate, L^3/T
\bar{q}	=average production rate, L^3/T
S	=saturation, dimensionless
R	=swept volume correction ratio, dimensionless
t	=time, T
\bar{t}	=residence time, T

V	=velocity, L/T
V_{Dp}	=Dykstra-Parson coefficient, dimensionless
\bar{V}	=average velocity, L/T
\hat{V}	=swept volume, L^3
σ	=standard deviation

Subscripts

<i>alcohol</i>	=component alcohol
<i>ester</i>	=component ester
<i>eq</i>	=at equilibrium condition
<i>k</i>	=tracer <i>k</i>
<i>o</i>	=oil
<i>or</i>	=residual oil
<i>peak</i>	=peak time
<i>res</i>	=residence time
<i>w</i>	=water
<i>1</i>	=tracer 1
<i>2</i>	=tracer 2

Chapter 3. Estimation of Hydraulic Fracture Volume utilizing Partitioning Chemical Tracer in Shale Gas Formation

3.1 Introduction

Hydraulic fracturing has been applied in shale gas development to increase the contact area with matrix and create permeable conduits for fluid flow. Knowledge of hydraulic fracture volume is essential in determining the stimulation treatment efficiency. However, the fracture volume diagnosis is very challenging because of the complexities of rock property and fracturing process. Davis (2009) summarized capabilities and limitations of numerous fracture diagnostic technologies, including tiltmeters, microseismic mapping and radioactive tracers. Among them, only surface tilt mapping is able to determine the hydraulic fracture volume, while its resolution decreases with depth.

Chemical tracer is a powerful technology for reservoir characterization (Tomich et al. 1973; Sheely Jr and Baldwin Jr 1982; Abbaszadeh-Dehghani and Brigham 1984; Allison et al. 1991). In recent years, its application has been extended in hydraulic fracturing to evaluate contribution of each fracture stage to the total hydrocarbon production in a multi-stage horizontal well (Goswick and LaRue 2014, King and Leonard 2011, Catlett et al. 2013). Chemical tracer can also help understand interwell communication for fractured wells (Crawford et al. 2014).

Chemical tracer is rarely used to estimate hydraulic fracture volume. Gardien et al. (1996) revealed that the tracer response was sensitive to an influence ratio, which was the combination of fracture half-length, fracture height, formation porosity and injected volume. They noticed that tracer response in fractured reservoir was quite

different with a homogeneous reservoir, indicating the possibility of hydraulic fracture diagnosis using chemical tracer. On the other hand, it was impossible to determine the fracture volume directly because fracture width was not included in the ratio. Leong et al. (2015) utilized deuterium tracer to detect the fracture volume based on flowrate and residence time in a well pair setting. They neglected the tracer swept volume in matrix, which could lead to an overestimation of fracture volume eventually. Elahi and Jafarpour (2015) proposed to analyze tracer test data for fracture volume using ensemble Kalman filter. However, this approach is difficult to employ because it required tremendous fracture and matrix information for the data assimilation.

This chapter describes the use of partitioning chemical tracer to estimate hydraulic fracture volume in shale gas formation. To compute the hydraulic fracture volume, method of moments is applied to the tracer production in both phases, gas and water, correspondingly. The impact of tracer invasion into the matrix can be decoupled from the overall tracer data. In addition, impacts of partition coefficient and adsorption are also investigated. Synthetic numerical modeling was used to validate the proposed approach.

3.2 Methodology

For most shale gas formations, more than 60% of injected fracking fluid is not produced back in the early production stage according to the field observations (Crafton 2008). Therefore, for the fracking fluid soluble tracers (conservative tracers), their production history would be either too limited, which may lead to incorrect estimations of fracture volume, or the tracer information is too late to yield useful information. Another type of conservative tracer is gas soluble tracers. Given that gas from the shale

reservoir has a much higher mobility than the fracking fluid and some reservoirs may even have immediate gas production right after completion (Asadi et al. 2008), these tracers are anticipated to quickly flow back. However, on the other hand, gas soluble tracers fail to provide sufficient information about the fracking fluid in the hydraulic fracture, and consequently it cannot accurately evaluate the fracture volume.

Upon previous discussions, this study proposes to use partitioning chemical tracer, which is soluble in both gas and fracking fluid. The partitioning coefficient, K , of tracer is defined as the ratio of tracer mole fraction in gas to its mole fraction in water (Eq. 3-1). Partitioning tracer production data will reflect the both phases that could simultaneously occur in the hydraulic fracture. In addition, it can flow back with gas in a short period of time, suggesting the potential of early interpretation of fracture volume.

$$K = \left(\frac{C_g}{C_w} \right)_{eq} \quad (3-1)$$

3.2.1 Swept Volume Calculation

Method of Moments (MoM) has been widely used to interpret tracer production data. First moment gives the tracer swept volume. For the produced tracer concentration versus cumulative produced volume within phase i , the first moment is calculated as (Oyerinde 2005):

$$V_{i,swept} = \frac{\int_0^\infty V_i C_i dV_i}{\int_0^\infty C_i dV_i} \quad (3-2)$$

Gas and fracking fluid could exist in the hydraulic fracture at the same time. Since partitioning tracer also exists in both phases, its swept volumes in gas and fracking fluid should be taken into account in order to get the total swept volume in

hydraulic fracture. Because the produced volume is measured at surface condition, the formation volume factor (FVF) at producing bottom-hole pressure (BHP) is needed to convert volume from surface to subsurface condition (Eq. 3-3)

$$V_{\text{swept}} = B_{g,\text{BHP}}V_{g,\text{swept}} + B_{w,\text{BHP}}V_{w,\text{swept}} \quad (3-3)$$

3.2.2 Exponential Decline

The tracer concentration declines exponentially in a homogeneous formation near the wellbore. There is linear relationship of $\ln(C)$ versus cumulative production at the later time. This assumption can be used to extrapolate tracer history. Mathematically, the tracer tail can be expressed by (Sharma et al. 2014):

$$C(V) = be^{-aV} \text{ for } V > V_e \quad (3-4)$$

When the fracture exists, the tracer behavior will be different (Gardien et al. 1996). By plotting the tracer tail in a semi-log plot, two distinct linear relationships are observed, which help to distinguish the tracer swept volume in matrix and fracture respectively. The following contents will illustrate how to analyze the tracer tail in a hydraulically fractured shale reservoir in the later section.

3.3 Validation and Discussion

3.3.1 Hydraulic Fracture Volume Estimation

A synthetic numerical model is used to validate the proposed approach in determining the swept fracture volume. In this section, to eliminate the impact of adjacent matrix, only half of the hydraulic fracture is simulated (Figure 3-1 **Error! Reference source not found.**). The fracture half-length is 300 ft and fracture height is

30 ft. Fracture flowing capacity is controlled by conductivity, which is defined constant as 20 md-ft. The fracture width could be larger than the actual width as long as the conductivity is maintained the same (Cipolla et al. 2010). Therefore, in the model, the fracture width is 2 ft and the fracture permeability is 10 md. The fracture properties are listed in Table 3-1. Dispersion, adsorption and capillary pressure effects are neglected in the simulation.

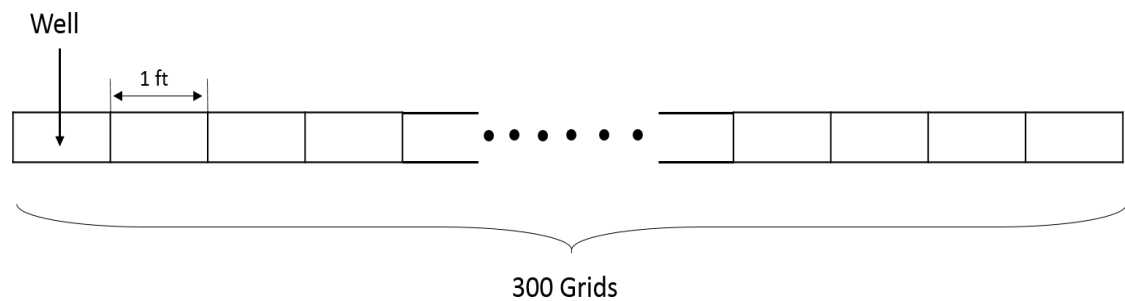


Figure 3-1. Illustration of hydraulic fracture configuration. Each grid is 1 ft long. There are 300 grids and the well perforates at one end.

Table 3-1. Generic Hydraulic Fracture Properties		
Parameter	Value	Unit
Number of Reservoir Grids	(1,300,1)	(<i>x, y, z</i>)
Fracture Half-Length	300	ft
Fracture Height	30	ft
Fracture Width	2	ft
Fracture Permeability	10	md
Fracture Porosity	0.05	fraction

Four steps are followed in the simulations:

1. Inject partitioning tracer as a slug with the fracking fluid;

2. Inject fracking fluid without the partitioning tracer, displacing the tracer farther into the fracture;
3. Shut in the well for a short time interval (water soaking) as the well is not initiated back to produce right after the treatment (Haddad et al. 2015);
4. Open the well to produce gas and fracking fluid as well as the partitioning tracer.

The first two steps are designed to simulate the hydraulic fracturing process. For injection, the well is constrained by the maximum BHP of 20,000 psi and maximum production rate of 2,000 bbl/day. The production minimum BHP is 500 psi. Figure 3-2 shows the details of the well setting.

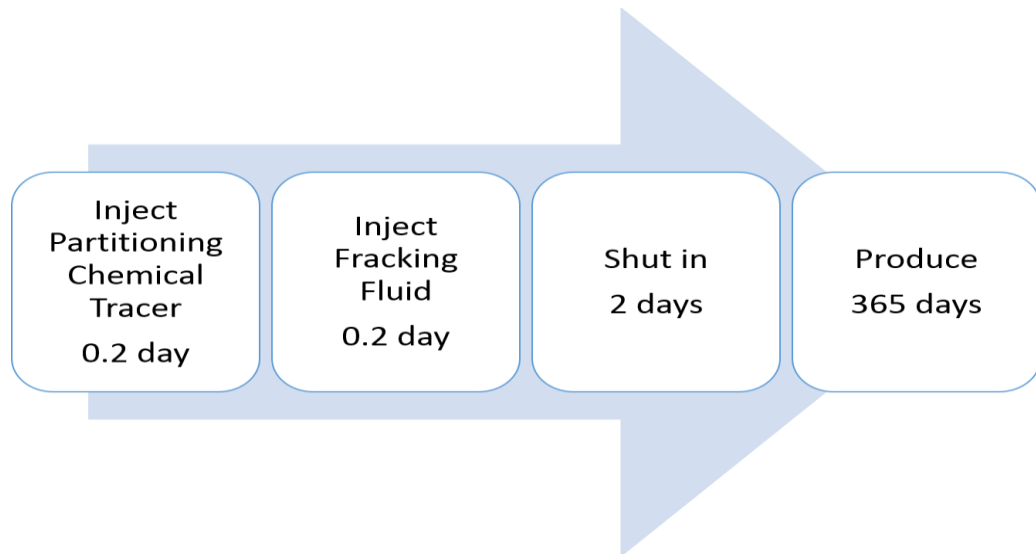


Figure 3-2. The four steps of well plan

Table 3-2. Well Constraints and Fluid Properties		
Well Controls	Value	Unit
Injection Maximum Bottom Hole Pressure	20000	psi
Injection Maximum Rate	2000	bbl/day
Production Minimum Bottom Hole Pressure	500	psi
Water FVF at 500 psi	1.0	rbbl/stb
Gas FVF at 500 psi	0.037	rsf/scf
Water Viscosity	0.3	cp
Gas Viscosity	0.02	cp
Initial Water Saturation	0.3	fraction
Partitioning Coefficient	25	fraction

The initial pressure of hydraulic fracture was 4925 psi. There were two phases, gaseous and aqueous, in the system initially. The aqueous phase represented the initial water and the injected fracking fluid. The gaseous phase stand for the shale gas. Other fluid properties were summarized in Table 3-2**Error! Reference source not found.** To complete the model description, the relative permeability curve for hydraulic fracture is shown in Figure 3-3.

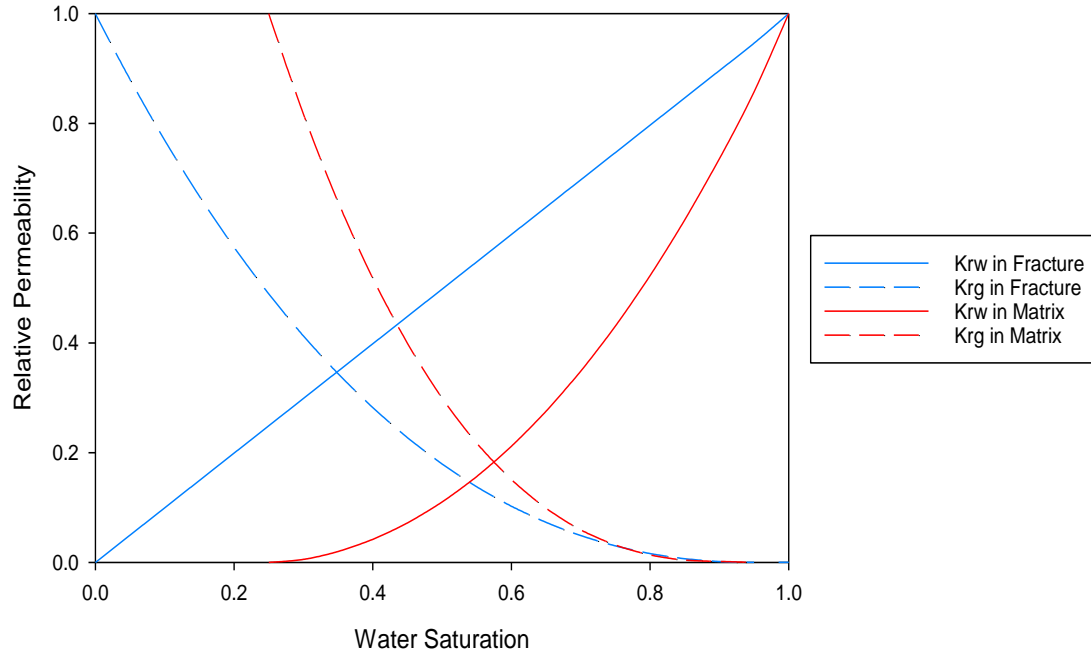


Figure 3-3. Relative permeability curves in matrix and hydraulic fracture (modified from Cheng (2012))

Figure 3-4 is the result of tracer production data in gas in a semi-log plot. The tracer tail section, the red section in graph, could be well fitted by an exponential decline function as shown in the Figure 3-4. Applying Eq. 3-2, tracer swept volume in gas at surface condition is 4605 ft³ and swept volume in water is 122 ft³. The total swept pore volume at subsurface through Eq. 3-3 is 293 ft³.

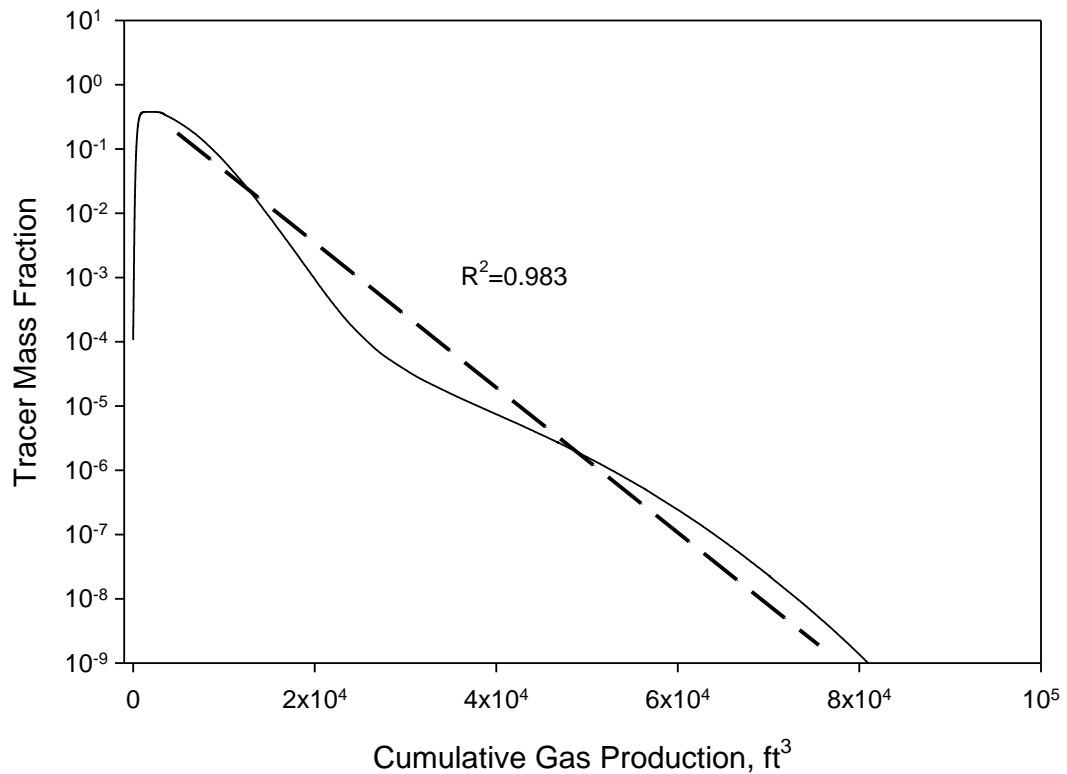


Figure 3-4. Tracer concentration vs. cumulative gas production. The dashed line is the best fitted line. Its R-square is 0.983, indicating the tracer tail is almost a straight line.

Figure 3-5 is the tracer distribution profile at the end of shut in period. The horizontal axis is the distance from the wellbore. It shows that the injected tracer has been pushed to the location of 100 ft away from the wellbore and the total contacted pore volume, if calculated based on Figure 3-5, is 300 ft³. This value is in a good agreement with the previous swept volume obtained from tracer production data.

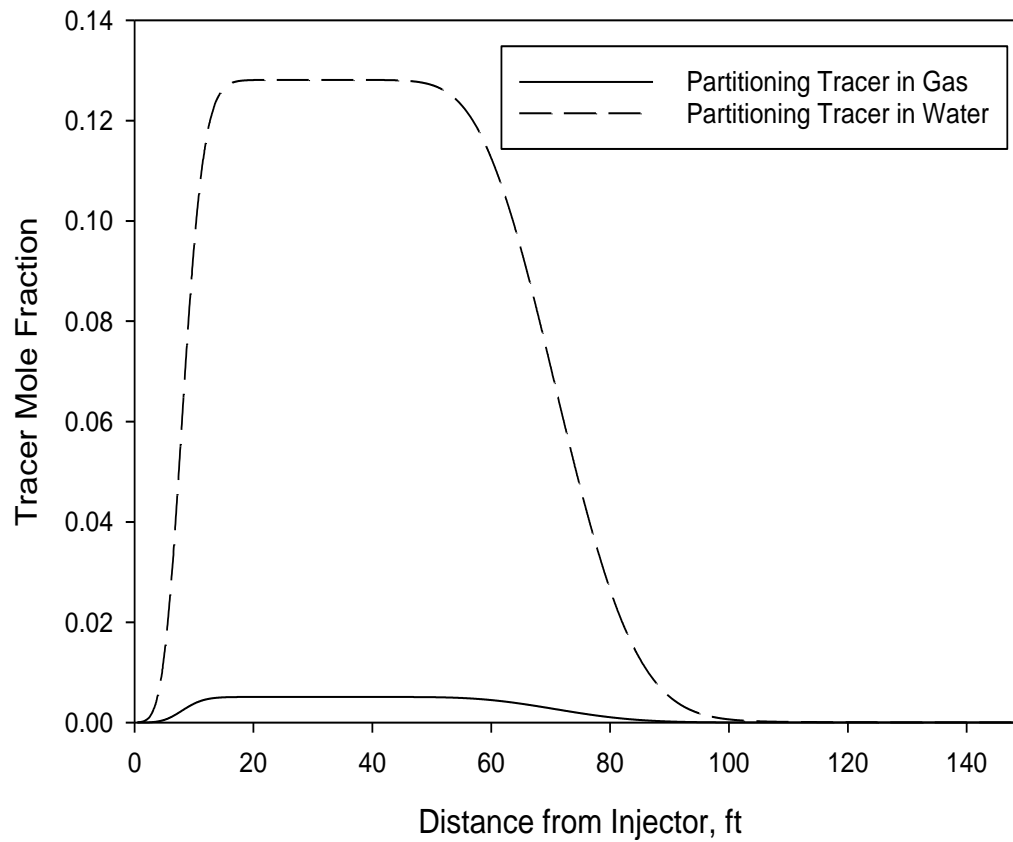


Figure 3-5. Tracer distribution inside fracture at the end of shut in

Although the hydraulic fracture is 300 ft, the tracer only reaches the 100 ft from wellbore because of the pressure increase in the system. The tracer swept volume calculated from Figure 3-4 verifies that MoM is capable in estimating such volume swept by the tracer. In other words, tracer production data could directly tell where the tracer goes during the injection process.

3.3.2 Matrix Impact

Previous case in section 3.3.1 simulates one single hydraulic fracture without matrix. Fracturing pressure is usually much higher than the matrix pore pressure, which leads to the fracking fluid intrusion into the matrix (Warpinski et al. 1998). The penetration distance of fracturing fluid into the matrix is relevant with matrix permeability. For high permeable reservoir, the injected fluid could penetrate deeper and vice versa (Chitrana et al. 2011). Such leak-off would complicate the tracer diagnosis. This section addresses the impact of matrix when using partitioning tracer to detect fracture volume.

Assuming bi-wing model of the fracture, a quarter of the hydraulic fracture and its adjacent matrix are simulated. There are 18 grids in x direction and 50 grids in y direction. The hydraulic fracture is located at the right side, whose x coordinate is 18. Local grid refinement is implemented near the hydraulic fracture with logarithmic grid size (Figure 3-6). Matrix porosity and initial water saturation are kept same with the hydraulic fracture (Table 3-3). With larger matrix permeability, the partitioning chemical tracer may invade deeper into the formation. To investigate the invasion zone impact, matrix permeability varies from 50 nd to 5000 nd. Instead of using the absolute permeability magnitude, a dimensionless permeability ratio of fracture permeability over matrix permeability (Eq. 3-5) was used for comparison. The fluid properties, hydraulic fracture and well information are same with the previous case.

$$R = \frac{K_f}{K_m} \quad (3-5)$$

Table 3-3. Model Dimensions and Matrix Properties		
Parameter	Value	Unit
Number of Reservoir Grids	(18,50,1)	(x, y, z)
Formation Length, y direction	300	ft
Formation Height, z direction	30	ft
Formation Width, x direction	414	ft
Initial Water Saturation in Matrix	0.3	fraction
Matrix Porosity	0.05	fraction

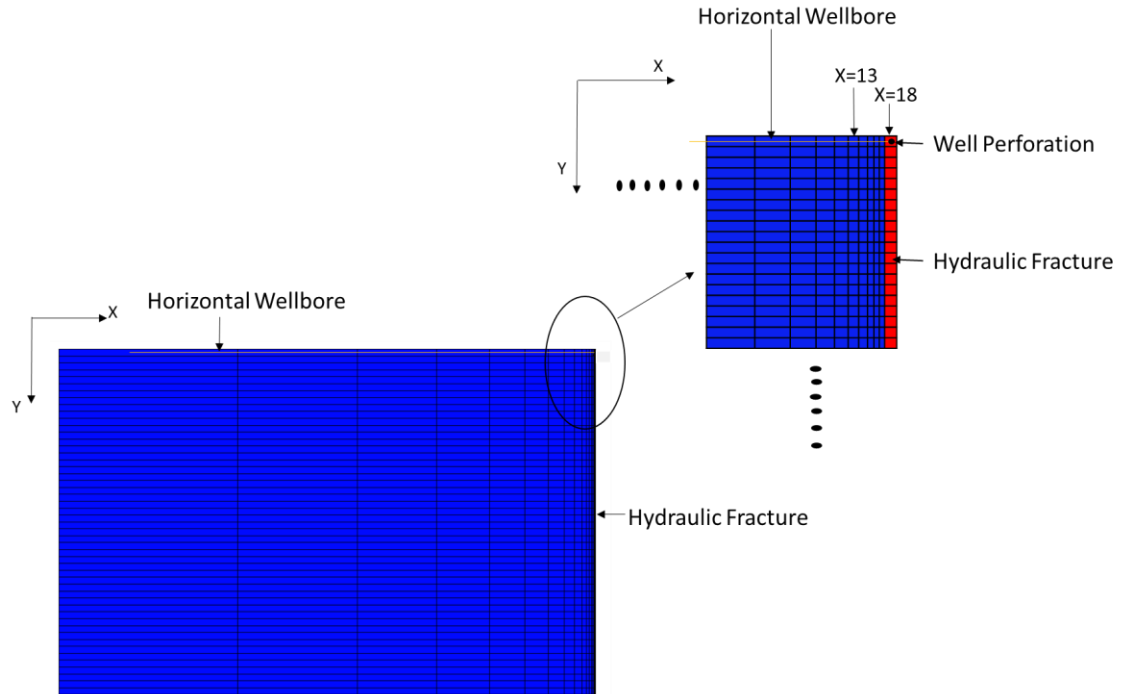


Figure 3-6. Synthetic model configuration with hydraulic fracture and matrix. The hydraulic fracture is on the right side with red color. The horizontal well perforates in the upper right grid. The matrix is in the blue color.

We first validated the grid size selection. The base case had identical grid size of 6 ft in y direction. Its matrix grid size started from 0.45 ft and increased by a factor of

1.45. The grid size standing for hydraulic fracture width was 2 ft as suggested in literatures (Cipolla et al. 2010). There were two cases being created to study the grid size impact. One case had smaller grid size of 3 ft in y direction. The other case had smaller grids size in x direction, starting from 0.2 ft and increased by a factor of 1.2. The grid number was adjusted accordingly to maintain the same pore volume in the model. They were compared with the base case (R=200,000). All the three cases had similar gas and water production. The partitioning tracer production in gas was plotted in Figure 3-7. The tracer's first peak in three cases overlapped with each other, indicating that the grid size in the base case was acceptable even though there was difference in the late tracer tail when grid size in X direction changes,

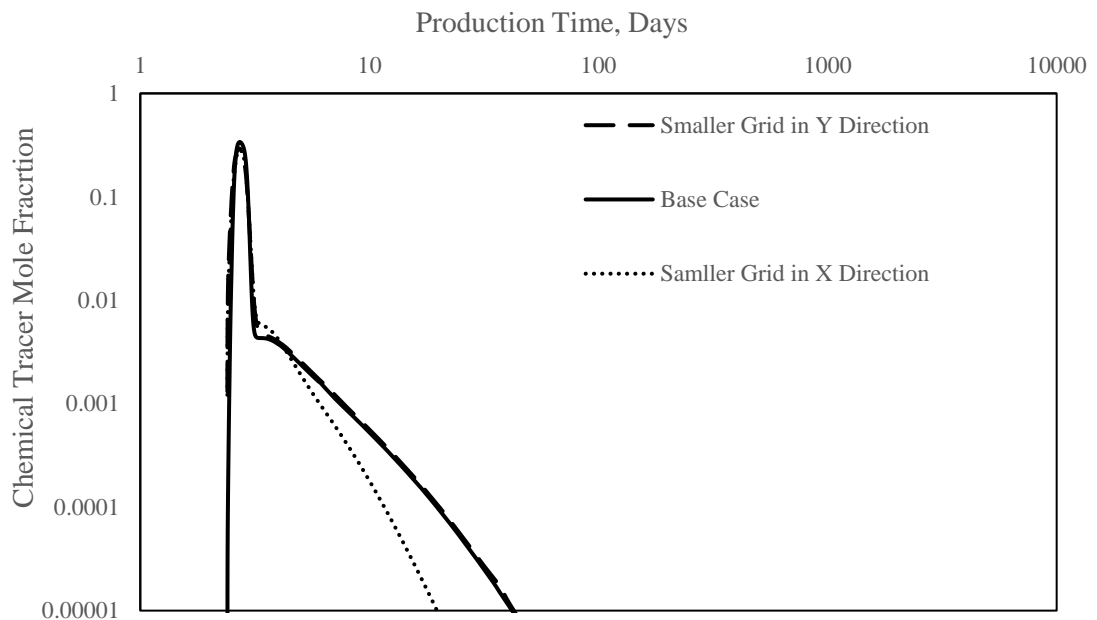


Figure 3-7. Partitioning tracer production in gas.

The solid lines in Figure 3-8 are simulation output of tracer production in gas in a semi-log plot. Its production in water has the similar shape. Based on the direct output

from simulation, the total swept volume for each case is listed in the third row in Table 3-4 using MoM. Figure 3-9 to Figure 3-11 shows the area contact by tracer at the end of shut in period. These graphs are used to compute the tracer contacted volume in hydraulic fracture and in entire system respectively (Table 3-4). In Figure 3-9 to Figure 3-11, columns of $x=18$ indicate the hydraulic fracture.

The results show that the tracer original production data provides the total swept volume rather than the hydraulic fracture volume as the injected fracking fluid penetrates into the matrix and the fluid flow from matrix contributes to the final tracer production besides hydraulic fracture. In addition, with smaller permeability ratio R (i.e. higher matrix permeability), the total tracer swept volume is larger, implying larger invasion zone of the fracking fluid. As shown in Figure 3-9 to Figure 3-11. Such observations suggest that the tracer production data can help estimate the invasion zone if hydraulic fracture volume is known.

Examining the tracer tail in Figure 3-8, two distinct linear relationships of tracer concentration versus cumulative gas production are noticed. This is also observed in water production. For the convenience of discussion, we name the intersection of the two linear lines as the deviation point. We extrapolate the first linear section for both gas and water using the exponential decline rule (Eq. 3-4). The dashed line declines more rapidly after the deviation point compared against the original plot (Figure 3-8). We re-calculate the swept volume based on the extrapolated curve and the results are displayed in the last row of Table 3-4.

For the case of fracture permeability is higher than the matrix permeability, the swept volume obtained from the extrapolated line is closer to hydraulic fracture volume

because less fluid flow contributes to the tracer production at early stage. Since the fracture permeability is much higher than the matrix, the fluid inside hydraulic fracture will come back to the wellbore first. On the other hand, if matrix permeability increases, more matrix fluid with tracer is produced right after production and the deviation point is postponed in the regard of gas production as well. This will result in a larger difference between the hydraulic fracture volume and the corrected swept volume. Therefore, the partitioning tracer could provide a reliable estimation of fracture volume when the fracture permeability is several orders higher than the adjacent matrix permeability.

Above results also indicates that the tracer should be injected as a slug at the beginning of proppant stage, so that it has minimum leak-off into the matrix and it could also inform the entire fracture volume. If injected in the pad stage, tracer will significantly penetrate into the matrix, which influences the fracture volume estimation. If injected too late, tracer can only inform partial fracture volume.

Another advantage of using partitioning tracer for fracture diagnosis is rapid feedback. Once the linear relationship occurs, we can simply use the exponential decline rule to extrapolate the curve without actually measuring the tracer concentration. According to the simulation, the first linear section can be observed within 1-day flowback or even less. The deviation point occurs within 3-day production, indicating the second linear relationship can also be observed very quickly. Nevertheless, only 1/3 of injected fracking is produced back after 1-year production. Such rapid response of tracer is because it partitions and flows back with the fast gas.

Table 3-4. Swept Volume Comparison

Matrix Permeability, nd	50	500	5000
R	200,000	20,000	2,000
Total Swept Volume, ft³	1358	1500	2134
Total Contacted Volume, ft³	1098	1449	2029
Contacted Fracture Volume, ft³	645	642	639
Corrected Swept Volume, ft³	835	1097	1864

(Note: ‘Total Swept Volume’ is calculated using MoM from the original tracer production history (the solid line in Figure 3-8); ‘Total Contacted Volume’ is the total pore volume contacted by the tracer at end of shut in, including matrix; ‘Contacted Fracture Volume’ is the fracture volume contacted by the tracer at end of shut in, not including matrix; ‘Corrected Swept Volume’ is calculated using MoM based on the extrapolated tracer production history (the dashed line in Figure 3-8)).

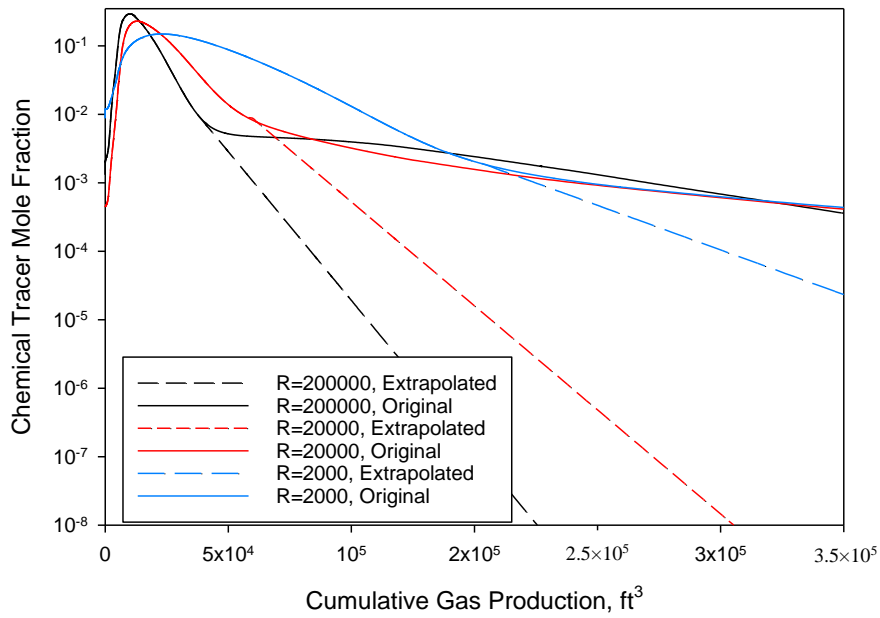


Figure 3-8. Partitioning tracer production data in gas. Solid lines are simulation output. The dashed lines are the extrapolation based on the first linear section. x axis is normal scale and y axis is in log scale.

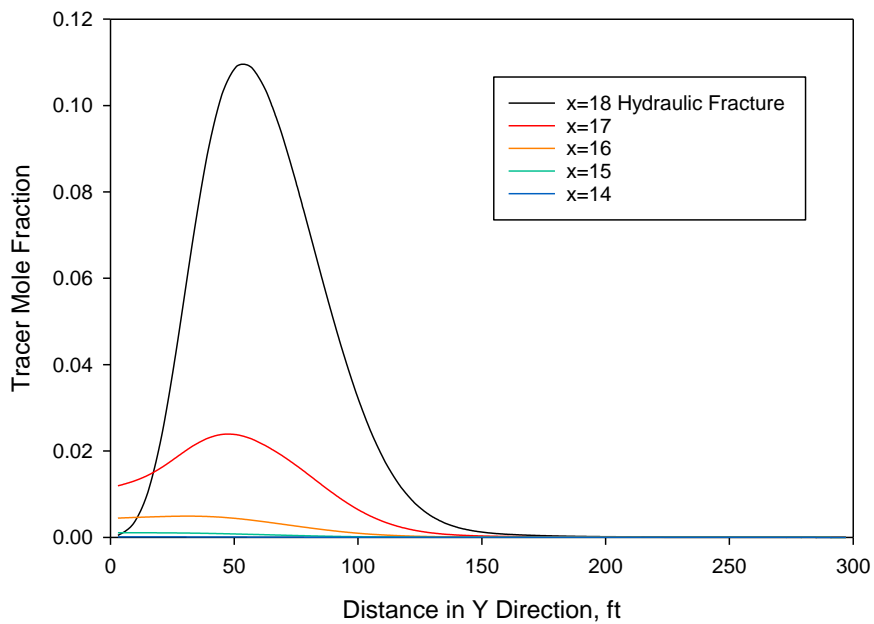


Figure 3-9. The volume contacted with tracer at the end of shut in. R=200000.

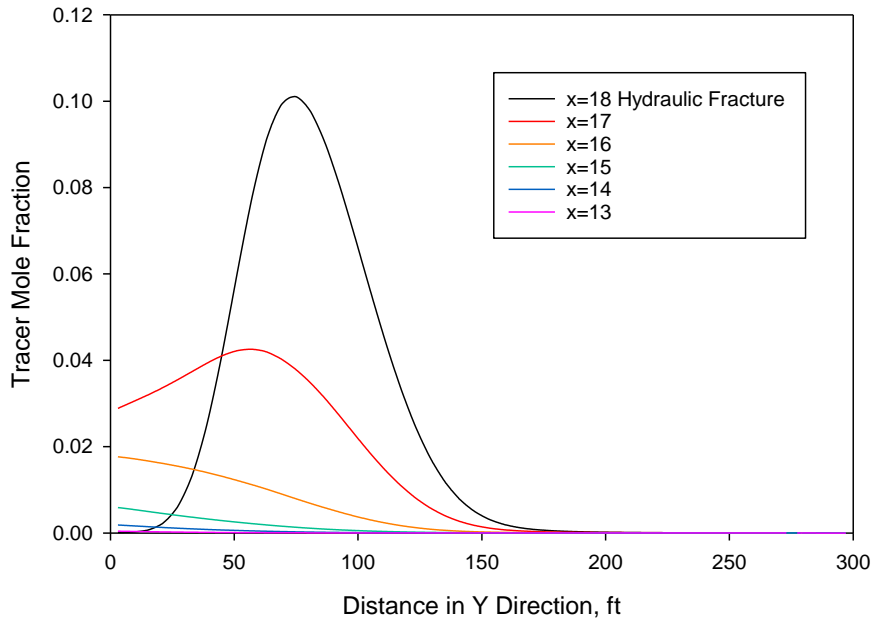


Figure 3-10. The volume contacted with tracer at the end of shut in. R=20000.

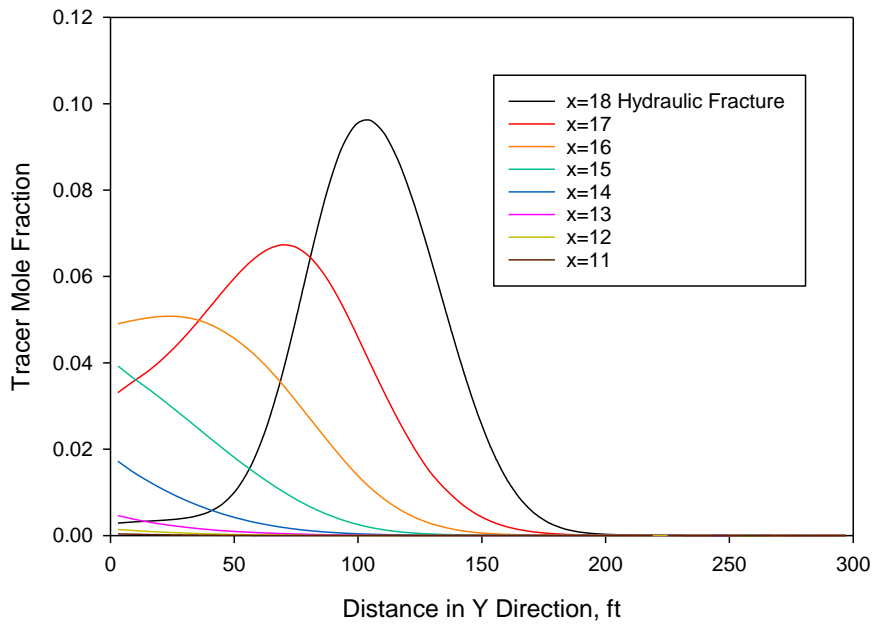


Figure 3-11. The volume contacted with tracer at the end of shut in. R=2000.

3.3.3 *Impact of Partition Coefficient (K)*

Three different partition coefficients were used to investigate the tracer partitioning effect and the results are shown in Table 3-5. The matrix permeability is 50 md and other parameters are kept same with the previous section. The adsorption was not included in the simulations. The solid line in Figure 3-12 is tracer production data in the vapor phase on a semi-log plot. Tracer production in water has the similar shape. The ‘Total Swept Volume’ in Table 3-5 is obtained using MoM according to the direct output from simulation. Figure 3-13 to Figure 3-15 shows the tracer distribution profiles at the end of shut in period. They are depicted on cross-sections in y direction. The decrease of x number indicates the deeper location into the matrix away from hydraulic fracture. We used these graphs to compute the tracer contacted volume in hydraulic fracture and in entire system respectively (i.e. ‘Contacted Fracture Volume’ and ‘Total Contacted Volume’ in Table 3-5 respectively). In Figure 3-13 to Figure 3-15, columns of $x=18$ indicate the hydraulic fracture. The ‘Corrected Swept Volume’ in Table 3-5 was obtained through the dashed line in in Figure 3-12, which was the extrapolation of first section using exponential decline law.

Table 3-5. Comparison of Swept Volume with Different Partition Coefficient			
Partition Coefficient, fraction	2.5	25	250
Total Swept Volume, ft ³	3565	1358	398
Total Contacted Volume, ft ³	1149	1053	374
Contacted Fracture Volume, ft ³	657	600	300
Corrected Swept Volume, ft ³	2014	835	275

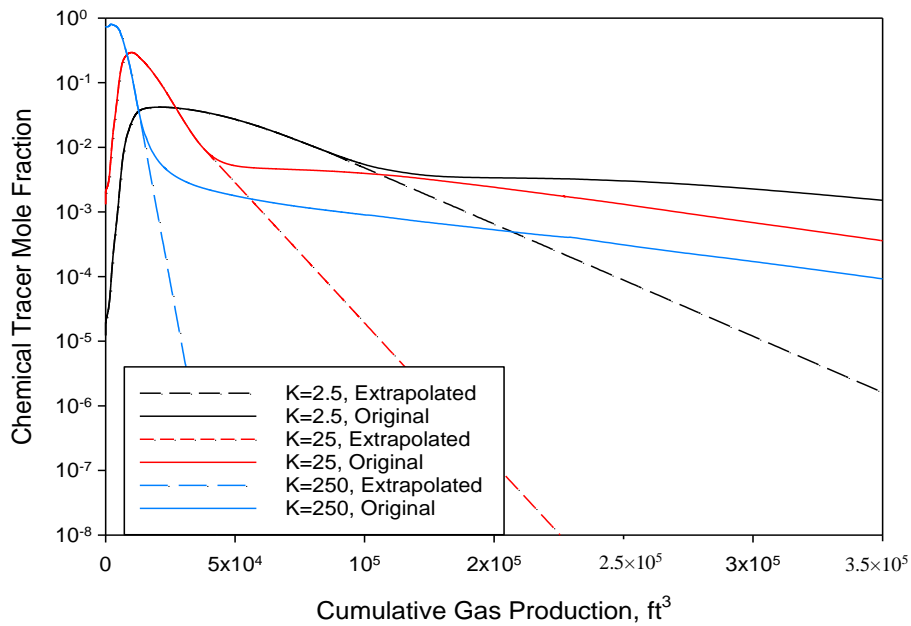


Figure 3-12. Partitioning chemical tracer production data in gas. Solid lines are simulation output. The dashed lines are the extrapolation based on the first linear section. This figure shows the difference between the cases with different partition coefficient (K). x axis is normal scale and y axis is in log scale.

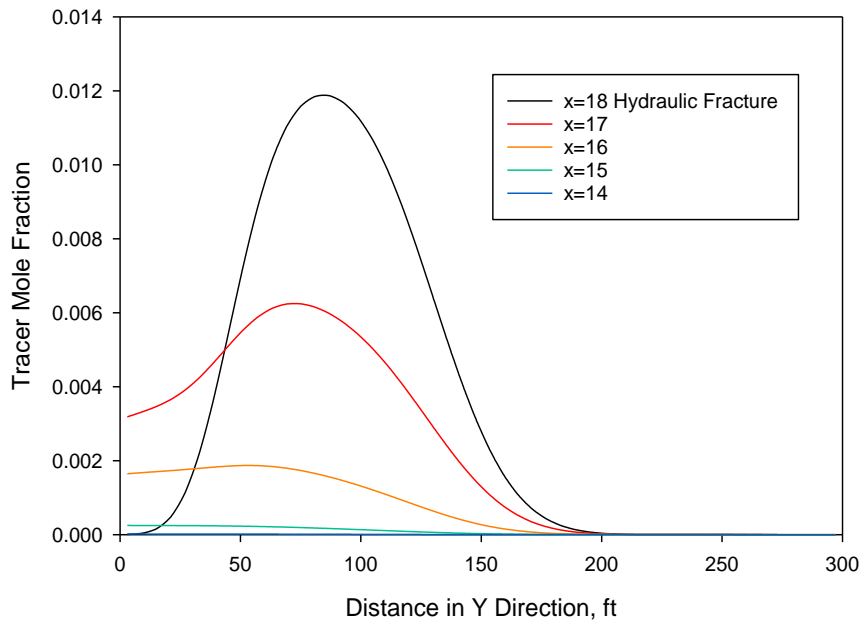


Figure 3-13. The tracer distribution profile inside domain at the end of shut in. $K=2.5$.

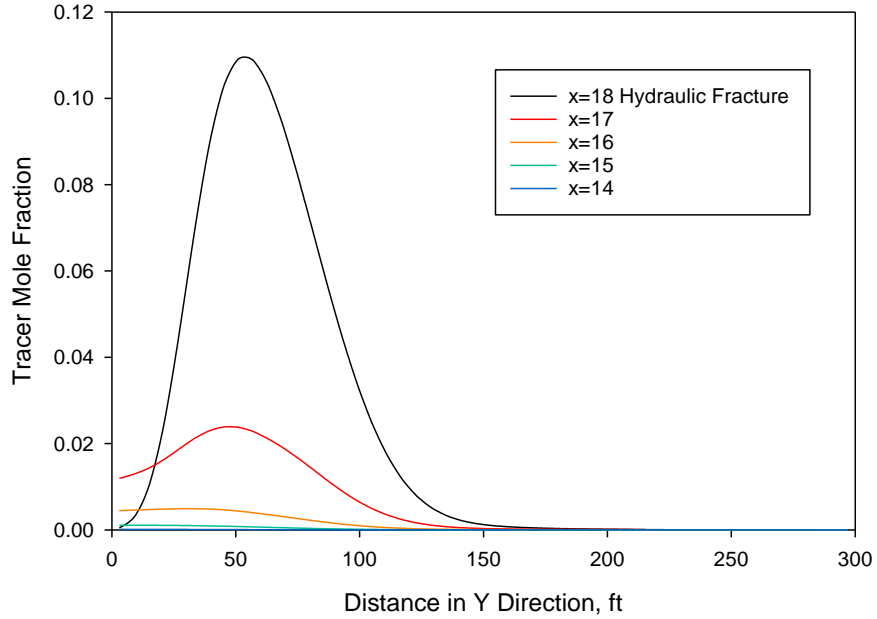


Figure 3-14. The tracer distribution profile inside domain at the end of shut in. $K=25$.

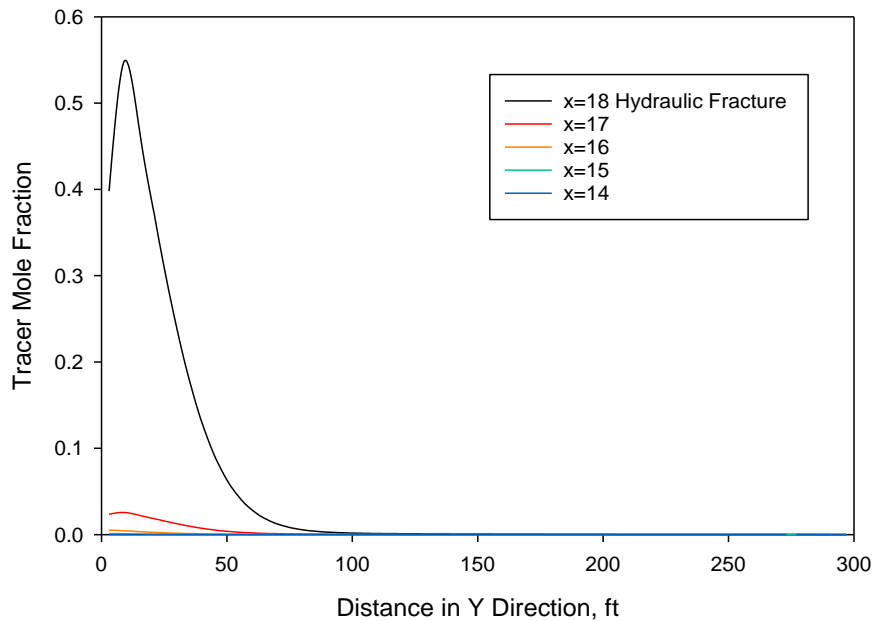


Figure 3-15. The tracer distribution profile inside domain at the end of shut in. K=250.

Figure 3-12 shows that tracer will be produced back faster with a larger partition coefficient because majority of the partitioning chemical tracer will flow with gas. Such observation is in an agreement with the observation in Wu (2006). It indicates that we could obtain tracer response quickly if the partition coefficient is larger.

Entire tracer production data gives a more precise evaluation of the total swept volume with larger partition coefficient as shown in Table 3-5. Additionally, the ‘Contacted Fracture Volume’ is closer to the ‘Corrected Swept Volume’ along with the increase of partition coefficient, indicating that the tracer with a large partition coefficient could provide an accurate estimation of swept hydraulic fracture volume through the extrapolation of first straight section of tracer production tail. For tracer with small partition coefficient, more tracer particles are trapped in the residual water so

that its production is delayed and it fails to accurately assess the hydraulic fracture volume and total swept volume.

Although above two observations indicate that large partition coefficient is favorable to hydraulic fracture diagnosis, it is also noted that the tracer with large partition coefficient only sweeps a small volume of the system. Table 3-5 shows that both 'Total Contact Volume' and 'Contacted Fracture Volume' decrease with the increase of partition coefficient. Figure 3-16 illustrates the fracking fluid distribution at the end of shut in inside hydraulic fracture grid column. It is identical in each case. We can consider actual fracture volume is based on the penetration distance (around 200 ft away from wellbore). Comparing fracking fluid distribution with tracer distribution, we notice that the tracer with larger partition coefficient remains close to the well and such tracer does not travel/penetrate into the fracture as deep as fracking fluid. The reason is that the more tracer particles partitions into the residual gas near wellbore and these particles will not be able to flow farther. Consequently, the tracer with large partition coefficient will only reflect the swept fracture volume, not the actual fracture volume.

A tracer with large partition coefficient could provide an accurate estimation of swept fracture volume, which could be, however, much smaller than the actual fracture volume. On the other hand, the tracer with small partition coefficient could penetrate as deep as fracking fluid, while it might overestimate the actual fracture volume. Therefore, the tracer partition coefficient should be carefully selected considering the balance between investigation volume and result accuracy.

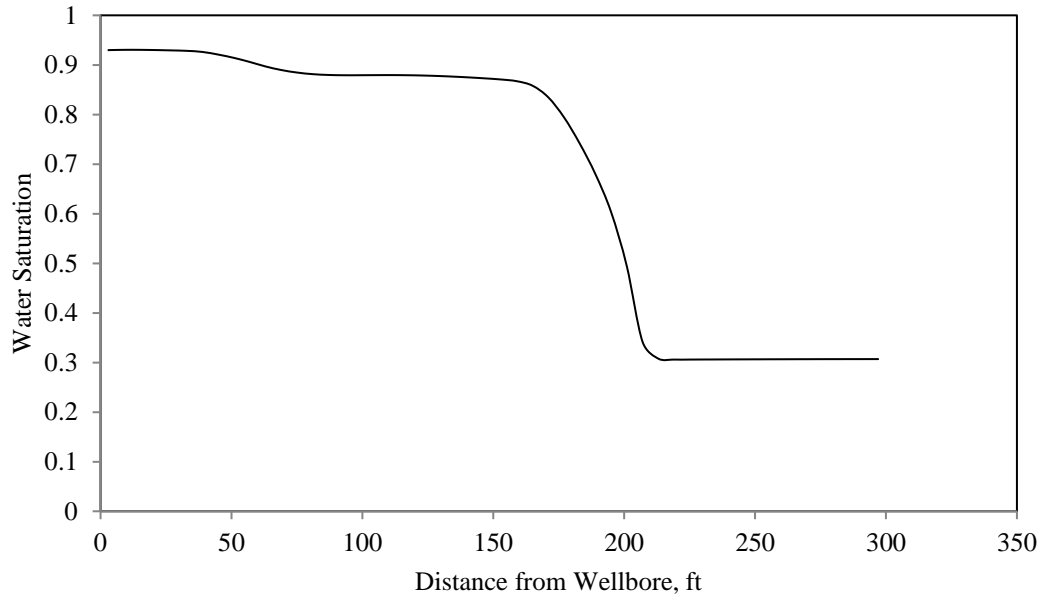


Figure 3-16. Fracking fluid (water) distribution at the end of shut in. Inside hydraulic fracture grid column (x=18).

3.3.4 Impact of Adsorption

Tracer may have the tendency to be adsorbed on the grain surface and affect tracer response. Langmuir isotherm model (Type I) (Langmuir 1918) was applied in the simulations. The governing equation of adsorption is (CMG-STARS User's Guide 2012):

$$ad = \frac{ac}{1+bc} \quad (3-6)$$

Where, ad represents the adsorbed moles of component per unit pore volume. a and b are two parameters.

It was assumed tracer adsorption on fracture and matrix was the same. Each case had the identical b value of 100. The parameter a had three different values to represent different adsorption capacity as shown in Table 3-6. The tracer partition coefficient is 25 and matrix permeability is 50 nd. The meaning of other terms in Table 3-6 is the

same as previous. Figure 3-17 is the tracer production data. Figure 3-18 and Figure 3-19 are tracer distribution profile for cases of medium adsorption and high adsorption respectively. The tracer profile of low (no) adsorption case is the same with Figure 3-8.

Table 3-6. Comparison of Swept Volume with Different Adsorption Parameter			
Adsorption	Low (No)	Medium	High
a, lbmol/ft³	0	0.5	5
Total Swept Volume, ft³	1358	1348	1349
Total Contacted Volume, ft³	1053	820	373
Contacted Fracture Volume, ft³	600	513	279
Corrected Swept Volume, ft³	835	855	974

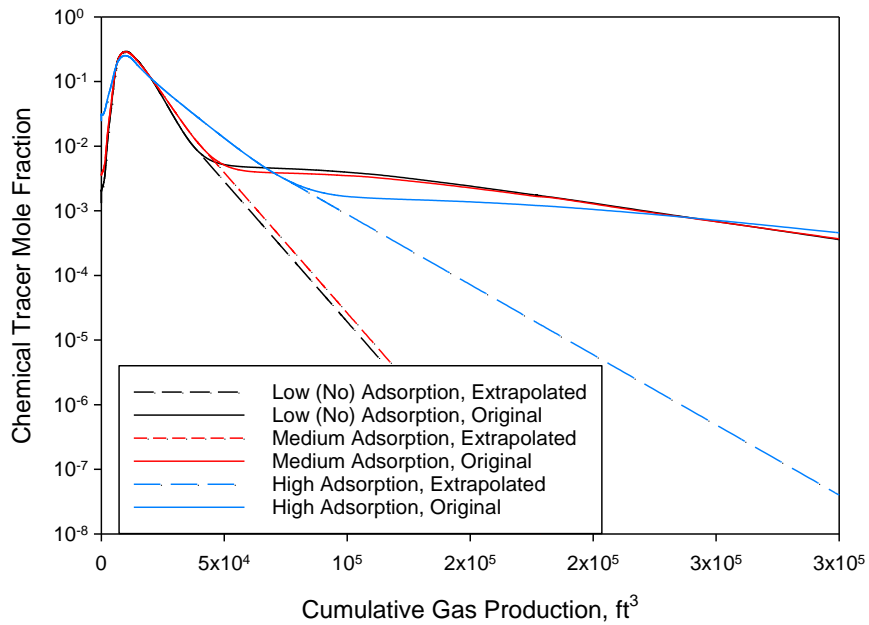


Figure 3-17. Partitioning chemical tracer production data in gas. Solid lines are simulation output. The dashed lines are the extrapolation based on the first linear section. This figure shows the difference between the cases with different adsorption.

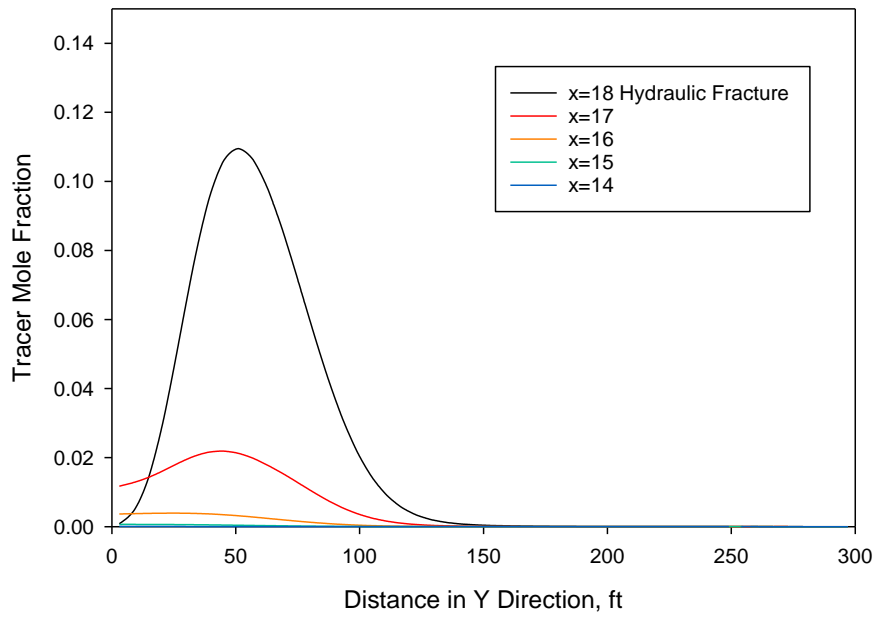


Figure 3-18. The tracer distribution profile inside domain at the end of shut in. Medium adsorption.

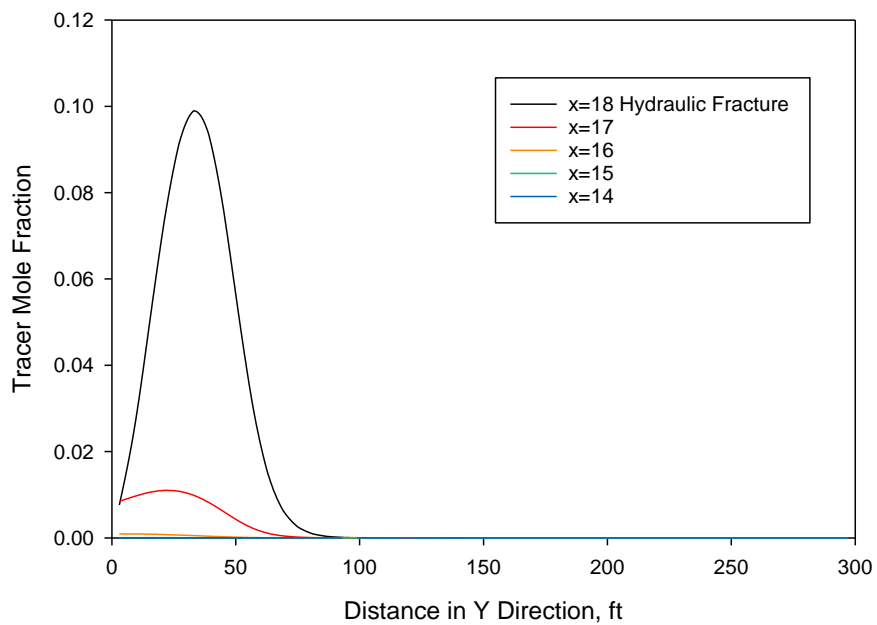


Figure 3-19. The tracer distribution profile inside domain at the end of shut in. High adsorption.

The tracer distribution profile demonstrates that tracer penetrates less into the fracture and matrix when there is adsorption. Tracer particles are adsorbed on the grain surface near the wellbore instead of flowing farther. The tracer production is delayed due to the adsorption as well (Figure 3-17).

Table 3-6 illustrates that the difference between the ‘Total Swept Volume’ and the ‘Total Contacted Volume’ is getting larger with the adsorption. The same trend is also observed for the difference between the ‘Corrected Swept Volume’ and the ‘Contacted Fracture Volume’. This result indicates that the partitioning production data could not provide reliable estimation of the total swept volume or fracture volume. Hence, adsorption should be avoided when selecting the tracer for fracture volume diagnosis.

3.4 Conclusion

This chapter introduces an approach to estimate fracture volume by injecting a slug of aqueous solution containing a partitioning tracer into a shale gas reservoir. The tracer will continuously partition into and out of the liquid water phase. The tracer in solution will penetrate into the rock matrix formation and some of them will be in the fracture. When the well is flowing back, the injected tracers are sampled during the production of gas, and the tracer test can be analyzed for fracturing information. Numerical simulation was employed to validate the use of MoM in estimating fracture volume and the impact of fracking fluid infiltration into the matrix. The impacts of partition coefficient and adsorption are also investigated. Several following conclusions are made:

1. MoM can be used to determine the swept volume of partitioning tracer under two-mobile-phase condition.
2. The tracer production data indicate the total volume of fracture and infiltration zone.
3. Two linear relationships of tracer tail are observed when fracture exists. Extrapolating the first straight section using exponential decline law can estimate fracture volume. Its accuracy is influenced by permeability ratio between 2,000 and 200,000.
4. Partitioning tracer has rapid feedback even though the injected fracking fluid is trapped in the system. The tracer test is therefore time-efficient.
5. Increase the partition coefficient can increase the accuracy of swept volume estimation from tracer production data. The partitioning chemical tracer will also flow back faster if it is more soluble in gas.
6. The tracer with high partition coefficient will not be able to reflect the actual fracture volume. When the partition coefficient is small, the calculated volume does not accurately reflect the swept volume. Therefore, careful selection of partition coefficient is required.
7. The tracer adsorption should be avoided when selecting the tracer for fracture volume diagnosis.

Nomenclature

Normal

ad	=adsorbed moles of component, mol/L ³
a	=First coefficient of Langmuir expression, mol/L ³
B	=Formation volume factor, fraction
C	=Chemical Tracer Concentration, mole fraction
K	=Partitioning Coefficient, fraction
L	=Length, L
h	=Height, L
t	=Time, T
V	=Swept Volume, L ³
w	=Width, L
ϕ	=poroity, fraction

Subscript

a	=Coefficient
b	=Coefficient
BHP	=Bottom-Hole Pressure
e	=End Point
eq	=Equilibrium
g	=Gas
i	=Component i
$swept$	=Swept Volume

w = *Water*

Chapter 4. Random Walk Algorithm to Track Partitioning Tracer

Movement

4.1 Introduction

Finite-difference method and streamline simulations are two widely applied numerical methods to simulate the tracer's movement of advection and dispersion. However, they all have drawbacks. In recent years, RWPT algorithm was applied in petroleum engineering to trace solute transport in porous media (Yi et al. 1994; Jha et al. 2011; Stalgorova and Babadagli 2012). The major advantage of RWPT over finite-difference method based simulators is that RWPT does not need to solve the partial differential equation numerically. As a result, the tracer concentration front is less artificially smeared (Liu et al. 2000). In addition, RWPT takes transvers dispersion into account, which is restricted in the streamline simulation. Nevertheless, current application of RWPT is limited to conservative tracer or partitioning chemical tracer within one-mobile-phase condition (Liu et al. 1999; Benson and Meerschaert 2009). To the best of present knowledge, no work has been done dealing with partitioning chemical tracer with two mobile phases. This chapter proposes a modified RWPT program to resolve such issue.

4.2 Algorithm Description

RWPT uses particles to represent tracer solutes. Each particle is designated as a certain amount of solutes. The movement of particle within each time step is divided into two segments: advection and diffusion. As shown in Figure 4-1, the particle located at A first travels a distance to B due to the advection. After advection step, it starts the diffusion step in both longitudinal and transverse directions respectively. The overall

diffusion displacement is the vector of BE. The particle eventually reaches the position E.

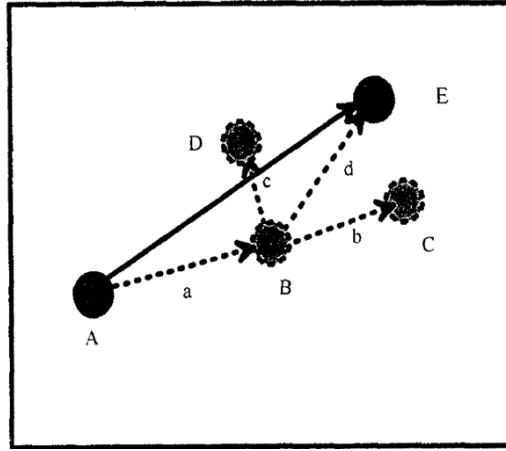


Figure 4-1. Particle movement is consisted by advection and diffusion (Yi et al. 1994).

Mathematically, particle travel distance in x direction $d_{t,x}$ is the sum of advection distance $u_x \Delta t$ and diffusion distance $d_{diffusion,x}$. This relation is also valid in y and z directions if the problem is in 3D.

$$d_{t,x} = u_x \Delta t + d_{diff,x} \quad (4-1)$$

For the partitioning chemical tracer, its advection velocity is related with carrier fluids. For example, ethyl formate (EtFm) partitions between oil and water. Its velocity is a combination of oil velocity and water velocity (Eq. 4-2) (Deans and Shallenberge 1974). The partition coefficient in Eq. 4-2 is mass concentration based instead of mole fraction. Appropriate unit conversion is needed.

$$u_p = \frac{S_w}{S_w + K S_o} v_w + \frac{K S_o}{S_w + K S_o} v_o \quad (4-2)$$

Once velocity field is known, particle advection velocity in each grid cell can be calculated using linear interpolation based on its relative position and velocity at cell faces. In Figure 4-2, the velocity at each wall of grid (i,j) is $u_{i-1/2,j}$ and $u_{i+1/2,j}$

respectively. The particle locates at the black dot, at a distance of $x_{i,j}$ to the left wall. Its velocity in x direction u_x is calculated by (John et al. 2000):

$$u_x = g_x \frac{x_{i,j}}{\Delta x_{i,j}} + u_{i-1/2,j} \quad (4-3)$$

Where, $\Delta x_{i,j}$ is the length of grid cell and g_x is the velocity gradient:

$$g_x = \frac{u_{i+1/2,j} - u_{i-1/2,j}}{\Delta x_{i,j}} \quad (4-4)$$

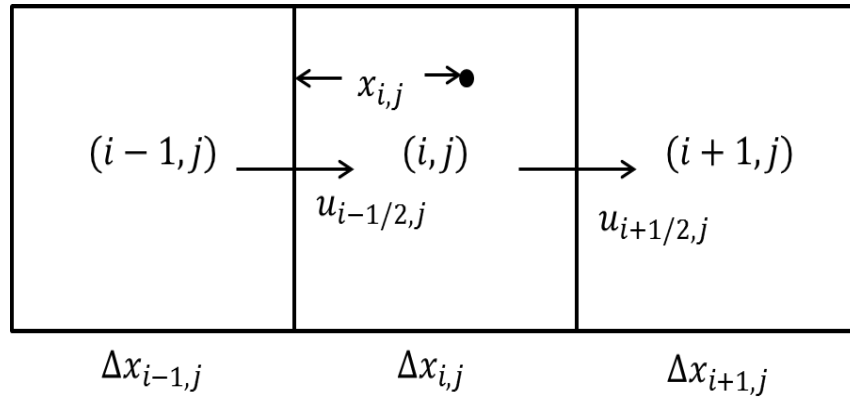


Figure 4-2. Linear interpolation to calculate particle velocity (modified from LaBolle et al. 1996).

Diffusion calculation comes after the advection step. Microscopically, diffusion refers to the random walk of the diffusing particles. This diffusion step follows a normal distribution, with a mean of zero and a standard deviation of $\sqrt{2D\Delta t}$. In x direction, the diffusion distance is calculated by (Scheidegger 1954):

$$d_{\text{diff},x} = z\sqrt{2D_x\Delta t} \quad (4-5)$$

Where, D_x is diffusion coefficient in x direction and z is a random number following standard normal distribution.

Therefore, the total movement of particle in each time step is calculated based on advection and diffusion. The new location (i.e. position E in Figure 4-2) will be set

as the start point of next time step. When a particle reaches the producer, it is assumed to be produced out of the reservoir. By recording the arrival time of each particle to the producer, tracer production data is easily obtained. The advection velocity in RWPT is calculated based on the pressure and saturation output from finite-difference based simulation.

4.3 Program Validation and Result

4.3.1 Model Description

A 1D model with 50 grids was built to validate the modified RWPT program with finite-difference method based simulator. The dimension of each grid was identical: 1 ft. in length with a cross-section of 10 ft². Water and oil were assumed as the two phases in the system. Their compressibility was neglected. Partitioning chemical tracer EtFm was continuously injected at a constant rate of 1.5 bbl./day from one side and produced from the other side of the system at the same rate (Figure 4-3). The partition coefficient was 25.62 (mole fraction based). All the input parameters of base case are given in Table 4-1. The relative permeability curve shows the residual oil saturation was 0.1 (Figure 4-4). This indicated that only water was flowing in the base case. The velocity field used in RWPT was obtained from the finite-difference based method.

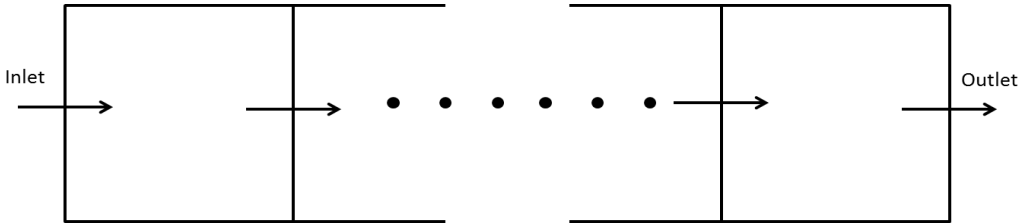


Figure 4-3. Configuration of 1D model. The partitioning chemical tracer is injected from left to right. Its concentration is recorded at the outlet.

Table 4-1. Input parameters of base case		
Parameter	Value	Unit
Length	50	ft.
Cross Section Area	10	ft ² .
Permeability	100	md
Porosity	0.1	%
Oil Saturation	0.1	%
Injection/Production Rate	1.5	bbl./day
Tracer Diffusion Coefficient	0	ft ² /day
Tracer Partition Coefficient	25.62	fraction

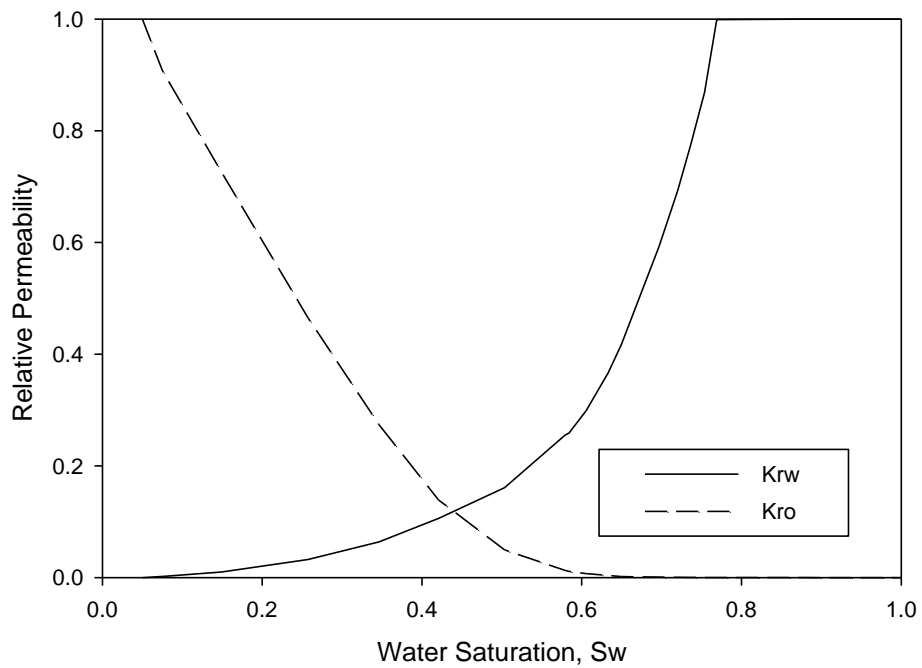


Figure 4-4. Relative permeability curve.

4.3.2 Validation

Figure 4-5 shows the result comparison between analytical solution, finite-difference based simulation and RWPT simulation using the base case input data. In this figure, the Peclet number was infinity (diffusion coefficient is zero). Figure 4-6 is the result comparison with tracer diffusion coefficient of 10 ft²/day in water (other parameters were kept same with the base case). The Peclet number was 45. In both figures, the analytical solution is obtained through Eq. 4-6 (Peters 2012).

$$C_D = -\frac{1}{2} \left[\operatorname{erf} \left(\frac{x_D - \frac{t_D}{R_F}}{2 \sqrt{\frac{t_D}{R_F N_{pe}}}} \right) - \operatorname{erf} \left(\frac{x_D - \frac{t_D - t_{DS}}{R_F}}{2 \sqrt{\frac{t_D - t_{DS}}{R_F N_{pe}}}} \right) \right] \quad (4-6)$$

Results clearly show an obvious difference between the analytical solution and finite-difference based simulation. The RWPT matches the analytical solution well. Both figures demonstrate that the modified RWPT program is more accurate than the simulators that utilize finite difference method in describing the diffusion involved transport phenomenon. Finite-difference based simulation can improve result accuracy by using smaller grids, which may significantly increase the computation time (Stalgorova and Babadagli 2012). The limited number of particles used in the simulation causes fluctuation at the later time for the RWPT result is caused by the. In this case, 200 particles were injected during each time step. This number balanced the calculation time and result accuracy.

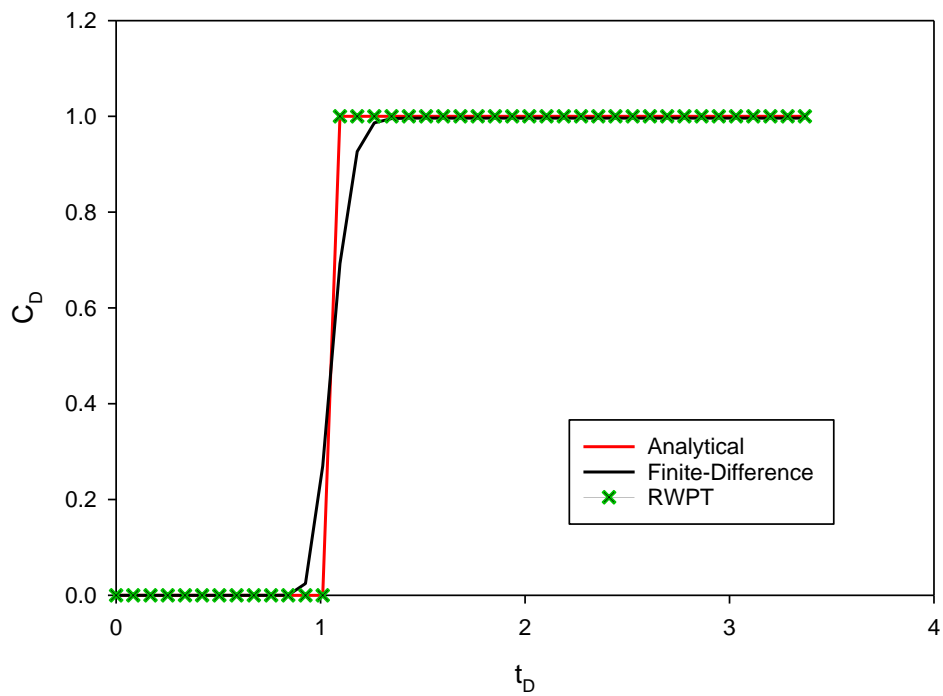


Figure 4-5. Comparison of RWPT with analytical solution and finite-difference. Peclet number is infinity (base case). Immobile oil.

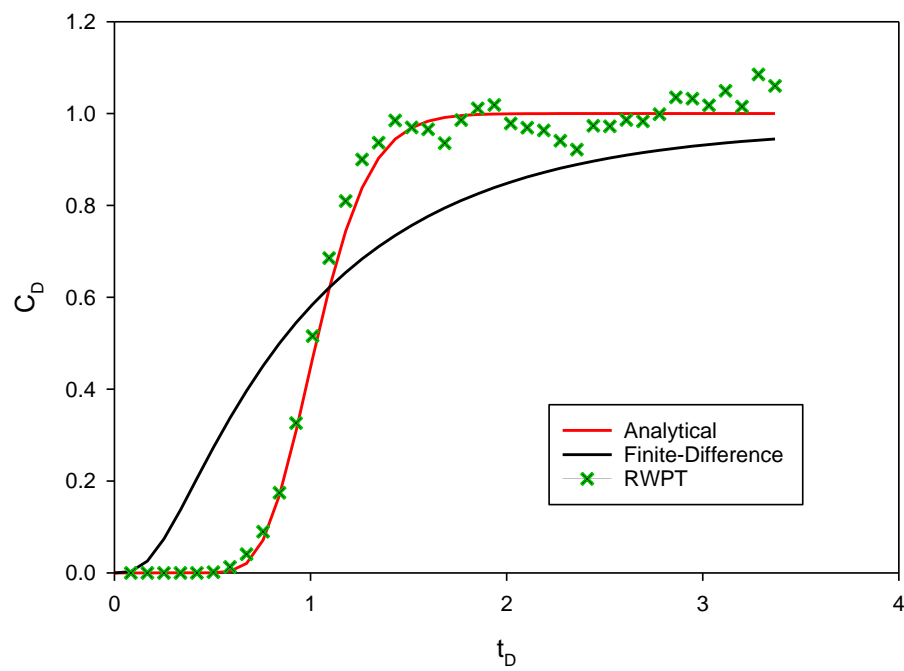


Figure 4-6. Comparison of RWPT with analytical solution and finite-difference. Peclet number is 45. Immobile oil.

4.3.3 Partitioning Tracer Movement with Two Mobile Phases

Strict assumptions of the analytical solution make it unsuitable for complex reservoir application. This drawback makes the RWPT a good approach when fluid flows in multi-dimensions or when the fluid flow is getting complex. Figure 4-7 shows the comparison between RWPT and finite-difference method with two flowing phases. In this case, the initial oil saturation was 0.5. Unlike previous steady-state flow, the velocity field was updated after each time step in RWPT. It is seen that finite-difference based simulation provides a much earlier breakthrough of tracer production. Such comparison indicates that RWPT is also applicable when there are multiple mobile phases.

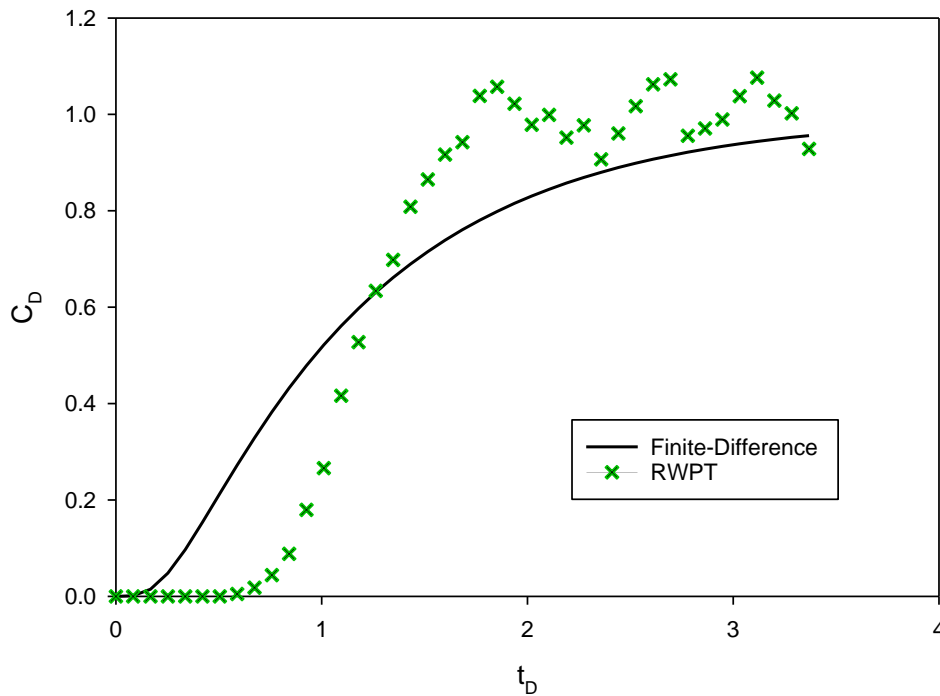


Figure 4-7. Comparison of RWPT with finite-difference. Peclet number is 45. Mobile oil.

Nomenclature

Normal

b	=Coefficient
C	=Chemical tracer concentration, mole fraction
D	=Diffusion coefficient, L^2/t
d	=Displacement, L
g	=Velocity gradient, $1/T$
K	=Partition coefficient, fraction
N_{pe}	=Peclet number, dimensionless
R_F	=Retardation factor
S	=Saturation, fraction
t	=Time, t
u	=Velocity, L/t
v	=Phase velocity, L/t
w	=Width, L
x	=Distance, L
z	=Random number, dimensionless

Subscript

D	=Dimensionless
$diff$	=Diffusion
(i, j)	=Grid location
o	=oil

p =partitioning tracer

w =Water

t =Total

x = x direction

Chapter 5. Quantitative Estimation of Radon Production from Marcellus Shale Gas Reservoirs

5.1 Introduction

Shale gas production is rapidly increasing and it brings remarkable economic interests in recent years. Technologies, such as hydraulic fracturing and horizontal drilling, enable the operators to target on shale formations that are now much easier and cheaper to explore and produce. Nowadays, shale gas production provides a large portion of total natural gas production within U.S. According to Environmental Information Administration (EIA), shale gas made up 40% of total natural gas production in 2013, which was mainly contributed by states of Texas, Pennsylvania, Louisiana and Arkansas (EIA 2014). Counties where shale gas is extracted have seen obvious increases in average incomes, jobs, and wages ranging between 10% to 20% and the unemployment in these counties are lower than other places within the U.S (Fetzer 2014).

Meanwhile, the public has raised numerous debates about radon production from shale formations and its negative environmental impacts, and radon is one of them. Radon is a colorless, odorless and radioactive inert gas. Its most stable isotope is ^{222}Rn with a half-life of 3.8 *days*. Darby et al. (2005) revealed that residential radon is responsible for about 2% of death from lung cancer in Europe. Scientists estimated that 15,000 to 22,000 lung cancer deaths in the United States each year are related to radon as well (NCI 2011).

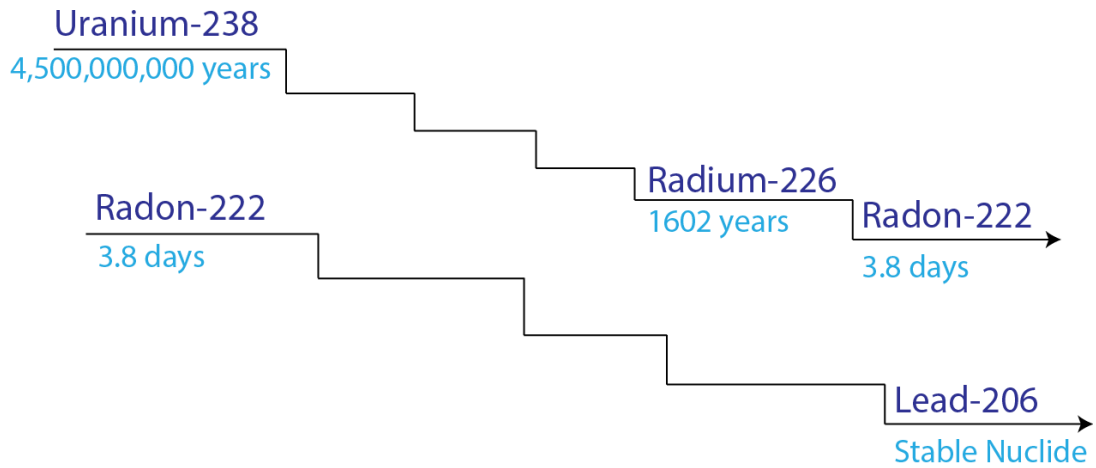


Figure 5-1. Radioactive decay process from Uranium to Lead (modified from Allthingsradon (2009))

Radon in shale formation originates from the decay of radium as the daughter product, one intermediate step in the decay chain through uranium to lead (Figure 5-1). It has been discovered that uranium concentration in shale formation is the highest among other common formations (**Table 5-1**). Recent measurements showed uranium concentration in shale reached to 30,000 *pCi/L* or even higher (Resnikoff 2011). With respect to radium, Nelson et al. (2014) measured radium concentration in hydraulic fracturing flowback water was 17297 *pCi/L*. Kondash et al. (2013) also mentioned flowback water contained unusual high level of naturally occurring radioactive materials in the form of radium isotopes. These imply that gas production from shale formation could be accompanied with severe environmental hazards related with radon. Some on site measurements of radon concentration have a medium of 37 *pCi/L* (Rowan and Kraemer 2012), which is higher than the safe standard of 4 *pCi/L* (EPA 2012). In addition, radon concentration was measured as 17 *pCi/L* inside pipeline (Anspaugh 2012). All above evidences show that there could be substantial amount of radon

existing in shale gas. For the benefit of public health, it is important to quantitatively evaluate the radon concentration from fractured wells in shale reservoirs.

Table 5-1. Uranium Concentration in Different Rocks (Andrews and Wood 1972).	
Rock Type	Uranium Concentration, <i>pCi/L</i>
Shale	4000-30,000
Carbonate	2000
Sandstone	386

There is limited research work focusing on radon production from hydraulic fractured shale gas wells. Resnikoff (2011) simulated radon transport and production from shale gas reservoirs. Results showed that the radon concentration at wellhead ranged from 36.9 *pCi/L* to 2576 *pCi/L*. However, his model did not consider the impact of hydraulic fracture, which increases the surface area for shale gas as well as radon to release and creates a “highway” for them to transport to the surface. In addition, no other work was found discussing the relation between shale gas production/operation protocols and radon wellhead concentration.

This chapter, with a focus on Marcellus shale reservoir, quantitatively evaluates radon concentration at wellhead through synthetic simulation by coupling radon generation, recoil, decay and transport in the subsurface. A quadrant of single hydraulic fracture with its stimulated reservoir was modeled. Natural fractures were also included to examine its effect on radon concentration at wellhead. This chapter also includes the investigation of pore shape and pore size distribution. The primary results show that radon concentration at wellhead is noteworthy. Afterwards, a sensitivity analysis was

conducted by changing input parameters one by one within their practical range. The results provide a better understanding about the parameters that could affect the radon wellhead concentration and suggest feasible actions to control environmental damage from shale gas production.

5.2 Marcellus Shale

Marcellus shale in the Appalachian basin is a middle Devonian-age shale and lies between limestone and shale (Hamilton Group) (DOE 2009). Pennsylvania has become the second largest shale gas producing state because of the Marcellus shale production (EIA 2013). In order to economically produce natural gas from extremely low permeable shale formation, operators rely on hydraulic fracturing to increase the reservoir contact area, creating high permeable conduits for natural gas to flow (Montgomery and Smith 2010).

5.2.1 Porous Media

Understanding the characteristics of shale gas porous media is essential to estimate the radon in-situ concentration and predict its wellhead concentration later on. Shale pores are divided into two types: organic pores and inorganic pores. (Organic pores are expected to contain hydrocarbons while inorganic pores contain water (Wang et al. 2014)). Water plays an important role in radon generation because water can more effectively trap ejected radon in pores than gas. The reservoir model assumes that water fills the pores from smaller size to larger size, which is also known as the blocked configuration (Nielson et al. 1984) (Figure 5-2) (Passey et al. 2010). Pore sizes in the shale formation vary dramatically and usually people use the pore size distribution to

characterize it. For example, a study of pore size distribution in shale gas formation showed that around 10% of pore volume (PV) consisted of pores with diameter less than 1.2 *nm*, 45% of PV was occupied by pores with diameter between 1.3 *nm* and 30 *nm* and the rest 45% of PV had pore size larger than 30 *nm* (Mosher et al. 2013).

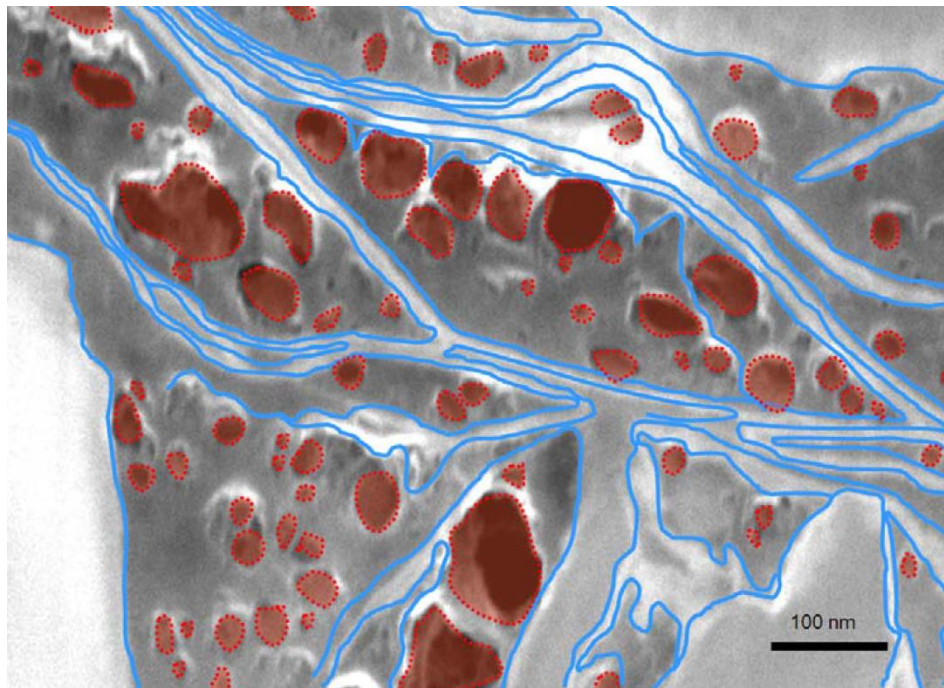


Figure 5-2. Gas is stored in spherical pores (the red color) and water is in slit pores (the blue color) (Passey et al. 2010).

Shale formation has natural fractures that provide highly conductive tunnels and contribute to gas production (Gale and Holder 2014). Hence, the impact of natural fractures with a width of 50 *nm* (Gale et al. 2010) is considered in this study. The natural fractures are assumed to contain both gas and water with an initial water saturation of 0.25.

5.2.2 *Experimental Methods*

The Marcellus shale sample used for this study was obtained from a gas producing well. The sample has a total organic carbon (TOC) of 4.1 wt% and clay content of 72 wt%, with illite as the dominant clay. Five grams of the sample were crushed to a particle size less than 150 μm (100 mesh). One gram of the crushed homogenized powder was collected and degassed at 373K under vacuum for twelve hours, prior to the subcritical nitrogen gas adsorption measurements. Nitrogen isotherm adsorption measurements were conducted in subcritical temperature (49.3K), to allow the condensation of nitrogen gas onto the pore walls. Pore volume is measured by the number of molecules needed to fill the pore space at different relative pressures.

A Density Functional Theory (DFT) statistical model was used to determine the pore size distribution. Unlike other analysis methods, this approach took into account the concentration of pores whose sizes are in the order nanometers (Lastoskie et al. 1993). It assumes that the pores act independently and contribute to the total isotherm adsorption in pore size distribution calculations. Lastoskie et al. (1993) and Adesida et al. (2011) provided more details of using DFT and the derivation of the pore volume calculation.

Scanning electronic microscopy (SEM) was also applied to observe the pore structure of shale sample. In order to receive a smooth surface, the sample was polished in sequence using 400, 600 and 800 grit abrasives and the surface was broad beam argon ion milled before SEM images were taken.

5.2.3 Pore Characterization

Backscattered SEM images are shown in Figure 5-3. Both spherical and slit shape pore exist in the sample. In general, organic pores have spherical shape. On the other hand, the large fractional volume of illite caused the inorganic pores to exhibit slit shape.

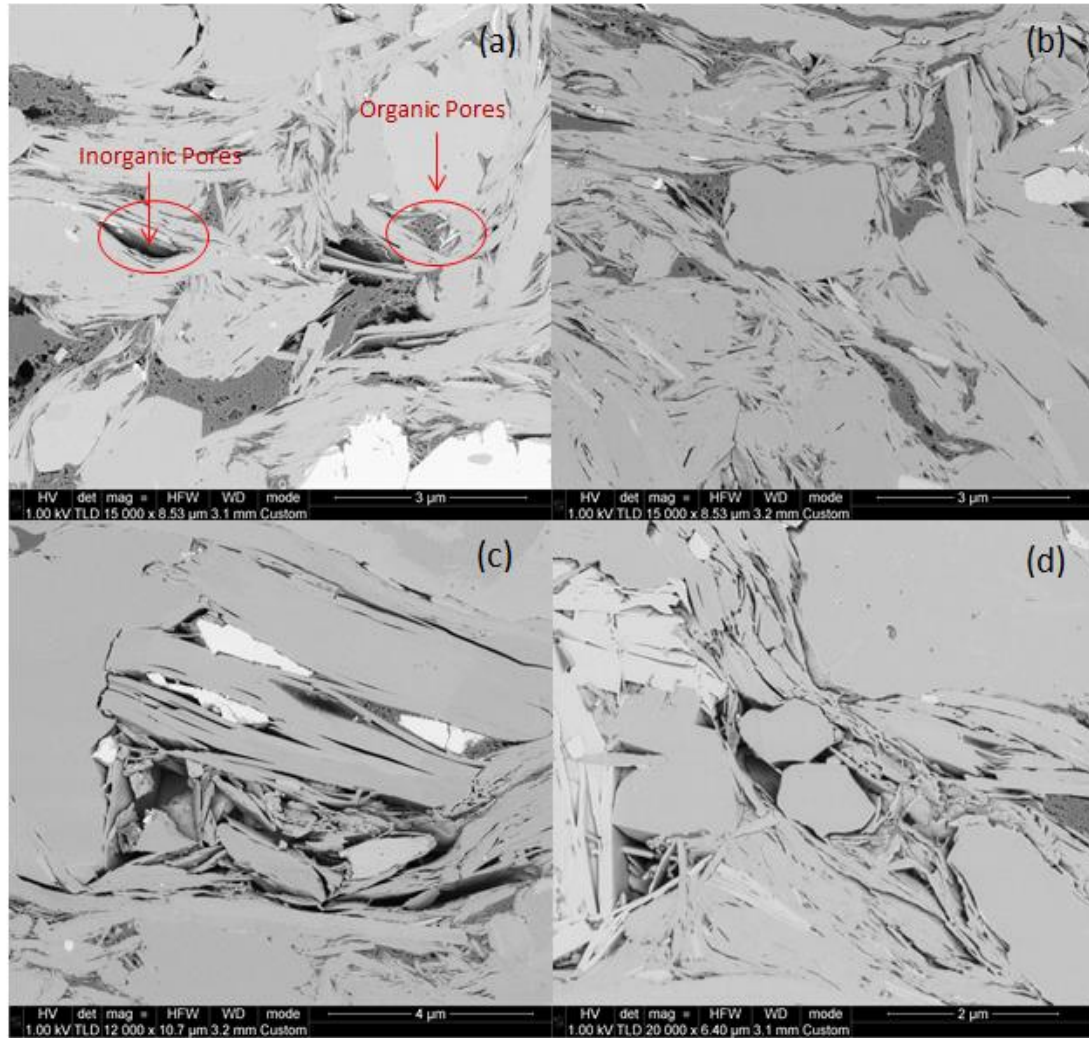


Figure 5-3. Backscattered SEM images for Marcellus shale. (a) Shows organic and inorganic pores at 3 μm. The inorganic pores show slit shape and organic pores shows spherical shape. In (b), the image shows more slits and sheets of illite. Illite is the dominant matrix mineral and is more visible as sheets in (c) and (d), creating inorganic pores around the sample.

Since both geometries are observed in SEM images, two distinct pore size distributions are obtained using DFT based on slit and spherical pore shapes respectively. For simplicity, in each calculation, all the pores are assumed either slit or spherical shape. As shown in Figure 5-4, the solid line represents pore size distribution for slit shape model, and the dashed line stands for the spherical shape pores. For the slit shape pores (Case A), the pore size is related to the pore width, the separation between grain plates (Newman and Thomasson 1979). In this case, it is noticed that the majority of pore volume consisted of pores with a size about $10nm$. The overall pore size ranges from $2\sim 200nm$. On the other hand, the pore size for spherical pores (Case B) is related to the pore radius. Its distribution is generally shifted to the larger size compared with distribution of slit model.

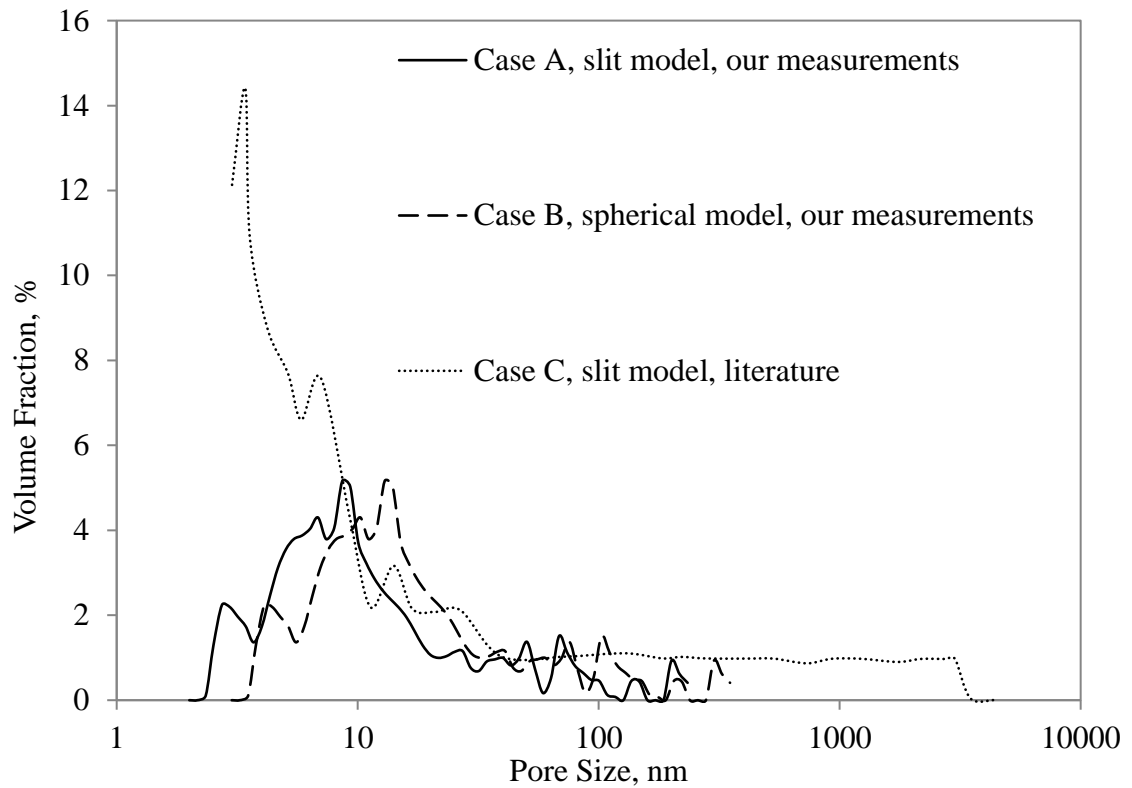


Figure 5-4. Pore size distribution for Marcellus shale. Case A and Case B are calculated through DFT using the adsorption measurements. Case C is obtained from literature (Chalmers et al. 2012).

Pore size distribution may vary from location to location within the same formation. Case C in Figure 5-4 shows a distinct pore size distribution for Marcellus shale with the assumption of slit pore shape (Chalmers et al. 2012). Although it assumes the same pore shape with Case A and both cases are from Marcellus shale, the distribution is obviously different. Most pores in Case C have the pore size of 3nm, which is smaller than Case A, and Case C has a wider range of pore size. Case C was selected to study the impact of pore size distribution by comparing with Case A in the following sections.

5.3 Radon Generation in Pore Space

5.3.1 Recoil Range

The radon atoms acquire kinetic energy after the alpha decay of radium. This energy defines a finite distance, known as the recoil range (Hecter 2005). The kinetic energy allows the radon atoms to travel inside materials. Once the atoms lose all the energy, they stop moving. This process is known as alpha recoil. The distance traveled is material dependent. Usually, solid materials like rock grain require more energy than air to travel the same distance. In other words, radon recoil range is shorter in the material with a higher density. Typically, recoil range in rock, water and gas is $36nm$, $100nm$ and $60,000nm$, respectively (Hecter 2005).

5.3.2 Slit Shape Pores

5.3.2.1 Emanation from Grains to Pores

Radon emanation is the process of radon transferring from mineral grains into pore spaces and this process is mainly controlled by direct recoil after alpha decay of radium (Barillon et al. 2005). Radon diffusivity in rock materials at $300 K$ ranges from $10^{-31} m^2/s$ to $10^{-69} m^2/s$ (Amirkhanoff et al. 1961). Given that the radon's half-life is 3.8 days, diffusion contribution to radon emanation is negligible. Therefore, direct recoil is the main mechanism to consider. Direct recoil, which governs the radon release, may only happen at the position whose distance to grain surface is shorter than the recoil length. Eq. 5-1 was proposed by Hammond et al. (1988) to estimate the radon concentration in pores from recoil. A_u is the radioactivity of uranium and A_{Rn} is the radioactivity of radon, both are in unit of pCi/L . R_s is the recoil length of radon in solid.

Heckter (1934) reported that ^{222}Rn has a R_s of $3.6 \times 10^{-8} \text{ m}$. e is the efficiency of recoil transfer and s is specific surface area with unit of m^{-1} .

$$A_{Rn} = A_U \cdot R_s \cdot e \cdot s \quad (5-1)$$

After the radon entering into the pore space from radium decay, it still maintains energy to travel (Sasaki et al. 2004), and the released radon could either be captured again by adjacent grains or stopped by fluid filled in pore space. Therefore, e is expressed by:

$$e = f_e \cdot f_i \quad (5-2)$$

f_e is the emanation coefficient of radon release from rock particles into surrounding pores by recoil. Andrews and Wood (1972) analytically calculate that this coefficient for plane surface is 23.5%. f_i is the fraction of ejected radon stopped in the interstitial fluid (Fleischer 1983):

$$f_i = 2\sigma - \sigma^2 \quad (5-3)$$

where, $\sigma = d/R_f$, d is the fracture width or pore size and R_f is the recoil range of radon in fluid. For water $R_f = 10^{-7} \text{ m}$ and for gas $R_f = 6 \times 10^{-5} \text{ m}$ (Nierenberg 1992).

Eq. 5-1 is used to obtain radon concentration in water or gas filled pores originated from mineral grains.

5.3.2.2 Generation from Pores

In Nelson et al. (2014), the flowback sample was collected one year after the completion of hydraulic fracturing. It was assumed that the radium concentration measured from their sample represented radium concentration in porous media. Consequently, radon was also produced by such radium through recoil in pores. Such

produced radon would either be emitted to adjacent grains or remain in pores. The escaping ratio is the ratio of surface area lying in the grains to the surface of sphere. For example, in Figure 5-5, escaping ratio is the surface of ABC and DEF to surface of sphere with R_f . Thus, the remaining ratio F of the entire pore could be known as unit minus integration of the escaping percentage, assuming radium is uniformly distributed and no radon that enters grains further travels to next pores:

$$F = 1 - \frac{1}{d} \int_0^d \frac{2\pi R_f [(R_f - x) + (R_f - (d - x))]}{4\pi R_f^2} dx, \text{ if } x < R_f \text{ and } d - x < R_f \quad (5-4)$$

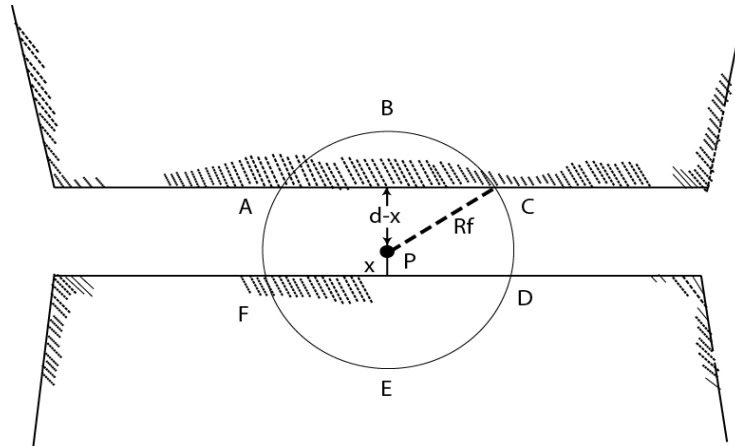


Figure 5-5. Radon escapes from pores into grains. The pore diameter is d and radon recoil length is R_f . When radon particle is ejected into the section of ABC or EFD, it is regarded as being escaped into grains from pore space.

When d is large enough, $(d-x)$ or x may become larger than R_f , Eq. 5-4 should be modified correspondingly. In other words, either term $(R_f - x)$ or $[R_f - (d - x)]$ would be eliminated from Eq. 5-4.

5.3.3 Spherical Pores

Besides slit pore shape, spherical pores also occur in shale, which require different formulas to calculate radon *in-situ* concentration. This section will discuss the proposed equations to calculate radon *in-situ* concentration in spherical pores.

5.3.3.1 Emanation from Grains to Pores

Emanation efficiency, e , is defined in Eq. 5-2. The point O_1 is the center of spherical pore with radius of R as shown in Figure 5-6. Radium atom is initially located at O_2 . The radon recoil range inside fluid filled pore space (inner of solid circle) is R_f and recoil range in solid material is R_s . If the trajectory of radon after recoil is O_2AB , it is helpful to convert the stopping power in fluid to solid (Fleischer 1983). In other words, the distance b in pore filled by fluid is modified to an equivalent distance bR_s/R_f in solid. Radon particle could possibly be ejected and trapped into the pore if the following criteria are satisfied:

$$\frac{bR_s}{R_f} + a > R_s \quad \& \quad a < R_s \quad (5-5)$$

where,

$$a = \frac{2(x+R)\cos\theta - \sqrt{4(x+R)^2 \cos^2 \theta - 4x^2 - 8Rx}}{2} \quad (5-6)$$

$$b = \sqrt{4(x+R)^2 \cos^2 \theta - 4x^2 - 8Rx} \quad (5-7)$$

For a specific x , when the radon trajectory is within the range of angles $[\theta_1, \theta_2]$ it will stay in the pore space. The corresponding probability is obtained by:

$$e_x = \frac{2\pi R_s[(R_s - R_s \cos\theta_2) - (R_s - R_s \cos\theta_1)]}{4\pi R_s^2} = \frac{\cos\theta_1 - \cos\theta_2}{2} \quad (5-8)$$

The overall emanation efficiency e is:

$$e = \frac{1}{V} \int e_x dV = \frac{1}{\left(\frac{4}{3}\pi(R+R_s)^3 - \frac{4}{3}\pi R^3\right)} \int_0^{R_s} e_x 4\pi(R+x)^2 dx \quad (5-9)$$

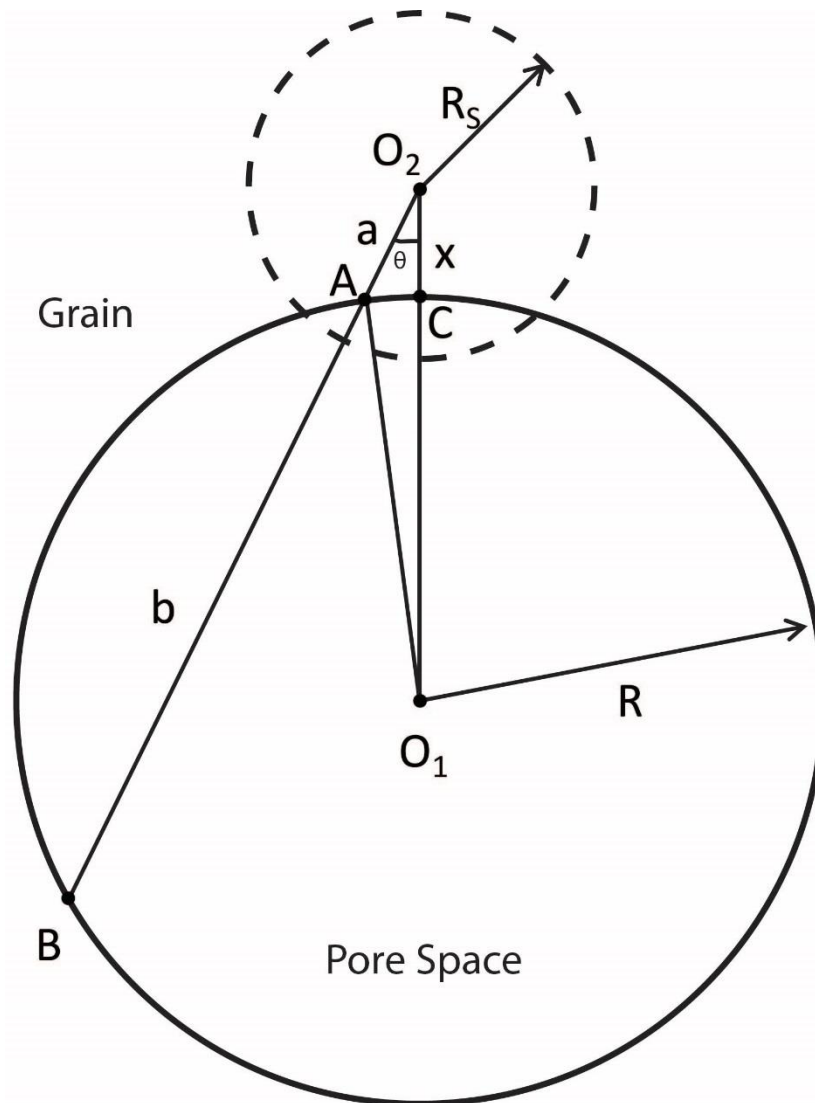


Figure 5-6. Schematic cross-section view of spherical pore shape. The radon generated from radium in grains may enter the pore space. O_2A section has length of a . AB section has length of b . O_2C section has length of x .

5.3.3.2 Generation from Pores

Figure 5-7 shows the geometry considered in the calculation of the remaining radon in pore after alpha decay of radium in the pore space. The radium atom is located at position O_2 . If produced radon falls on to the curve \widehat{AB} outside the pore space (solid circle), it is regarded as entering into adjacent grains. The remaining ratio F is defined to represent how much of the produced radon will be kept in the pore space. By assuming radium is uniformly distributed in the pore space, F (Flügge and Zimens

1939) is calculated by:

$$F = 1 - \frac{3}{4}\alpha(1 - \alpha^2/12) \quad (5-10)$$

where,

$$\alpha = R_f/R \quad (5-11)$$

The remaining ratio F becomes zero when $R_f \geq 2R$.

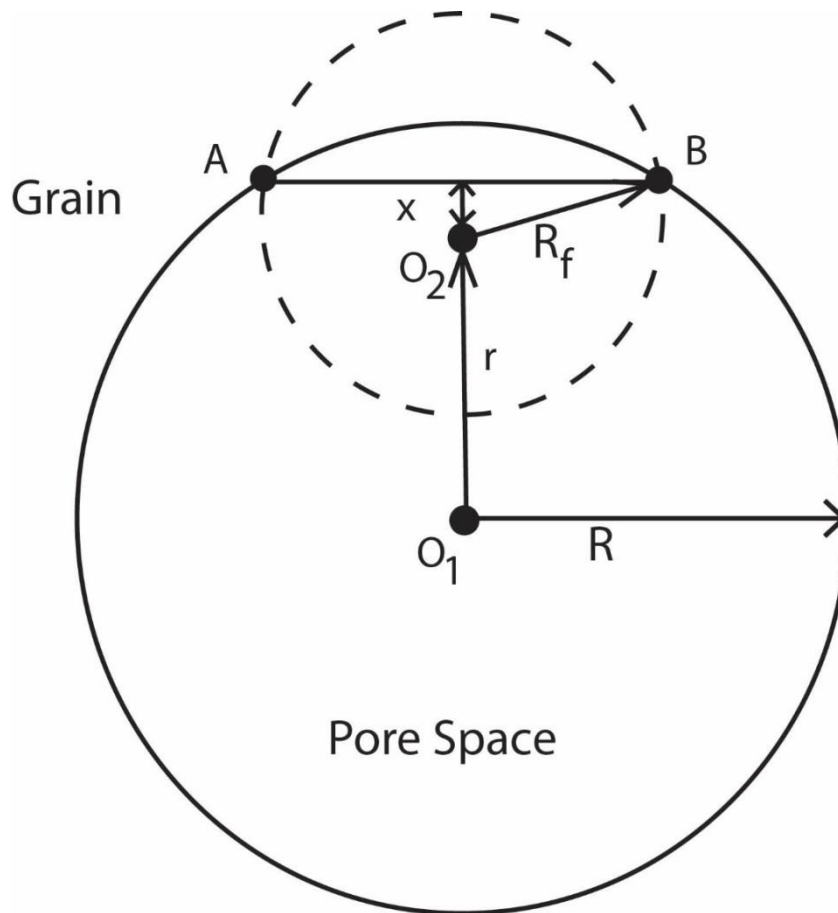


Figure 5-7. Schematic cross-section view. Radon generated from radium in pore space may remain in pore space.

5.4 Radon Transport

Radon starts to flow with natural gas or water when the reservoir is developed. Radon partitions between water and gas if there is any two-phase condition. The partition coefficient of radon is changing with temperature T (Weigel 1978):

$$K = \frac{{}^{222}\text{Rn}_w}{{}^{222}\text{Rn}_g} = 0.105 + 0.405 \times e^{-0.5027T} \quad (5-12)$$

Where, ${}^{222}\text{Rn}_w$ represents radon concentration in water and ${}^{222}\text{Rn}_g$ is the concentration in gas. Radon will flow into hydraulic fractures through porous media and then flow to wellbore. The flow of radon in porous media is assumed to be governed by Darcy's law, and the radon concentration at the wellhead is assumed to be the same at the bottom hole of the well since the gas transport in pipe is rapid. In other words, the radon decay inside well tubing is not simulated. Later on, radon entrained in gas will be produced to the surface and enter residential buildings through pipelines. Radon surface transport is not included in this study either. The entire radon transport process is illustrated in Figure 5-8.

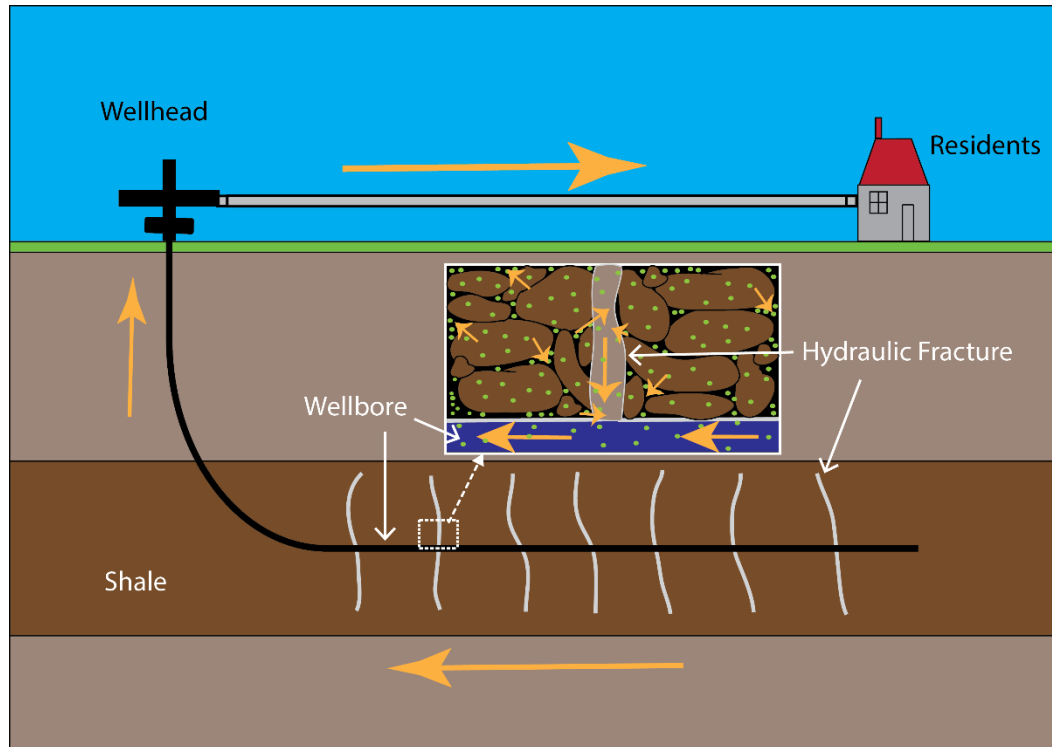


Figure 5-8. Radon transport process from porous media to residential users. Green dots represent radon particles.

5.5 Model Description

A compositional model is constructed to capture radon generation, release and transport process. Major assumptions are:

- Slit shaped pore.
- The flow in porous media is governed by Darcy's law.
- Two phases: liquid and vapor. The liquid phase is water, and the vapor phase is methane.
- Homogeneous distributed radioactive atoms in the reservoir. Uranium and radium are uniformly distributed in grains. Radium is also uniformly distributed in liquid phase. Radon has homogeneous concentration throughout the formation.

- Radon is in secular equilibrium with radium. Radon half-life is much shorter than radium half-life. As a consequence, it will achieve secular equilibrium.

Above discussion about radon emanation mechanism gives the estimation of radon in-situ concentration. In order to maintain secular equilibrium, a solid source of radium is designed in the model to simulate the radon generation from grains that contains radium before shale development. Proppant is the man-made solid material used to keep induced hydraulic fracture open. Thus, there is no natural solid radium attached on proppant and, for hydraulic fracture grids, the solid radium concentration is therefore slightly lower than matrix. The decay rates of both radon and radium are dependent on their own concentrations. Radioactive decay is simulated as a first order chemical reaction by assigning corresponding decay constant as the reaction frequency factor (CMG-STARS user's guide, 2012). The reaction frequency factor is also known as the reaction rate constant. Hydraulic fracture is implemented with conductivity of 200 *md·ft*. This work only simulates one fracture and a quadrant of the stimulated reservoir as shown in Figure 5-9(a). The horizontal well only perforates at the left upper corner grid. Local grid refinement is applied nearby the fracture in order to accurately simulate pressure and fluid transport between fracture and matrix (Cippola et al. 2010).

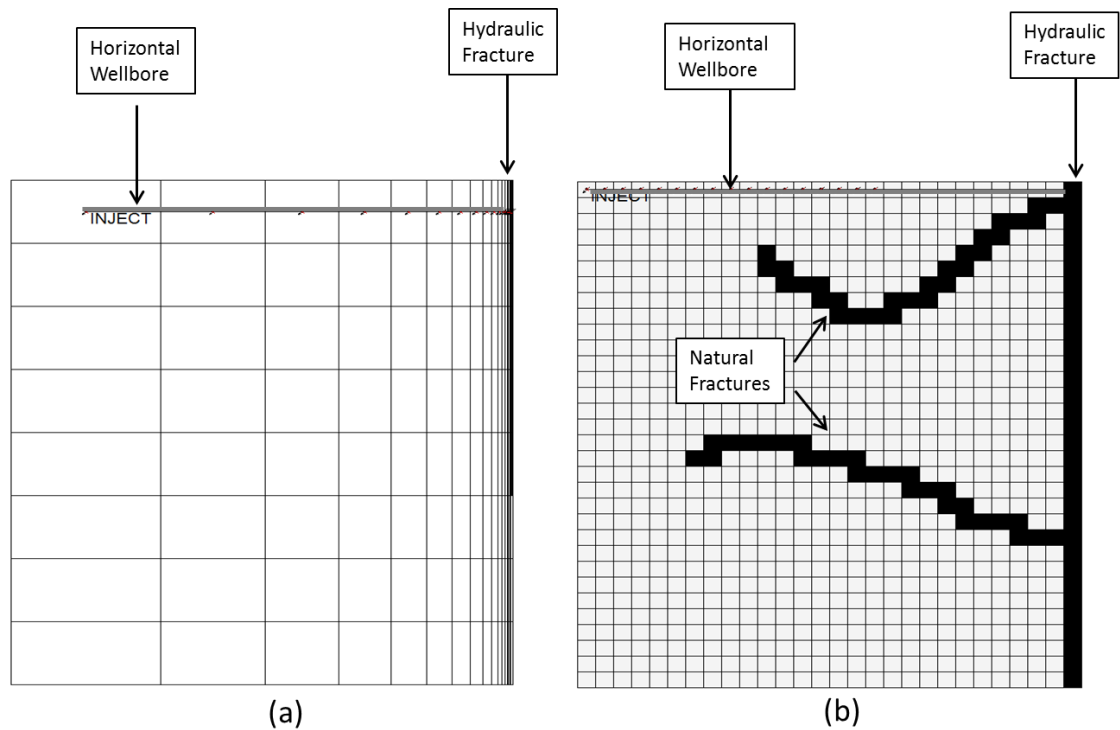


Figure 5-9. Model configuration. (a) is for the base case. (b) is the case with manually created natural fractures. The black color represents hydraulic fracture and natural fractures. The gray color represents the wellbore.

To better visually understand how natural fractures influence radon wellhead concentration, natural fractures are manually created, intersecting the hydraulic fracture as shown in Figure 5-9(b). Anisotropic permeability of natural fracture is determined through Sakhaee-Pour and Wheeler (2015). In their work, three different types of interactions are considered: matrix-matrix, matrix-fracture and fracture-fracture. This algorithm enables us to use uniform grid system to investigate the natural fracture's impact on fluid flow in such a system.

In the base case, water based fracking fluid is injected create hydraulic fractures for 0.5 *day* followed by a shut-in period for 0.5 *day*. The injected fracking fluid does not contain any radon or radium. The well will start to produce back at a constant bottom-

hole pressure (BHP) after shut in. Essential input parameters for shale reservoirs and wells are listed in **Table 5-2**.

Table 5-2. Simulation input parameters of base case		
Parameter	Value	Source
Uranium Concentration, <i>pCi/L</i>	1.7×10^4	(Resnikoff 2011)
Radium Concentration in Water, <i>pCi/L</i>	1.73×10^4	(Nelson et al. 2014)
Radon Concentration, <i>pCi/L</i>	1.22×10^4	From Calculation
Pore Diameter, <i>nm</i>	20	(Mosher et al. 2013)
Natural Fracture Width, <i>nm</i>	50	(Gale et al. 2014)
Hydraulic Fracture Conductivity, <i>md • ft</i>	200	(Medeiros et al. 2008)
Matrix Permeability, <i>md</i>	5×10^{-4}	(DOE, US 2009)
Temperature, <i>K</i>	377	(DOE, US 2009)
Initial/Residual Water Saturation, %	25	(DOE, US 2009)
Porosity, %	5	(DOE, US 2009)
Reservoir Pressure, <i>psi</i>	3925	(Medeiros et al. 2008)
BHP, <i>psi</i>	2000	(Cipolla et al. 2010)
Radon Diffusivity in Water, <i>m²/s</i>	1.13×10^{-9}	(Tanner 1980)
Radon Diffusivity in Gas, <i>m²/s</i>	10^{-5}	(Tanner 1980)

5.6 Result and Discussion

5.6.1 *In-situ* Radon Concentration

To investigate the impacts of pore size distribution and pore shape on *in-situ* radon concentration, 3000 pores were generated following the pore size distribution for each case in Figure 5-4. For simplification, radon recoil range in pore space is assumed as 100nm. The radium concentration in a shale grain is taken to be 3.4×10^4 pCi/L (Resnikoff 2011). The radium concentration in formation water is determined by the lab measurement of 1.7×10^4 pCi/L (Nelson et al. 2014).

Figure 5-10 shows the distribution of radon *in-situ* concentration for all the three cases. The radon is generated from radium in rock grains as well as radium in formation water. As Case A and Case C were assumed slit pore shape, the formulas in section 5.3.2 were employed to calculate radon *in-situ* concentration. In Case B, the equations derived in section 5.3.3 for spherical pore shape were utilized.

Figure 5-10 shows that both pore shape and pore size distribution influence the radon concentration in pore space. The distribution of radon *in-situ* concentration in Case A is more stretched than Case C, which is caused by the difference in pore size distribution as shown in Figure 5-4. Nevertheless, radon *in-situ* concentrations in these two cases are mostly concentrated at the level of 1.17×10^4 pCi/L. Such similarity is attributed to the majority of their pore sizes are both in the range of 1-10nm. If the general pore size in Case C is 10 times larger than Case A, a quite different distribution of radon *in-situ* concentration should be expected. On the other hand, pore shape is another critical factor. The radon *in-situ* concentration obtained from spherical model is generally shifted to the right of the slit model. The mode value of radon concentration

for Case B is 1.22×10^4 pCi/L, larger than the mode value of Case A. This observation indicates that pore shape will influence the pore size distribution and it will further affect the radon *in-situ* concentration. Therefore, an accurate description of the pore size distribution as well as pore shape is essential to evaluate the radon *in-situ* concentration.

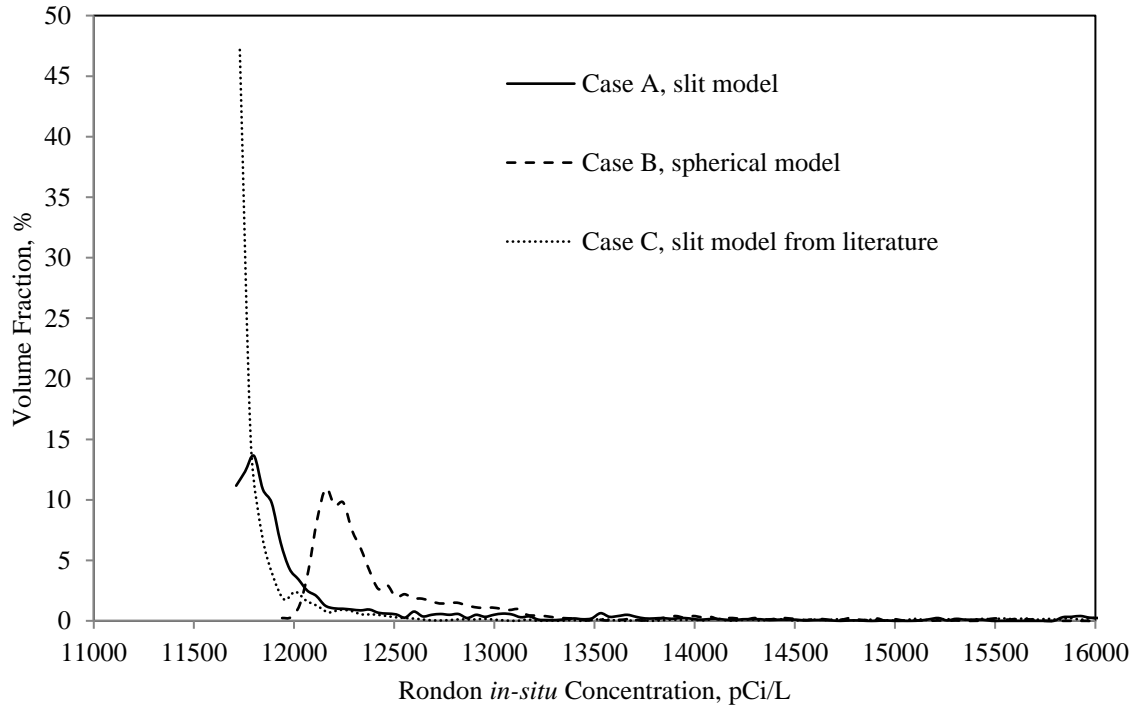


Figure 5-10. Radon total *in-situ* concentration for the three cases.

5.6.2 Wellhead Radon Concentration

The simulation assumed the initial water saturation was 25%. As previously assumed blocked configuration of saturation in section 5.2.1, water saturated the small pores first. Larger pores were filled with gas. The average pore size was used to represent water filled pores and gas filled pores for simplification. Average pore size for each case and their corresponding radon *in-situ* concentration in pores are shown in

Table 5-3. As pore size in Case A and Case C is concentrated at the magnitude of 1-10nm, their calculated average pore size of water filled pores is close to each other.

Table 5-3. Radon in-situ concentration				
	Water Filled Pores		Gas Filled Pores	
	Avg. Size,	Radon <i>in-situ</i> Conc.	Avg. Size,	Radon <i>in-situ</i> Conc.
	<i>nm</i>	<i>pCi/L</i>	<i>nm</i>	<i>pCi/L</i>
Case A	4.0	1.175×10 ⁴	26	23
Case B	5.5	1.220×10 ⁴	40	85
Case C	3.2	1.171×10 ⁴	198	48

Radon diffusivity in water is $1.13 \times 10^{-9} \text{ m}^2/\text{s}$ and $10^{-5} \text{ m}^2/\text{s}$ (Tanner 1978) in air. Although radon concentration in water pores and gas pores right after the generation from radium are dramatically different as seen in Table 5-3, the diffusion process could balance radon concentration in these two types of pore, especially over the long geological time. Consequently, after being buried underground for millions of years, it is safe to assume that the radon atoms are uniformly distributed. Gas pores shall eventually have the identical radon concentration with water pores. Therefore, for each case, the radon *in-situ* concentration in water pores was used as the initial radon concentration in simulation. Radium content in rock grains was designed correspondingly.

Figure 5-11 shows the wellhead radon concentration for the three cases. Wellhead radon concentration in Case A gradually increases from 36 *pCi/L* to 100 *pCi/L* in 100 *days*. Subsequently, it remains at 100 *pCi/L* for late production time. The

injected fracking fluid pushes the radon and radium away from the wellbore. After a certain period, highly concentrated radon gas will flow back to wellbore. As a result, the wellhead radon concentration at early time is relatively low. The other two cases behave a similar pattern in radon production history with Case A. Case C has an identical radon production history with Case A because of their similar initial radon *in-situ* concentration in Table 5-3. Since Case B has a higher initial radon concentration, it produces higher wellhead radon concentration as well. This observation indicates that the wellhead radon concentration is directly related with the *in-situ* concentration. Furthermore, pore size distribution and pore shape will influence the radon *in-situ* concentration, which will further determine the wellhead radon concentration.

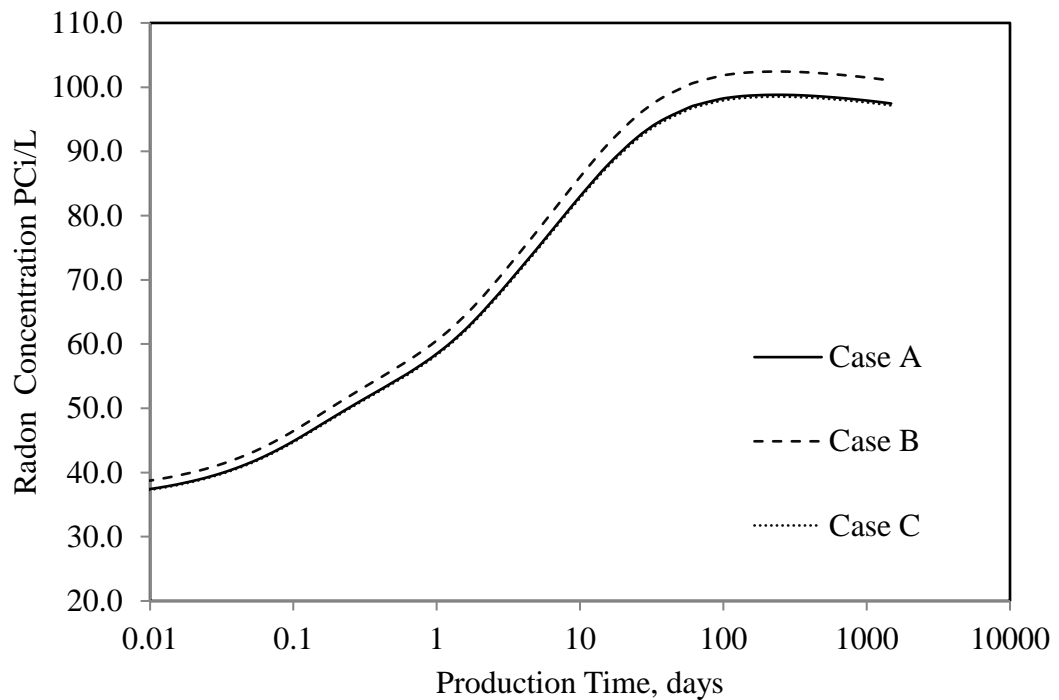


Figure 5-11. Wellhead radon concentration with multiple initial radon *in-situ* concentrations. Wellhead radon concentration is directly related with the *in-situ* concentration

5.6.3 Impact of Spatial Distribution of Pore Size

Shale formations are highly heterogeneous. The pore shape and pore size could vary dramatically from location to location within a same formation, leading to heterogeneous radon *in-situ* concentration. This section studies the impact of heterogeneity. The stimulated reservoir was divided into two sections: near fracture zone and far formation zone (Figure 5-12). By doing this, people can understand how heterogeneously distributed radon could affect wellhead radon concentration.

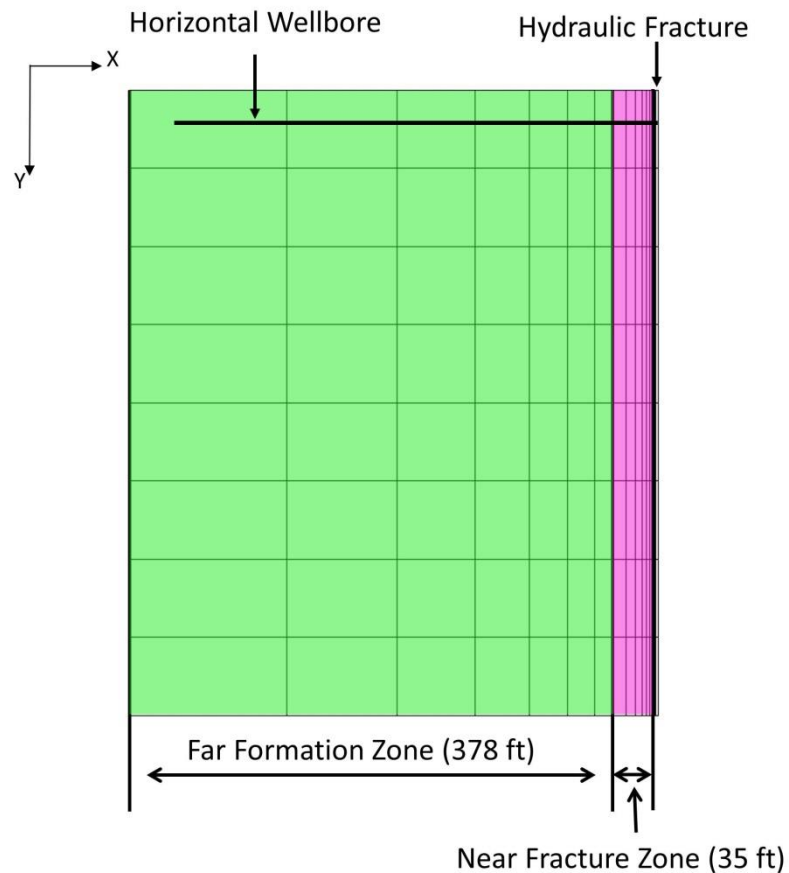


Figure 5-12. Synthetic model configuration. The horizontal well is located at the top. It is perforated at hydraulic fracture at the left side. The stimulate reservoir is divided into two sections: near fracture zone and far formation zone.

The Case A and Case B in Figure 5-11 were used as the lower and upper bounds.

Another two scenarios were designed, whose initial radon *in-situ* concentrations are listed in Table 5-4. Their results are plotted in Figure 5-13.

Simulation results show wellhead radon concentrations in both cases are constrained by the upper and lower bounds. This can be explained by material balance. Since the overall radon mass will not be higher than Case B or lower than Case A, the produced radon mass will not exceed the limit as well. Another trend observed from Figure 5-13 is that the near fracture zone determines the early radon production. If the near fracture zone has a higher radon *in-situ* concentration, the produced wellhead radon concentration will be higher. On the other hand, the far formation zone influences the late time radon production. A high radon *in-situ* concentration in far formation zone will lead to a rapid increase of wellhead radon concentration from early to late time.

Table 5-4. Radon in-situ concentration in near fracture zone and far formation zone for Case D and Case E.		
	Case D	Case E
Radon in Near Fracture Zone, <i>pCi/L</i>	1.220×10 ⁵	1.175×10 ⁴
Radon in Far Formation Zone, <i>pCi/L</i>	1.175×10 ⁴	1.220×10 ⁵

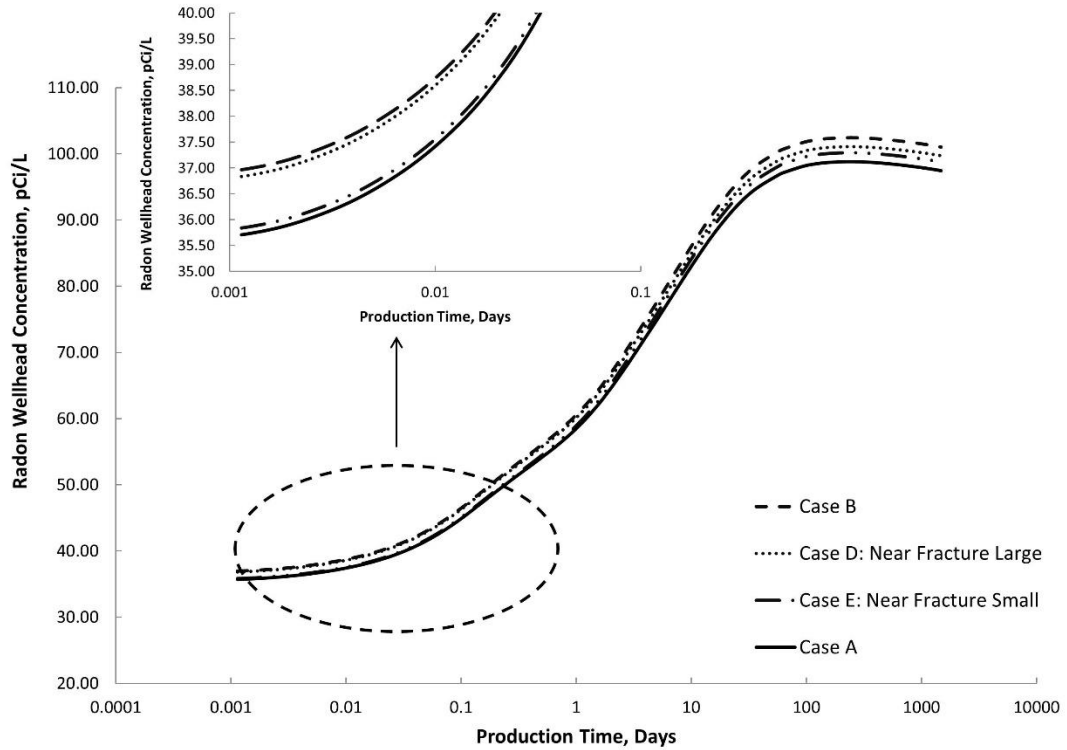


Figure 5-13. Wellhead radon concentration to investigate heterogeneity impact. Near fracture zone determines the early radon production.

5.6.4 Impact of Natural Fracture

The solid line in Figure 5-14 shows that, at the early stage, radon concentration at wellhead is relatively low because gas with radon was pushed away from the well during fracturing process. Radon wellhead concentration increases and reaches a peak, which is around 105 pCi/L , for the particular case study. Such increase is because the radium and radon gas are flowing back. Later on, radon concentration slowly declines to 95 pCi/L after 7.5 years production, due to the loss of radium in formation. This wellhead concentration is directly related to radon in-situ concentration, which depends on pore size and emanation efficiency.

Radon wellhead concentration of the case with natural fractures can be found as the dashed line in Figure 5-14. Initially, radon wellhead concentration in naturally fractured reservoir is slightly higher than the value in case without natural fractures because natural fractures will bring high concentrated radon gas to wellhead faster. After days of production, matrix is contributing to the production and radon concentration in non-naturally fractured well becomes higher.

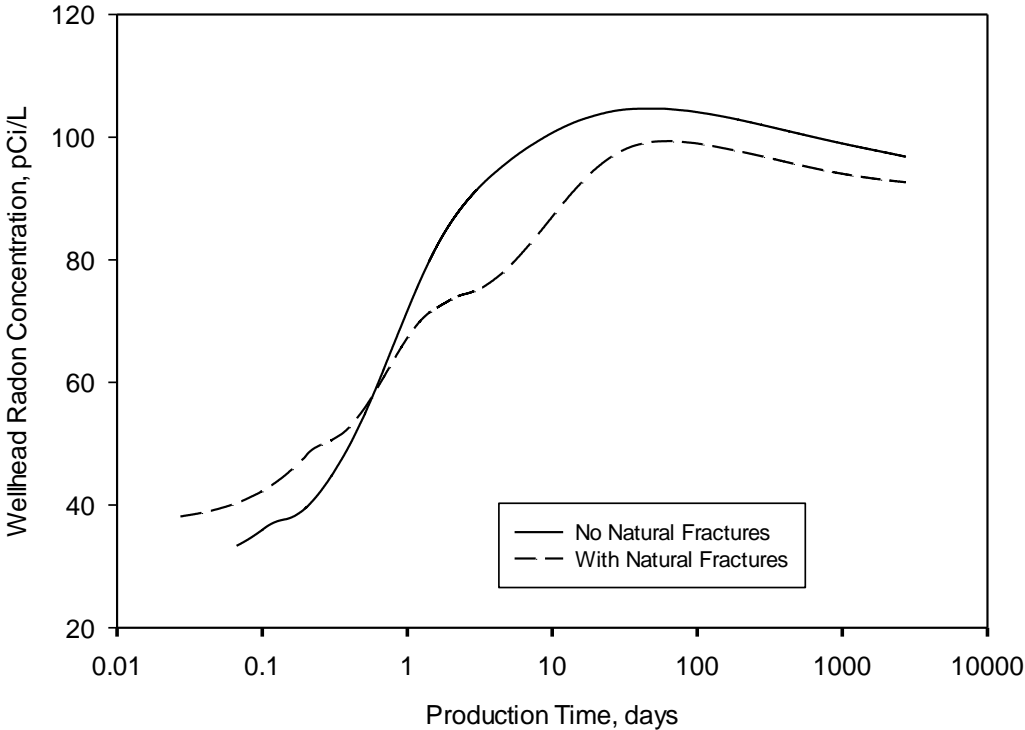


Figure 5-14. Radon wellhead concentration from simulation output

5.6.5 Sensitivity Analysis

Shale gas development requires delicate completion and stimulation design to obtain high production rate. However, radon release has not been carefully considered. Therefore, several parameters that could possibly affect radon concentration are

investigated in this sensitivity analysis. Relative permeability data for shale matrix is obtained from Cheng (2012). According to its base water relative permeability, another two curves were created to represent water preferred and non-preferred hydraulic fracture (Figure 5-15). A summary of all varied parameters is given in Table 5-5. In this part, the base case has no natural fractures.

Table 5-5. Varied parameters for sensitivity analysis			
Parameter	Low Value	Base Case	High Value
Hydraulic Fracture Half-Length, ft	240	300	360
Hydraulic Fracture Permeability, md	500	1000	1500
Matrix, md	0.00005	0.0005	0.005
BHP, psi	1500	2000	2500
Radon Diffusivity in Gas, $\times 10^{-5}$ m²/s	0.75	1	1.25
Water Relative Permeability in Fracture	Low	Base	High
Radium Concentration in Water, $\times 10^4$ pCi/L	0.8	1.1	1.4
Shut in Time, day	0.3	0.5	0.7

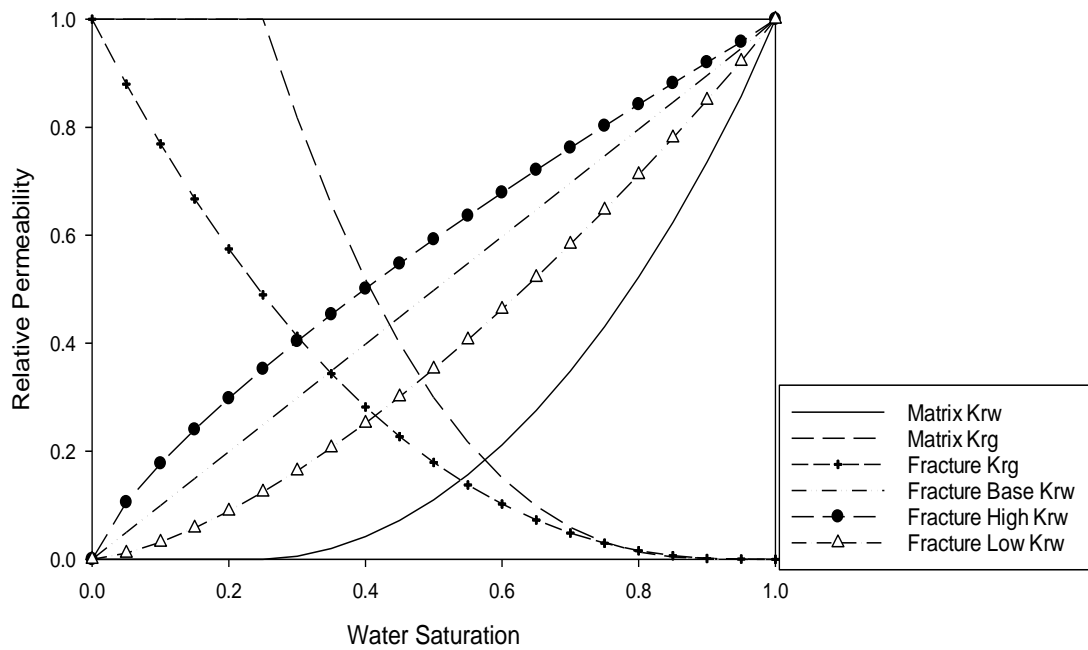


Figure 5-15. Relative permeability curves. Modified from Cheng (2012).

Two tornado charts are generated regarding to radon wellhead concentration after 5 days production and 7.5 years production, shown in Figure 5-16 and Figure 5-17 respectively. It is noticed that impacts of some parameters change significantly at different times.

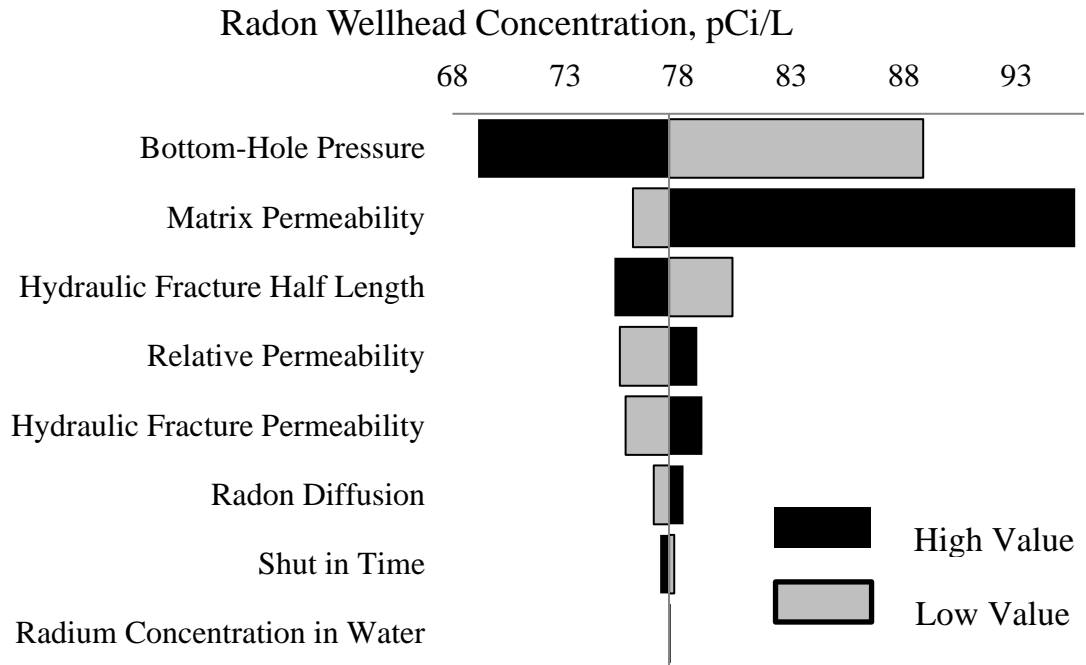


Figure 5-16. Sensitive tornado charts after 5 days of production. Black color represents the high value and gray color stands for the low value.

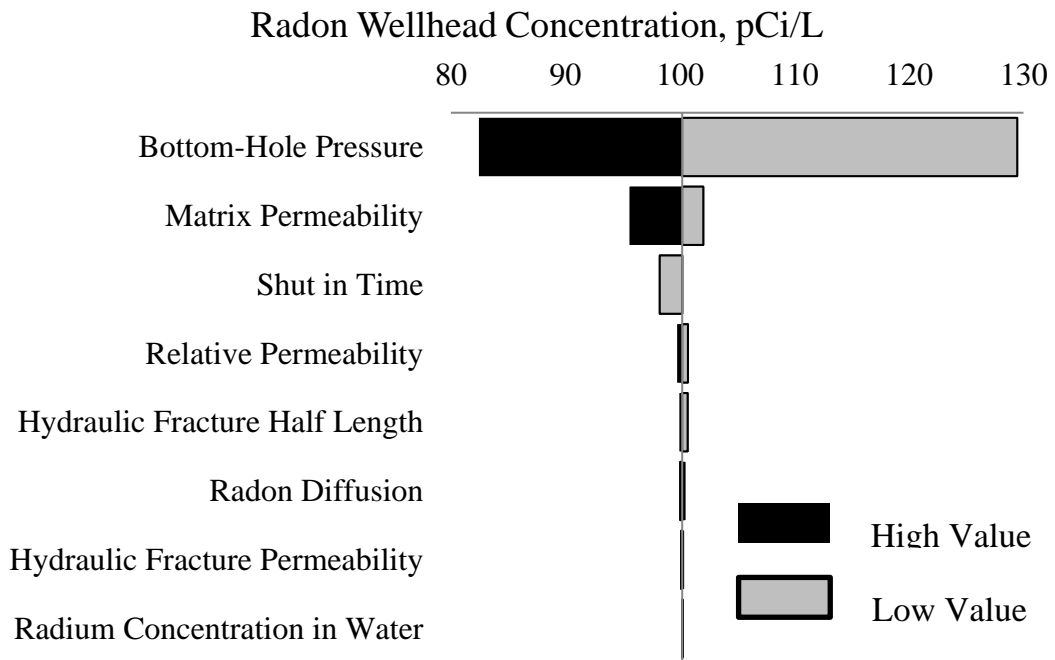


Figure 5-17. Sensitive tornado charts after 7.5 years of production. Black color represents the high value and gray color stands for the low value.

- BHP is the most influential factor that determines radon wellhead concentration at both moments, especially in later time. At high BHP, gas rate is small. It results in low radon wellhead concentration since radon has more time to decay inside hydraulic fracture where secular equilibrium is broken. On the other hand, with lower BHP, wellhead would observe higher radon concentration.
- Matrix permeability is the second influential factor. At the beginning of production, high matrix permeability brings more radon and radium to the wellbore and causes higher radon wellhead concentration. For the case with high matrix, in the later time, less radon and radium remains in the formation since majority of them are produced rapidly at the early time. This results in a lower radon wellhead concentration.
- Hydraulic fracture permeability also controls production rate as well as the radon wellhead concentration, in the same way with BHP. Thus, higher permeability causes higher radon concentration and vice versa.
- Hydraulic fracture half-length represents the high conductive conduit volume within the reservoir. A longer half-length means a larger hydraulic fracture and more fracking fluid could be injected into the reservoir. Therefore, radium in water is diluted more significantly. In addition, more radon will partition into the liquid phase from vapor phase. It turns out the radon concentration in gas at wellhead is lower.
- Relative permeability has opposite impacts in early time and later time. At the early stage, water preferred hydraulic fracture causes reservoir water with radium flows back to the wellbore faster. Consequently, high radon

concentration occurs initially. However, the smaller water relative permeability case has higher concentrated radon gas being produced at the later time since more radium is left in the reservoir.

- Radium concentration in reservoir initial water has minor impacts. Because radium in water only contribute a little portion of radon generation, compared with radon ejected from grains. However, if the pore size increases and radium in water plays a more important role in radon generation, the influences of this factor in a long time will increase.
- Longer shut in time leads lower radon wellhead concentration especially at early time. Overall radon in-situ concentration decreases during the shut in period since its secular equilibrium is broken by the injected fracking fluid. Therefore, with longer shut in time, more radon will decay, resulting in less wellhead radon concentration.
- Radon diffusion is the reason that causes the slow decline of radon wellhead concentration as shown in Figure 5-18. With diffusion, radon wellhead concentration maintains at a stable level for a very long time. Its impact on early production stage is not that much significant.

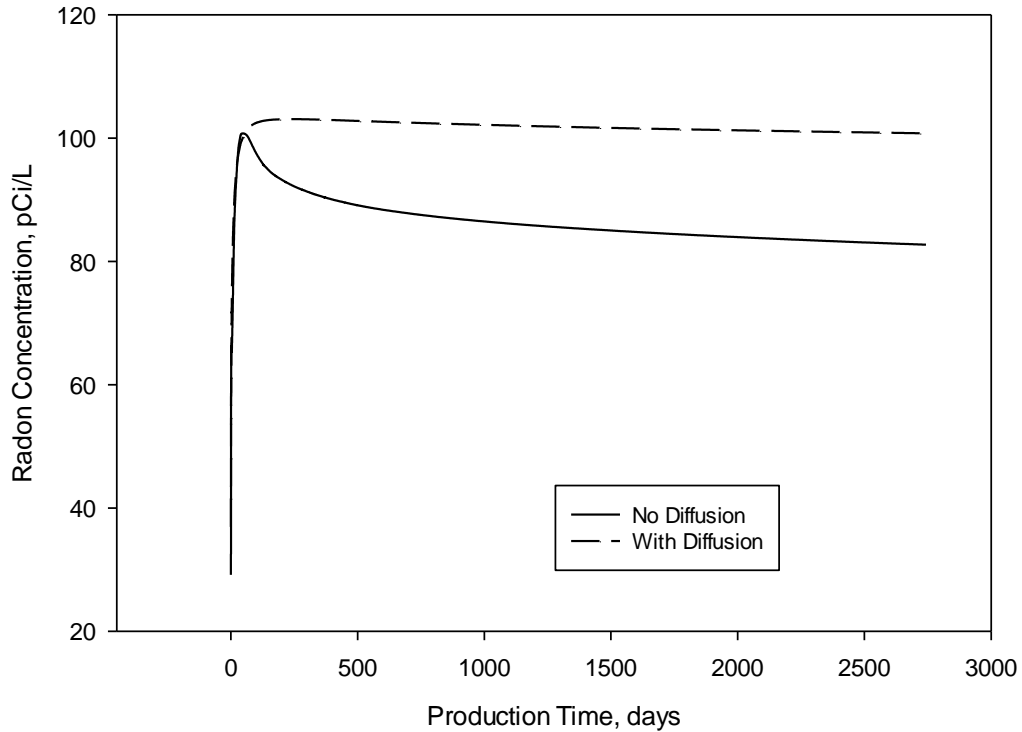


Figure 5-18. Diffusion impact on radon wellhead concentration

5.6.6 Discussion

5.6.6.1 Transport Time in Wellbore

Figure 5-19 shows the simulation outputs of gas production rate for the cases of with and without natural fracture. The rate rapidly declines from a high initial rate to a low rate as expected, ranging from 10^5 to 10^3 *ft/day* (Figure 5-19). Considering such production rate is obtained from a quadrant of the stimulated reservoir, the actual gas rate could be four times larger. Given the well radius is 3 *in.* and the formation depth is 6500 *ft.*, the transport time from bottom hole to wellhead is around 0.003 to 0.3 *day*, which is at least one order smaller than the radon half-life. Therefore, it is reasonable to assume that radon decay inside wellbore is negligible. Of course, these numbers may

vary case by case and radon decay inside wellbore should be considered if possible for a more comprehensive analysis.

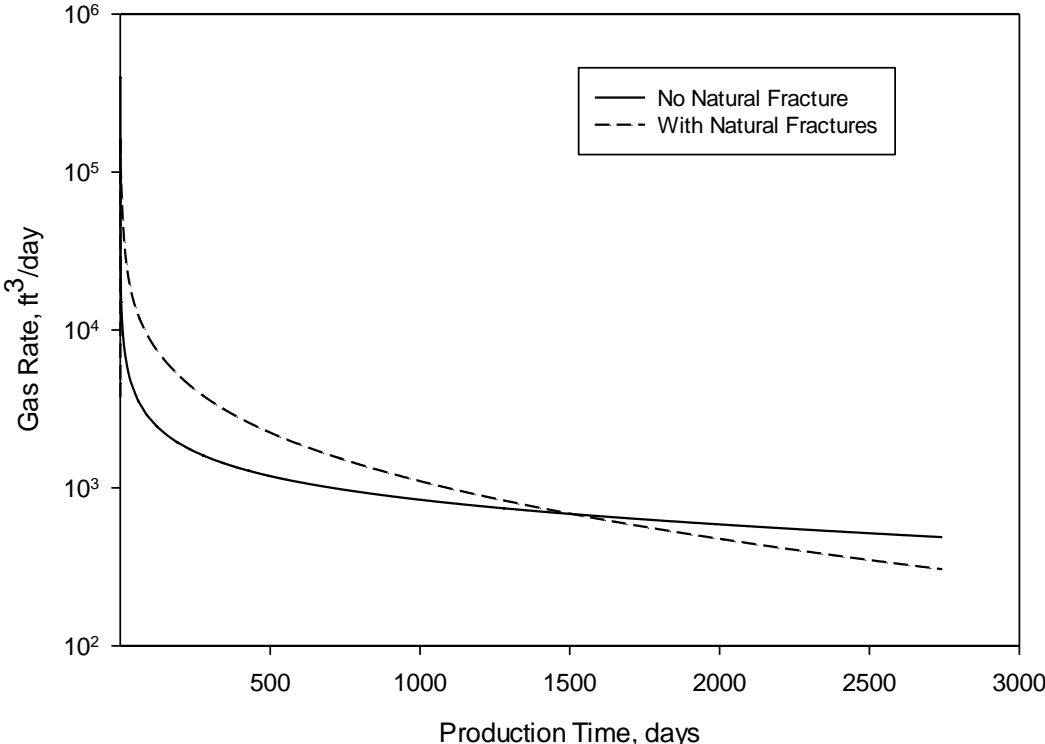


Figure 5-19. Gas production rate of two cases

5.6.6.2 Radon Production

Section 5.3 present formulas to capture the radon generation process in slit and spherical pores, considering the fluid stopping power and radium existence in pore space. The primary result indicates that the pore shape as well as pore size distribution strongly influence the *in-situ* radon concentration, which in turn will directly affect the wellhead radon concentration. The simulation utilized representative data of Marcellus shale and revealed that wellhead radon concentration increases from 36 *pCi/L* to 110 *pCi/L*. This result is in agreement with the field measurement (USGS 2012) that pointed

out the on-site radon concentration in Marcellus shale ranged from 1 pCi/L to 79 pCi/L , with a median value of 37 pCi/L . In addition, the radon *in-situ* concentration near the hydraulic fracture influences radon production in early time, while the impact of radon that is far away from fracture affects at late time. More importantly, simulation results indicate that radon production is truly above the safe standard and it is indeed a potential hazard to the public health and environment.

Transport time in surface facility from wellhead to consumers could reduce the radon levels, but radon may still be dangerous to human health. For example, assuming it takes natural gas one week to be transported from wellhead to users, radon will decay to approximately 25% of its original concentration considering 3.8 *days* half-life. That is to say, the radon concentration that entered residential buildings would be in the range of 9 to 25 pCi/L (based on Case A), which is far above the safe standard of 4 pCi/L . Therefore, radon monitoring and protection should be implemented during Marcellus shale gas development.

There are three apparent trends from the sensitivity analysis. First, radon concentration is strongly related with gas production rate. If the gas flows fast, radon shall have less time to decay and its wellhead concentration is higher. On the other hand, if the gas flow is slow, radon will decay more before it approaches the surface, so that the wellhead concentration would be lower. Second, water injected for fracturing will dilute radon concentration in gas as well as radium in water and it turns out to decrease the radon wellhead concentration. This observation implies that a long hydraulic fracture, which is beneficial to production, reduces the radon release. Third,

radon wellhead concentration is sensitive to radium content in reservoir. With less radium in water, the radon wellhead concentration would be lower.

According to the above study, radon hazard, especially at the early stage, could be remedied more or less by controlling production rate. Therefore, it may change the current shale gas development protocols for the benefit of environments and public health. Reducing radium concentration near the wellbore could be another way to resolve the problem. Yet, how to successfully implement the treatment needs further investigations.

The uranium and radium concentration and their distributions in the reservoir will intensively affect the radon wellhead concentration. The pore size distribution is also an important influential factor. More thoroughly measured data will help increase the accuracy of the predicted radon wellhead concentration. Another approximation is the slit pore shape. A cylindrical structure will result in a different radon in-situ concentration and the analysis should be straightforward.

5.6.6.3 Comparison of Radon Concentration between Sandstone and Shale:

Generally, uranium concentration is less in sandstone than shale. Since uranium is the source of radon, lower radon concentration from sandstone is expected. However, this is not always true. Rowan and Kraemer (2012) reported radon activity in sandstone gas from Pennsylvania was 7-65 pCi/L, which is in the same order with the radon concentration in shale gas from the same location. There are several hypotheses to explain the quantity. First, these two formations contain similar level of uranium since

they are close in location. Second, radon may find a way to migrate from shale to sandstone. Nevertheless, these explanations have not been rigorously investigated.

Literature survey indicates that there is very limited reported measurement of radon concentration in sandstone gas production. The measurement mentioned above indicates that the radon from sandstone could be a concern. On the other hand, it is also necessary keep in mind that the radon release should be analyzed case by case. Radon production is related with pore size, reservoir characteristics, uranium and radium concentrations, etc. It is not reasonable to conclude that shale gas must have the radon issue or sandstone gas does not. Thorough research and investigation of the target formation are required before making the conclusion.

Nomenclature

Normal

<i>A</i>	=radioactivity, $T^{-1}L^{-3}$
<i>a</i>	=one parameter, <i>L</i>
<i>b</i>	=one parameter, <i>L</i>
<i>d</i>	=width, <i>L</i>
<i>e</i>	=emanation efficiency, fraction
<i>F</i>	=remaining fraction, dimensionless
<i>f</i>	=fraction
<i>K</i>	=partition coefficient, fraction
<i>R</i>	=recoil length, <i>L</i>
<i>s</i>	=specific surface area, L^{-1} (surface area/ volume of pore space)
<i>T</i>	=Temperature, <i>K</i>

x =one length parameter, L
 α =one parameter, dimensionless
 θ =angle, degree
 σ = d/R_f , fraction

Subscript

e =release fraction from grain into pore
 f =fluid
 g =gas
 i =fraction that being stopped in pore, fraction
 Ra =radium
 Rn =radon
 s =solid
 w =water

Chapter 6. Conclusions and Recommendations

6.1 Conclusions

This dissertation quantifies the particle movement and its conclusions from previous individual chapter are as follows:

1. This dissertation first develops of an innovative procedure of SWCTT for the condition of two mobile phases. The new SWCTT has been provides a reasonably precise measurement of mobile saturations, validated through numerical simulation. The new modified MoM is also applicable in conventional SWCTT to measure immobile oil saturation and it improves the accuracy of conventional MoM. The new tracer method is an easy and robust in-situ way to measure oil and water saturations near the wellbore at any time of production, without the limitation of conventional SWCTT analysis. The new modified SWCTT can better assist engineers to monitor the reservoirs and determine the best time to start EOR operations.
2. An approach is introduced to estimate fracture volume by injecting a slug of aqueous solution containing a partitioning tracer into a shale gas reservoir. MoM is capable to determine the swept volume of partitioning tracer under two-mobile-phase condition. The tracer production data is indicative of the total volume of fracture and infiltration zone. Two linear relationships of tracer tail are observed when fracture exists. Extrapolating the first straight section using exponential decline can estimate fracture volume. Its accuracy is influenced by permeability ratio. The partitioning tracer is recommended to inject as a slug at the beginning of stimulation treatment at each stage, so that it can inform the

entire fracture volume. Partitioning tracer has rapid feedback even though the injected fracking fluid is trapped in the system. The tracer test is therefore time-efficient. Tracer should be carefully selected based on its partition coefficient and adsorption should be avoided when selecting the tracer for fracture volume diagnosis.

3. A RWPT algorithm to track the partitioning tracer movement in multi-mobile phase condition is developed. It reduces the numerical dispersion caused by the finite-difference based method. By comparing the developed program with CMG, the advantage of RWPT is proven.
4. This dissertation quantitatively evaluates radon concentration at wellhead through synthetic simulation by coupling radon generation, recoil, decay and transport in the subsurface. Radon emanation efficiency and radon in-situ concentration are affected by pore size as well as pore geometry. Radon is produced along with shale gas and its wellhead concentration exceeds the safe level. Therefore, for the public wellness, appropriate regulation should be carried out dealing with radon production. The sensitivity analysis shows that radon wellhead concentration is strongly related with production rate. Producing shale gas at a low rate reduces the radon hazard. This can be achieved through operations such as increasing the BHP. Increasing the shut-in time and fracture half-length also help lower the radon wellhead concentration. Longer fracture half-length will also contribute to the shale gas production, which is not controversial to the economic interest.

6.2 Recommendations for Future Work

The following recommendations may be considered for future research focus.

1. Other contextual factors such as drift and mixture injection could be investigated to determine their impacts on determining mobile oil saturation through SWCTT. Such study will provide additional practical guidance to field operations.
2. This dissertation uses partitioning tracer to estimate single fracture. It is of industry interest to investigate application of partitioning chemical tracer in multi-fracture system. Fluid flow from multi-fracture will change the interpretation of tracer production data. Therefore, future work could focus on this topic.
3. RWPT is proven as a powerful tool to inversely simulate tracer flow. Next step is to implement this algorithm into reservoir simulators to interpret tracer test data.
4. The future work of radon hazard is to come up a control or mitigation method to reduce the radon pollution since it is proven to be real. Also, it is necessary to integrate radon wellhead concentration with surface transport to better understand its threat.

References

- Abbaszadeh-Dehghani, M., and Brigham, W. E. 1984. Analysis of well-to-well tracer flow to determine reservoir layering. *Journal of petroleum technology*, 36(10): 1-753. <http://dx.doi.org/10.2118/10760-PA>
- Adesida, A.; Akkutlu, I.; Resasco, D.; Rai, C. 2011. Kerogen pore size distribution of Barnett shale using DFT analysis and Monte Carlo simulations. *Society of Petroleum Engineers*. DOI: 10.2118/147397-MS.
- Allison, S. B., Pope, G. A., and Sepehrnoori, K. 1991. Analysis of field tracers for reservoir description. *Journal of Petroleum Science and Engineering*, 5(2): 173-186. [http://dx.doi.org/10.1016/0920-4105\(91\)90066-V](http://dx.doi.org/10.1016/0920-4105(91)90066-V)
- Allthingsradon. 2009. How is radon created? <http://allthingsradon.com/tag/radioactive-decay/> (accessed Feb. 11 2016)
- Amirkhanoff, K. I., Brandt, S., and Bartnitsky, E. 1961. Radiogenic argon in minerals and its migration. *Annals of the New York Academy of Sciences* 91(2): 235-275.
- Andrews, J. N., and Wood, D. F. 1972. Mechanism of radon release in rock matrices and entry into groundwater. *Trans. Inst. Min. Metall. B* 81: 198-209.
- Anspaugh, L. R. 2012. Scientific issues concerning radon in natural gas. Texas Eastern Transmission, LP and Algonquin Gas Transmission, LLC, New Jersey–New York Expansion Project.
- Asadi, M., Woodroof, R. A., and Dumas, J. D. 2008. Post-frac analysis based on flowback results using chemical frac-tracers. Presented at the *International Petroleum Technology Conference*. Kuala Lumpur, Malaysia, 3-5 December. <http://dx.doi.org/10.2523/IPTC-11891-MS>
- Asakawa, K. 2005. *A generalized analysis of partitioning interwell tracer tests*. Ph.D dissertation, The University of Texas at Austin, Austin, Texas (December 2015).
- Barillon, R., Özgümüş, A., and Chambaudet, A. 2005. Direct recoil radon emanation from crystalline phases. Influence of moisture content. *Geochimica et cosmochimica acta* 69(11): 2735-2744.
- Benson, D. A., and Meerschaert, M. M. 2009. A simple and efficient random walk solution of multi-rate mobile/immobile mass transport equations. *Advances in Water Resources*, 32(4), 532-539.
- Bragg, J.R., Shallenberger, L.K. and Deans H.A. In-situ Determination of Residual Gas Saturation by Injection and Production of Brine. Presented at the SPE Annual Fall

- Technical Conference and Exhibition, New Orleans, Louisiana, 3-6 October. SPE-6047-MS. <http://dx.doi.org/10.2118/6047-MS>.
- Bu, P. X., AlSofi, A.M, Liu, J. et al. 2014. Simulation of single well tracer tests for surfactant–polymer flooding. *Journal of Petroleum Exploration and Production Technology*: 1-13. <http://dx.doi.org/10.1007/s13202-014-0143-9>.
- Buckley, S.E., and Leverett, M.C. 1942. Mechanism of Fluid Displacement in Sands. *Transactions of the AIME* 146 (01): 107-116. SPE-942107-G. <http://dx.doi.org/10.2118/942107-G>.
- Catlett, R. D., Spencer, J. D., Lolon, E., et al. 2013. Evaluation of two horizontal wells in the Eagle Ford using oil-based chemical tracer technology to optimize stimulation design. Presented at the SPE Hydraulic Fracturing Technology Conference, Woodlands, Texas, USA, 4-6 February. <http://dx.doi.org/10.2118/163846-MS>
- Cheng, Y. 2012. Impact of water dynamics in fractures on the performance of hydraulically fractured wells in gas-shale reservoirs. *Journal of Canadian Petroleum Technology*, 51(02): 143-151. <http://dx.doi.org/10.2118/127863-PA>.
- Chalmers, G. R., Bustin, R. M., Power, I. M. 2012. Characterization of gas shale pore systems by porosimetry, pycnometry, surface area, and field emission scanning electron microscopy/transmission electron microscopy image analyses: Examples from the Barnett, Woodford, Haynesville, Marcellus, and Doig units. *AAPG bulletin*, 96(6): 1099-1119. Doi: 10.1306/10171111052
- Chitrala, Y., Moreno, C., Songdergeld, C. H. et al. 2011. Microseismic and microscopic analysis of laboratory induced hydraulic fractures. Presented at the Canadian Unconventional Resources Conference, Calgary, Alberta, Canada, 15-17 November. <http://dx.doi.org/10.2118/147321-MS>
- Cipolla, C. L., Lolon, E. P., Erdle, J. C., et al. 2010. Reservoir modeling in shale-gas reservoirs. *SPE reservoir evaluation & engineering*, 13(04): 638-653. <http://dx.doi.org/10.2118/125530-PA>.
- Civan, F. 2011. Porous media transport phenomena. John Wiley & Sons.
- CMG-STARS User's Guide. 2012: *Computer Modeling Group Ltd*
- Cockin, A.P., Malcolm, L.T., McGuire, P.L. et al. 2000. Analysis of A Single-Well Chemical Tracer Test to Measure the Residual Oil Saturation to A Hydrocarbon Miscible Gas Flood at Prudhoe Bay. *SPE Res Eval & Eng* 3 (06): 544-551. SPE-68051-PA. <http://dx.doi.org/10.2118/68051-PA>.

- Cooke Jr., C.E. 1971. Method of Determining Fluid Saturations in Reservoirs. US Patent No. US3590923A.
- Crafton, J. W. 2008. Modeling flowback behavior or flowback equals" slowback". Presented at the SPE Shale Gas Production Conference, Fort Worth, Texas, USA, 16-18 November. <http://dx.doi.org/10.2118/119894-MS>
- Crawford, E., Senters, C. W., Bullard, K. E., et al. 2014. Granite Wash optimization-validating completion and production techniques. Presented at the SPE Annual Technical Conference and Exhibition, Amsterdam, Netherlands, 27-29 October. <http://dx.doi.org/10.2118/170923-MS>
- Davis, E. 2009. Hydraulic Fracture Diagnostics and Reservoir Diagnostics. http://www.ieaghg.org/docs/monitoring/5mtg/Pinnacle_BD%20Overview%20EJD.pdf
- Darby, S., Hill, D., Auvinen, A. et al. 2005. Radon in homes and risk of lung cancer: collaborative analysis of individual data from 13 European case-control studies. *Bmj* 330(7485), 223.
- Deans, H.A., and Carlisle, C.T. 1988. Single Well Chemical Tracer Test Handbook . *Chemical Tracers Inc.*, Houston, TX.
- Deans, H.A., and Mut, A.D. 1997. Chemical Tracer Studies to Determine Water Saturation at Prudhoe Bay. *SPE Res Eng* 12: 52-57. SPE-28591-PA. <http://dx.doi.org/10.2118/28591-PA>.
- Deans, H.A., and Shallenberger, L.K. 1974. Single Well Chemical Tracer Method to Measure Connate Water Saturation. Presented at the SPE Improved Oil Recovery Symposium, Tulsa, Oklahoma, 22-24 April. SPE-4755-MS. <http://dx.doi.org/10.2118/4755-MS>.
- Deans, H.A., and Majoros, S. 1980. Single-Well Chemical Tracer Method for Measuring Residual Oil Saturation. Final report. United States.
- Denney, D. 2011. Alkaline/Surfactant/Polymer Flood: Single Well Chemical Tracer Tests-Design, Implementation and Performance. *J Pet Technol* 63(06):86-88. SPE-0611-0086-JPT. <http://dx.doi.org/10.2118/0611-0086-JPT>.
- DOE, US. 2009. Modern shale gas development in the United States: A primer. Office of Fossil Energy and National Energy Technology Laboratory.
- EIA. 2014. Shale gas provides largest share of U.S. natural gas production in 2013. <http://www.eia.gov/todayinenergy/detail.cfm?id=18951> (accessed Feb. 11 2016)

- EPA. 2012. A citizen's guide to radon: the guide to protecting yourself and your family from radon. <http://www.epa.gov/sites/production/files/2015-05/documents/citizensguide.pdf> (accessed Feb. 11 2016)
- Elahi, S. H., and Jafarpour, B. 2015. Characterization of fracture length and conductivity from tracer test and production data with Ensemble Kalman filter. Presented at the Unconventional Resources Technology Conference, San Antonio, Texas, USA, 20-22 July. <http://dx.doi.org/10.2118/178707-MS>
- Fetzer, T. 2014. Fracking growth. Presented at the CEP Discussion Papers, London, UK, June.
- Fleischer, R. L. 1983. Theory of alpha recoil effects on radon release and isotopic disequilibrium. *Geochimica et Cosmochimica Acta* 47(4): 779-784.
- Flügge, S.; Zimens, K. 1939. The Determination of Grain Size and Diffusion Constant by the Emanation Power (The Theory of Emanation Method). *Z. Phys. Chem.* 42: 179-220.
- Gardien, C. J., Pope, G. A., and Hill, A. D. 1996. Hydraulic fracture diagnosis using chemical tracers. Presented at the SPE Annual Technical Conference and Exhibition, Denver, Colorado, 6-9 October. <http://dx.doi.org/10.2118/36675-MS>.
- Gale, J. F., and Holder, J. 2010. Natural fractures in some US shales and their importance for gas production. Geological Society, London, Petroleum Geology Conference Series 7: 1131-1140
- Gale, J. F., Laubach, S. E., Olson, J. E. et al. 2014. Natural fractures in shale: A review and new observations. *AAPG bulletin* 98(11): 2165-2216.
- Goswick, R. A., and LaRue, J. L. 2014. Utilizing oil soluble tracers to understand stimulation efficiency along the lateral. Presented at the SPE Annual Technical Conference and Exhibition, Amsterdam, Netherlands, 27-29 October. <http://dx.doi.org/10.2118/170929-MS>
- Haddad, M., Sanaei, A., Al-Shalabi, E. W., et al. 2015. Major obstacles in production from hydraulically re-fractured shale formations: reservoir pressure depletion and pore blockage by the fracturing fluid. Presented at the Unconventional Resources Technology Conference, San Antonio, Texas, USA, 20-22 July. <http://dx.doi.org/10.2118/178587-MS>
- Hammond, D. E., Leslie, B.W., Ku, T. et al. 1988. Rn concentrations in deep formation waters and the geohydrology of the Cajon Pass borehole. *Geophysical Research Letters* 15(9): 1045-1048.

- Heckter, M. 1934. Radiochemische Oberflächenbestimmung an glas. *Deutsche Glastechnische Gesellschaft* 12: 156-172.
- Jerauld, G., Mohammadi, H., and Webb, K.J. Interpreting Single Well Chemical Tracer Tests. Presented at SPE Improved Oil Recovery Symposium, Tulsa, Oklahoma, 24-28 April,. SPE-129724-MS. <http://dx.doi.org/10.2118/129724-MS>.
- Jha, R. K., Bryant, S., and Lake, L. W. 2011. Effect of diffusion on diffusion. *SPE J*, 16(01):65-77.
- Jin, L., Ahmad, J., Harwell, J.H. et al. 2015. Modeling and Interpretation of Single Well Chemical Tracer Tests (SWCTT) for pre and post Chemical EOR in two High Salinity Reservoirs. Presented at SPE Production and Operations Symposium, Oklahoma City, Oklahoma, 1-5 March. SPE-173618-MS. <http://dx.doi.org/10.2118/173618-MS>.
- John, A. K., Lake, L. W., Bryant, S. et al. 2010. Investigation of mixing in field-scale miscible displacements using particle-tracking simulations of tracer floods with flow reversal. *SPE J*, 15(03):598-609.
- King, G. E., and Leonard, D. 2011. Deciphering chemical tracer results in multi-fractured well backflow in shales: A framework for optimizing fracture design and application. Presented at the SPE Hydraulic Fracturing Technology Conference and Exhibition, the Woodlands, 24-26 January. <http://dx.doi.org/10.2118/140105-MS>
- Kondash, A. J., Warner, N. R., Lahav, O. et al. 2013. Radium and barium removal through blending hydraulic fracturing fluids with acid mine drainage. *Environmental science & technology* 48(2): 1334-1342
- LaBolle, E. M., Fogg, G. E., and Tompson, A. F. 1996. Random-walk simulation of transport in heterogeneous porous media: Local mass-conservation problem and implementation methods. *Water Resources Research*, 32(3): 583-593.
- Langmuir, I. 1918. The adsorption of gases on plane surfaces of glass mica and platinum. *J. Am. Chem. Soc.* 40:1361-1403.
- Leong, Y., de Iongh, J. E., Bähring, S., et al. 2015. Estimation of fracture volume between well pairs using deuterium tracer. Presented at the SPE Annual Technical Conference and Exhibition. Houston, Texas, USA, 28-30 September. <http://dx.doi.org/10.2118/174832-MS>
- Liu, H. H., Bodvarsson, G. S., and Pan, L. 2000. Determination of particle transfer in random walk particle methods for fractured porous media. *Water Resources Research*, 36(3): 707-713.

- Liu, J., Parker, E. D., and Camilleri, D. 1999. A new particle tracking algorithm for tracer flow simulation. Presented at the SPE Reservoir Simulation Symposium, Houston, Texas, 14-17 February.
- Maroongroge, V. 1994. *Modeling and application of tracers for reservoir characterization*. Ph.D dissertation, The University of Texas at Austin, Austin, Texas.
- Medeiros, F., Ozkan, E., and Kazemi, H. 2008. Productivity and drainage area of fractured horizontal wells in tight gas reservoirs. *SPE Res Eval & Eng* 11(05): 902-911. SPE-108110-PA.
- Montgomery, C. T., Smith, M. B. Hydraulic Fracturing: History of an enduring technology. *Journal of Petroleum Technology* 2010 62(12):26-40; doi: 10.2118/1210-0026-JPT
- Mosher, K., He, J., Liu, Y. et al. 2013. Molecular simulation of methane adsorption in micro-and mesoporous carbons with applications to coal and gas shale systems. *International Journal of Coal Geology* 109: 36-44
- NCI. 2011. Radon and cancer. <http://www.cancer.gov/cancertopics/factsheet/Risk/radon> (accessed Feb. 11 2016)
- Nelson, A. W., May, D., Knight, A. W. et al. 2014. Matrix complications in the determination of radium levels in hydraulic fracturing flowback water from Marcellus Shale. *Environmental Science & Technology Letters* 1(3): 204-208
- Newman, A.; Thomasson. 1979. A rothamsted studies of soil structure III. *Journal of Soil Science* 30(3): 415-439.
- Nielson, K., Rogers, V., Gee, G. 1984. Diffusion of radon through soils: a pore distribution model. *Soil Science Society of America Journal* 48(3): 482-487.
- Nierenberg, W.A. 1992. *Encyclopedia of Earth System Science*. San Diego, CA (US): Academic Press, Inc.
- Oyerinde, A. S. 2005. *A composite tracer analysis approach to reservoir characterization*. Ph.D dissertation, Texas A&M University.
- Park, Y.J., and Deans, H.A., and Tezduyar, T.E. 1991. Thermal Effects on Single-Well Chemical-Tracer Tests for Measuring Residual Oil Saturation. *SPE Form Eval* 6 (03): 401-408. SPE-19683-PA. <http://dx.doi.org/10.2118/19683-PA>.
- Passey, Q. E., Bohacs, K., Esch, W. L. et al. 2010. From oil-prone source rock to as-producing shale reservoir—geologic and petrophysical characterization of

- unconventional shale-gas reservoirs. Presented at the International Oil and Gas Conference and Exhibition, Beijing, China, 8-10 June. SPE-131350-MS.
- Peters, E.J. 2012. *Advanced petrophysics: Volume 2: Dispersion, Interfacial Phenomena/Wettability, Capillarity/Capillary Pressure, Relative Permeability*, first edition. Austin, Texas: Greenleaf Book Group.
- Resnikoff, M. 2011. Radon in natural gas from marcellus shale. *Ethics in Biology, Engineering and Medicine* 2(4): 317-331.
- Rowan, E. L., and Kraemer, T. 2012. Radon-222 Content of natural gas samples from Upper and Middle Devonian sandstone and shale reservoirs in Pennsylvania: Preliminary data. Open-File Report, US Geological Survey.
- Sasaki, T., Gunji, Y., and Okuda, T. 2014. Mathematical modeling of radon emanation. *Journal of nuclear science and technology* 41(2): 142-151.
- Sakhaee-Pour, A., and Wheeler M. F. 2015. Effective flow properties for cells containing fractures of arbitrary geometry. SPE J. SPE-167183-PA. (in press; posted August 2015).
- Scheidegger, A. E. 1954. Statistical hydrodynamics in porous media. *Journal of Applied Physics*, 25(8): 994-1001.
- Sharma, A., Shook, G. M., and Pope, G. A. 2014. Rapid analysis of tracers for use in EOR flood optimization. Presented at the SPE Improved Oil Recovery Symposium, Tulsa, Oklahoma, USA, 12-16 April. <http://dx.doi.org/10.2118/169109-MS>
- Sheely Jr, C. Q., and Baldwin Jr, D. E. 1982. Single-well tracer tests for evaluating chemical enhanced oil recovery processes. *Journal of Petroleum Technology*, 34(08): 1887-1896. <http://dx.doi.org/10.2118/8838-PA>.
- Shen, T., Rouzbeh, G. M., and Tian, W. 2016. Contribution of Dispersion and Permeability Variation on Propagation of Tracer Concentration in Permeable Media. Presented at the International Petroleum Technology Conference, Bangkok, Thailand, 13-16 November. IPTC-18954-MS.
- Shen, T., Rouzbeh, G. M., and Tian, W. 2017. Interpretation of Interwell Chemical Tracer Tests in Layered Heterogeneous Reservoirs with Crossflow. Presented at the SPE ATCE, San Antonio, Texas, 9-11 October. SPE-187400-MS.
- Shook, G. M., Ansley, S.L., and Wylie, A. 2004. Tracers and Tracer Testing: Design, Implementation, and Interpretation Methods. DOI, 10, 910642.
- Shook, G.M., Pope, G.A., and Asakawa, K. 2009. Determining Reservoir Properties and Flood Performance from Tracer Test Analysis. Presented at SPE Annual Technical

- Conference and Exhibition, New Orleans, Louisiana, 4-7 October. SPE-124614-MS. <http://dx.doi.org/10.2118/124614-MS>.
- Sobieski, W., and Trykozko, A. 2014. Darcy's and Forchheimer's laws in practice. Part 1. The experiment. Technical Sciences/University of Warmia and Mazury in Olsztyn.
- Stalgorova, E., and Babadagli, T. 2012. Modeling miscible injection in fractured porous media using random walk simulation. *Chemical Engineering Science*, 74: 93-104.
- Sun, J., and Schechter, D. S. 2015. Optimization-Based Unstructured Meshing Algorithms for Simulation of Hydraulically and Naturally Fractured Reservoirs with Variable Distribution of Fracture Aperture, Spacing, Length and Strike. *SPE Reservoir Evaluation & Engineering*, 18 (04):463-480. <http://dx.doi.org/10.2118/170703-PA>.
- Tang, J. S., and Harker, B. 1990. Mass Balance Method to Determine Residual Oil Saturation from Single Well Tracer Test Data. *Journal of Canadian Petroleum Technology* 29(02). PETSOC-90-02-08. <http://dx.doi.org/10.2118/90-02-08>.
- Tang, J.S. 1995. Partitioning Tracers and In-situ Fluid-Saturation Measurements. *SPE Form Eval* 10(01): 33-39. SPE-22344-PA. <http://dx.doi.org/10.2118/22344-PA>.
- Tang, J. S., and Zhang, P. 2000. Effect of Mobile Oil on Residual Oil Saturation Measurement by Interwell Tracing Method. Presented at International Oil and Gas Conference and Exhibition, Beijing, China, 7-10 November. SPE-64627-MS. <http://dx.doi.org/10.2118/64627-MS>.
- Tanner, A. B. 1980. Radon migration in the ground: a supplementary review. *Natural radiation environment III* 1: 5-56.
- Tomich, J. F., Dalton Jr, R. L., Deans, H. A., et al. 1973. Single-well tracer method to measure residual oil saturation. *Journal of Petroleum Technology*, 25(02): 211-218. <http://dx.doi.org/10.2118/3792-PA>
- USGS. 2012. *Radon-222 Content of natural gas samples from Upper and Middle Devonian sandstone and shale reservoirs in Pennsylvania: Preliminary data*. Highlights of Open- file report series 2012-1159; U.S. Geological Survey: Reston, Virginia; <http://pubs.usgs.gov/of/2012/1159>.
- Wang, C., Yao, J., Wu, K., et al. 2014. Organic and inorganic pore structure analysis in shale matrix with superposition method. Presented at the Unconventional Resources Technology Conference, Denver, Colorado, USA, 25-27 August. <https://doi-org.ezproxy.lib.ou.edu/10.15530/URTEC-2014-1922283>.

- Warpinski, N. R., Branagan, P. T., Peterson, R. E., et al. 1998. Mapping hydraulic fracture growth and geometry using microseismic events detected by a wireline retrievable accelerometer array. Presented at the SPE Gas Technology Symposium, Calgary, Alberta, Canada, 15-18 March. <http://dx.doi.org/10.2118/40014-MS>.
- Weigel, F. 1978. RADON. *Chemiker-Zeitung* 9: 287-299.
- Wellington, S.L., and Richardson, E.A. 1994. Redesigning Ester Single-Well Tracer Test that Incorporates pH-Driven Hydrolysis Rate Changes. *SPE Res Eng* 9 (04): 233-239. SPE-24135-PA. <http://dx.doi.org/10.2118/24135-PA>.
- Wu, X. 2006. *An investigation of partitioning chemical tracers for characterizing geothermal reservoirs and predicting enthalpy production*. Ph.D dissertation, The University of Texas at Austin, Austin, Texas.
- Yi, T., Daltaban, T. S., and Dawe, R. A. 1994. Prediction of interwell tracer flow behaviour in heterogeneous reservoirs. *Transport in porous media*, 17(1): 59-75.

Appendix A: Derivation of Modified MoM

The derivation of our proposed MoM follows Asakawa (2005), but it is modified for the new SWCTT. The mass conservation equation of a tracer component k anywhere in the reservoir free of tracer decay, adsorption and reaction is expressed by

$$\frac{\partial}{\partial t} (\phi \sum_{i=1}^2 S_i C_{ki}) + \nabla \cdot \vec{N}_k = 0 \quad (\text{A-1})$$

Where C_{kl} is the concentration of k in phase l (subscript 1 for water and 2 for oil), and \vec{N}_k is the total flux of the tracer component k , including both the convection and dispersion. The expression is

$$\vec{N}_k = \sum_{i=1}^2 (C_{ki} \vec{u}_i - \phi S_i \vec{K} \cdot \nabla C_{ki}) \quad (\text{A-2})$$

The first term in the right hand side is mass conservation equation and the second in the right hand side is the transport term in Eq. A-1.

If the porosity is constant, Eq. A-1 can be transformed to

$$\phi \frac{\partial}{\partial t} C_k + \nabla \cdot \vec{N}_k = 0 \quad (\text{A-3})$$

Where C_k is the overall fluid phase concentration of the tracer k , and it is defined as:

$$C_k = \sum_{i=1}^2 S_i C_{ki} \quad (\text{A-4})$$

Replacing t in Eq. A-3 by τ for integration

$$\phi \frac{\partial}{\partial \tau} C_k + \nabla \cdot \vec{N}_k = 0 \quad (\text{A-5})$$

Multiplying above equation by time τ and to obtain the first temporal moment and integrating it from 0 to t gives

$$\int_0^t \tau \phi \frac{\partial C_k}{\partial \tau} d\tau + \int_0^t \tau \nabla \cdot \vec{N}_k d\tau = 0 \quad (\text{A-6})$$

Since porosity is constant and switching the order of the time integration and the delta operator in the second term, Eq. A-6 is rewritten as

$$\phi \int_0^t \tau \frac{\partial C_k}{\partial \tau} d\tau + \nabla \cdot \int_0^t \tau \overrightarrow{N_k} d\tau = 0 \quad (\text{A-7})$$

Now, integrate the first term

$$\int_0^t \tau \frac{\partial C_k}{\partial \tau} d\tau = \int_0^t \left(\frac{\partial(\tau C_k)}{\partial \tau} - C_k \right) d\tau = [\tau C_k]_0^t - \int_0^t C_k d\tau \quad (\text{A-8})$$

Assuming that the initial concentration is zero, the first term in Eq. A-7 becomes

$$\phi \int_0^t \tau \frac{\partial C_k}{\partial \tau} d\tau = -\phi \left[-t C_{k,\tau=t} + \int_0^t C_k d\tau \right] \quad (\text{A-9})$$

The Eq. (A-7) comes to

$$-\phi \left[-t C_{k,\tau=t} + \int_0^t C_k d\tau \right] + \nabla \cdot \int_0^t \tau \overrightarrow{N_k} d\tau = 0 \quad (\text{A-10})$$

Multiplying Eq. A-5 by time t and integrate it from t to infinity gives

$$\int_t^\infty t \phi \frac{\partial C_k}{\partial \tau} d\tau + \int_t^\infty t \nabla \cdot \overrightarrow{N_k} d\tau = 0 \quad (\text{A-11})$$

Similarly, the first term can be integrated as

$$\int_t^\infty t \frac{\partial C_k}{\partial \tau} d\tau = t \int_0^\infty dC_k = t[C_k]_{\tau \rightarrow \infty} - t[C_k]_{\tau=t} \quad (\text{A-12})$$

When time goes to infinite, then, C_k is zero, hence above equation turns to

$$\int_t^\infty t \frac{\partial C_k}{\partial \tau} d\tau = -t[C_k]_{\tau=t} \quad (\text{A-13})$$

Now, the Eq. A-11 becomes as

$$-\phi t C_{k,\tau=t} + \nabla \cdot \int_t^\infty t \overrightarrow{N_k} d\tau = 0 \quad (\text{A-14})$$

Combining Eq. A-14 and Eq. A-10,

$$-\phi \left[-t C_{k,\tau=t} + \int_0^t C_k d\tau \right] + \nabla \cdot \int_0^t \tau \overrightarrow{N_k} d\tau + (-\phi t C_{k,\tau=t} + \nabla \cdot \int_t^\infty t \overrightarrow{N_k} d\tau) = 0 \quad (\text{A-15})$$

Rearranging the equation yields:

$$-\phi \int_0^t C_k d\tau + \nabla \cdot \int_0^t \tau \overline{N}_k d\tau + \nabla \cdot \int_t^\infty \tau \overline{N}_k d\tau = 0 \quad (\text{A-16})$$

Defining zeroth temporal moment of tracer concentration:

$$m_{0k} = \int_0^t C_k d\tau \quad (\text{A-17})$$

With this, Eq. A-16 is transformed as:

$$-\phi m_{0k} + \nabla \cdot \int_0^t \tau \overline{N}_k d\tau + \nabla \cdot \int_t^\infty \tau \overline{N}_k d\tau = 0 \quad (\text{A-18})$$

Integrating Eq. A-18 in the domain swept by the tracer gives:

$$-\iiint \phi m_{0k} dV_R + \iiint \left(\nabla \cdot \int_0^t \tau \overline{N}_k d\tau + \nabla \cdot \int_t^\infty \tau \overline{N}_k d\tau \right) dV_R = 0 \quad (\text{A-19})$$

Applying Gauss theorem, Eq. A-19 can be written as:

$$-\iiint \phi m_{0k} dV_R + \iint \left(\int_0^t \tau \overline{N}_k d\tau + \int_t^\infty \tau \overline{N}_k d\tau \right) \cdot \vec{n} dA = 0 \quad (\text{A-20})$$

The second term is only calculated at the well since there is no other tracer mass transfer in other places. For this sake, the second term on the left side of above equation can be written as

$$\begin{aligned} & \iint \left(\int_0^t \tau \overline{N}_k d\tau + \int_t^\infty \tau \overline{N}_k d\tau \right) \cdot \vec{n} dA \\ &= \iint \left(\int_0^t \tau \overline{N}_k d\tau \right) \cdot \vec{n} dA + \iint \left(\int_t^\infty \tau \overline{N}_k d\tau \right) \cdot \vec{n} dA \end{aligned} \quad (\text{A-21})$$

Assuming there is no diffusion and combining with Eq. A-2, Eq. A-21 is further revised as

$$\begin{aligned} & \iint \left(\int_0^t \tau \overline{N}_k d\tau \right) \cdot \vec{n} dA + \iint \left(\int_t^\infty \tau \overline{N}_k d\tau \right) \cdot \vec{n} dA \\ &= \int_0^t q\tau \left(\sum_{l=1}^2 \frac{q_l C_{kl}}{q} \right) d\tau + \int_t^\infty q\tau \left(\sum_{l=1}^2 \frac{q_l C_{kl}}{q} \right) d\tau \end{aligned} \quad (\text{A-22})$$

Define

$$m_{1k} = \int_0^t \tau \left(\sum_{l=1}^2 \frac{q_l C_{kl}}{q} \right) d\tau = \int_0^t \tau \left(\sum_{l=1}^2 f_l C_{kl} \right) d\tau \quad (\text{A-23})$$

$$\tilde{m}_{1k} = \int_0^\infty t \left(\sum_{l=1}^2 \frac{q_l c_{kl}}{q} \right) d\tau = \int_0^\infty t \left(\sum_{l=1}^2 f_l c_{kl} \right) d\tau \quad (\text{A-24})$$

Where

$$f_l = \frac{q_l}{q} \quad (\text{A-25})$$

$l = 1$ stands for water and $l = 2$ is oil, respectively.

Substituting Eq. A-23 and A-24 into A-22 get

$$\int_0^t q\tau \left(\sum_{l=1}^2 \frac{q_l c_{kl}}{q} \right) d\tau + \int_t^\infty q\tau \left(\sum_{l=1}^2 \frac{q_l c_{kl}}{q} \right) d\tau = q(m_{1k} + \tilde{m}_{1k}) \quad (\text{A-26})$$

Subsequently, Eq. A-20 can be written as

$$- \iiint \phi m_{0k} dV_R + q(m_{1k} + \tilde{m}_{1k}) = 0 \quad (\text{A-27})$$

This equation can be obtained only at the well. The information of the pore volume and the saturation is imbedded in the left hand term. Also, this formula is for multiphase flow.

Let water phase be the reference phase. Define partition coefficient

$$K_l = \frac{C_{kl}}{C_{k1}} \quad (l = 1, 2) \quad (\text{A-28})$$

With Eq. (A-28) only the water phase could be used to describe Eq. A-17

$$m_{0k} = \int_0^t C_k d\tau = \int_0^t \left(\sum_{l=1}^2 S_l C_{kl} \right) d\tau = \left(\sum_{l=1}^2 K_l \hat{S}_l \right) m_{0k1} \quad (\text{A-29})$$

Where

$$\hat{S}_l = \frac{\left(\int_0^t (S_l C_{k1}) d\tau \right)}{\left(\int_0^t C_{k1} d\tau \right)} \quad (\text{A-30})$$

And

$$m_{0k1} = \int_0^t C_{k1} d\tau \quad (\text{A-31})$$

Hence, Eq. A-27 can be re-written as

$$- \iiint \left(\phi \left(\sum_{l=1}^2 K_l \hat{S}_l \right) m_{0k1} \right) dV_R + q(m_{1k} + \tilde{m}_{1k}) = 0 \quad (\text{A-32})$$

q is the constant total production rate.

Define new term

$$\bar{m}_{0k1} = \int_0^{\infty} f_1 C_{k1} d\tau \quad (\text{A-33})$$

Switching the order of integration and combining Eq. A-33, Eq. A-32 turns to

$$-(\sum_{l=1}^2 K_l) \iiint \left(\phi \hat{S}_l \frac{m_{0k1}}{\bar{m}_{0k1}} \right) dV_R + q \left(\frac{m_{1k} + \tilde{m}_{1k}}{\bar{m}_{0k1}} \right) = 0 \quad (\text{A-34})$$

Substituting '1' and '2' to 'w' and 'o', Eq. A-34 becomes to

$$-\left[\iiint \left(\phi \hat{S}_w \frac{m_{0kw}}{\bar{m}_{0kw}} \right) dV_R + K_o \iiint \left(\phi \hat{S}_o \frac{m_{0kw}}{\bar{m}_{0kw}} \right) dV_R \right] + q \left(\frac{m_{1k} + \tilde{m}_{1k}}{\bar{m}_{0kw}} \right) = 0 \quad (\text{A-35})$$

For a conservative tracer, how much water is contacted at any given time t is given

$$V_w = \iiint \left(\phi \hat{S}_w \frac{m_{0kw}}{\bar{m}_{0kw}} \right) dV_R = q \left(\frac{m_{1k} + \tilde{m}_{1k}}{\bar{m}_{0kw}} \right) \quad (\text{A-36})$$

For a tracer with partition coefficient equals to 1, and knowing that $\hat{S}_o + \hat{S}_w = 1$

The pore volume contacted at time t

$$V_{\text{swept}} = \iiint \left(\phi \frac{m_{0kw}}{\bar{m}_{0kw}} \right) dV_R = q \left(\frac{m_{1k} + \tilde{m}_{1k}}{\bar{m}_{0kw}} \right) \quad (\text{A-37})$$

The residence time can be obtained by

$$\bar{t}_k = \lim_{t \rightarrow \infty} \left(\frac{m_{1k} + \tilde{m}_{1k}}{\bar{m}_{0kw}} \right) = \frac{\int_0^{\infty} \tau (\sum_{l=1}^2 f_l C_{kl}) d\tau}{\bar{m}_{0kw}} \quad (\text{A-38})$$

In SWCTT, the swept pore volume of two tracers with different partition coefficient may be different. Therefore, a ratio R is introduced here

$$R = \frac{V_{\text{swept,tracer 1}}}{V_{\text{swept,tracer 2}}} \quad (\text{A-39})$$

Hence, for two tracers whose partition coefficients between oil and water are K_1 and K_2

$$R \cdot \hat{V}_w + R \cdot K_1 \hat{V}_o = q \bar{t}_1 \quad (\text{A-40})$$

$$\widehat{V}_w + K_2 \widehat{V}_0 = q \bar{t}_2 \quad (\text{A-41})$$

Then,

$$\widehat{V}_0 = \frac{q(R \cdot \bar{t}_2 - \bar{t}_1)}{R \cdot (K_2 - K_1)} \quad (\text{A-42})$$

$$\widehat{V}_w = \frac{q(K_2 \bar{t}_1 - R \cdot K_1 \bar{t}_2)}{R \cdot (K_2 - K_1)} \quad (\text{A-43})$$

$$V_P = \widehat{V}_w + \widehat{V}_0 = \frac{q((K_2 - 1) \bar{t}_1 - R \cdot (K_1 - 1) \bar{t}_2)}{R \cdot (K_2 - K_1)} \quad (\text{A-44})$$

The average oil saturation can be calculated from

$$S_o = \frac{R \cdot \bar{t}_2 - \bar{t}_1}{(K_2 - 1) \bar{t}_1 - R \cdot (K_1 - 1) \bar{t}_2} \quad (\text{A-45})$$

If there is one active partitioning tracer and one conservative tracer, Eq. A-45 is going to be:

$$S_o = \frac{R \cdot \bar{t}_2 - \bar{t}_1}{(K_2 - 1) \bar{t}_1 + R \cdot \bar{t}_2} \quad (\text{A-46})$$

Appendix B: Simulation Input File for SWCTT

RESULTS SIMULATOR STARS 200500

*interrupt *stop

*INUNIT *FIELD

TITLE1 'SWTT Model'

TITLE2 'SWCTT'

TITLE3 'Single layer'

*wrst

WPRN SECTOR TIME

OUTPRN WELL ALL

WSRF SECTOR TIME

WSRF WELL TIME

*OUTSRF *GRID *ALL

OUTSRF SPECIAL MASSFRAC 'PRODUC' 'MeOH' WATER

OUTSRF SPECIAL MASSFRAC 'PRODUC' 'PrOH' WATER

OUTSRF SPECIAL MASSFRAC 'PRODUC' 'EtFm' WATER

OUTSRF SPECIAL MASSFRAC 'PRODUC' 'EtFm' OIL

OUTSRF SPECIAL MASSFRAC 'PRODUC' 'EtAl' WATER

OUTSRF SPECIAL MASSFRAC 'INJECT' 'MeOH' WATER

OUTSRF SPECIAL MASSFRAC 'INJECT' 'PrOH' WATER

OUTSRF SPECIAL MASSFRAC 'INJECT' 'EtFm' WATER

** WPRN WELL TIME (not supported by stars)

**\$ Distance units: ft

RESULTS XOFFSET 0.0000

RESULTS YOFFSET 0.0000

RESULTS ROTATION 0.0000 **\$ (DEGREES)

RESULTS AXES-DIRECTIONS 1.0 -1.0 1.0

**\$

**\$ Definition of fundamental cylindrical grid

**\$

GRID RADIAL 737 1 1 *RW 0.2

DI IVAR 700*0.1

1.944425195 2.61543928 2.89253235 3.19898209 3.53789868 3.91272184

4.32725569 4.78570738 5.2927298 9.790447 38.04171 60.29205 95.55647

151.4468 240.027

380.4171 546.178423 20*1000

SECTOR 'SWTT' 1:10 1 1

DJ JVAR 360

DK CON 16

KDIR DOWN

DEPTH TOP 1 1 1 6415 ** depth of top is constant at 6415

NULL CON 1

POR CON 0.19

PERMI CON 1000.

PERMJ CON 1000.

PERMK CON 1000.

PINCHOUTARRAY CON 1

END-GRID

ROCKTYPE 1

*MODEL 8 8 8 6 ** 8 total components, 8 fluid , 8 liquid , 6 aqueous

*COMPNAME 'Water' 'NaCl' 'MeOH' 'PrOH' 'EtFm' 'EtAl' 'Dead_Oil'
'Soln_Gas'

** -----

*CMM 0.0000 58.4400 60.096 60.096 66.00 46.069 299.8980
24.3930 ** Component MW

*PCRIT 0.00 0.00 0.00 0.00 0.00 0.00 225.04 764.99 **
Component critical pressure (kPa | psi | kPa).

*TCRIT 0.00 0.00 0.00 0.00 0.00 0.00 975.87 -32.16 **
Component critical temperature (C | F | C)

*KV1 0.000E+0 0.0000 0.00 0.00 0.00 0.00 2.843E+6 2.375E+5
*KV2 0.000E+0 0.0000 0.00 0.00 0.00 0.00 0.000E+0 0.000E+0
*KV3 0.000E+0 0.0000 0.00 0.00 0.00 0.00 0.000E+0 0.000E+0
*KV4 0.000E+0 0.0000 0.00 0.00 0.00 0.00 -13557.5 -2453.1
*KV5 0.000E+0 0.0000 0.00 0.00 0.00 0.00 -459.67 -459.67

*MOLDEN 0.000E+00 0.0000 0.00 0.00 0.00 0.00 0.00 1.969E-01
9.784E-01 ** Molar density at reference pressure and temperature

*CP 0.000E+00 0.0000 0.00 0.00 0.00 0.00 3.507E-06 2.632E-05
** Liquid compressibility (1/kPa | 1/psi) at constant temperature

*CT1 0.000E+00 0.0000 0.00 0.00 0.00 0.00 1.688E-04 1.110E-03
** thermal expansion correlation (1/C | 1/F).

*AVISC 0.0500 3713.8 0.0294906 0.05496736 0.1634264 0.102069 2.469E-
01 3.916E-01 ** visc=avisc*exp(-bvisc/T)

*BVIS 1184.85 1659.8 2051.46 1711.872 769.284 1235.952 1389.43
210.37

*SURFLASH *KVALUE
** K_SURF is the k value between liquid and gas
*K_SURF 'EtAl' 0
*K_SURF 'EtFm' 0
*K_SURF 'MeOH' 0
*K_SURF 'PrOH' 0
*K_SURF 'Water' 0

*PRSR 4925.0 ** reference pressure, corresponding to the density
*TEMR 219.0 ** reference temperature, corresponding to the density

*PSURF 14.7 ** pressure at surface, for reporting well rates, etc.

*TSURF 60.0 ** temperature at surface, for reporting well rates, etc.

*LIQLIQKV ** Flag for liquid-liquid k-values, $K_{ow}=x_i/w_i >0$ usually in the range of 2.0 to 8.0

*KVABLIM 14 9000 60 220 ** plow phigh Tlow Thigh

*KVTABLE 'EtFm' ** Multiply usual mass based k-value by $MW_{oil}/MW_{water}=7$

25.62 25.62

25.62 25.62

*RPHASE 0 0 0 0 1 1 0 0

*RORDER 0 0 0 0 1 1 0 0

** 'WATER' 'NaCL' 'MeOH' 'PrOH' 'EtFm' 'EtAl' 'oil' 'gas'

*STOREAC 0 0 0 0 1 0 0 0

*STOPROD 0 0 0 0 0 1 0 0

*FREQFAC 1.0 **units are 1/day 0.0136 for first test and 0.0089 for the second test, reaction rate

*ROCKFLUID

*RPT 1 *WATWET *STONE2

*SWT

0.0500 0.000E+00 1.000E+00 0

0.0755 2.100E-03 9.070E-01 0

0.1491 1.010E-02 7.260E-01 0

0.2574 3.250E-02 4.650E-01 0

0.3462 6.400E-02 2.740E-01 0

0.4208 1.060E-01 1.390E-01 0

0.5035 1.610E-01 4.940E-02 0

0.5791 2.550E-01 1.270E-02 0

0.5842 2.590E-01 1.080E-02 0

0.6057 2.990E-01 7.000E-03 0
0.6333 3.670E-01 3.900E-03 0
0.6496 4.170E-01 1.600E-03 0
0.6966 5.920E-01 8.500E-04 0
0.7201 6.930E-01 4.200E-04 0
0.7365 7.750E-01 2.300E-04 0
0.7538 8.690E-01 1.300E-04 0
0.7691 9.900E-01 5.506E-05 0
0.8774 9.990E-01 0.000E+00 0
1.0000 1.000E+00 0.000E+00 0

*SLT

0.050000 1.000 0 0
0.299998 0.507 0 0
0.349999 0.336 0.00049 0
0.396003 0.201 0.00126 0
0.454996 0.093 0.00372 0
0.510001 0.0644 0.00676 0
0.564001 0.0404 0.0138 0
0.592000 0.0285 0.0174 0
0.618001 0.0223 0.0234 0
0.646 0.0142 0.0355 0
0.672001 0.0105 0.0537 0
0.715 0.00645 0.0974 0
0.761003 0.00332 0.129 0
0.800998 0.00194 0.214 0
0.860996 0.00126 0.404 0
0.949998 0.000454 0.786 0
1 0 1 0

*** total dispersion this is wrong.

RESULTS SECTION ROCKARRAYS

```

**MDSPI_WAT CON 0.2
**MDSPJ_WAT CON 0.2
**MDSPK_WAT CON 0.2
**MDSPI_OIL CON 0.2
**MDSPJ_OIL CON 0.2
**MDSPK_OIL CON 0.2
*KRTYPE con 1

*INITIAL
*VERTICAL *DEPTH_AVE
**$ Data for PVT Region 1
**$ -----
*INITREGION 1
*REFPRES 4925.
REFDEPTH 6430.
*DWOC 7000.0
**$ Property: Water Saturation Max: 0.05 Min: 0.05
SW CON 0.1

MFRAC_OIL 'Dead_Oil' CON 1
MFRAC_OIL 'Soln_Gas' CON 0
MFRAC_WAT 'Water' CON 1.00000 ** Molefraction
MFRAC_WAT 'NaCl' CON 0.0000 ** Molefraction
MFRAC_WAT 'MeOH' CON 0.0000 ** Molefraction
MFRAC_WAT 'PrOH' CON 0.0000 ** Molefraction
MFRAC_WAT 'EtFm' CON 0.0000 ** Molefraction
MFRAC_WAT 'EtAl' CON 0.0000 ** Molefraction

*NUMERICAL
*MAXSTEPS 999999999
*SDEGREE *GAUSS

```

*MAXPRES 1.450377E+05

*TFORM *ZT

*ISOTHERMAL

*AIM STAB

RUN

DATE 2011 01 01 ** year month day

DTWELL 0.00001

WELL 1 'PRODUC' vert 1 1

** rad geofac wfrac skin

GEOMETRY *K 0.2 0.5 1.0 0.0

PRODUCER 'PRODUC'

OPERATE MIN BHP 1200.0 CONT

OPERATE MAX STL 550.0 CONT

** liquid rate in bbl/day

perfv geo 'PRODUC' ** k ff

1 1.

SHUTIN 'PRODUC'

DTMAX 0.1

**TIME 0.1

**TIME 0.5

**TIME 1.0

**DTWELL 0.00001

**DTMAX 0.1

**

WELL 2 'INJECT' vert 1 1

** rad geofac wfrac skin

GEOMETRY *K 0.2 0.5 1.0 0.0

INJECTOR *MOBWEIGHT 'INJECT'

INCOMP WATER 0.0346 0.00 0.0016 0.0013 0.0025 0.0 0.96 0.0

perfv geo 'INJECT' ** k ff

1 1.

INJECTOR *MOBWEIGHT 'INJECT'

INCOMP WATER-OIL 0.0346 0.00 0.0016 0.0013 0.0025 0.0 0.96 0.0

OPERATE MAX BHP 9999.0 CONT

OPERATE MAX STF 550.0 CONT

TIME 0.01

TIME 0.02

TIME 0.03

TIME 0.04

TIME 0.05

TIME 0.06

TIME 0.07

TIME 0.08

DTWELL 0.00001

DTMAX 0.002

**Composition of Pusher

INJECTOR *MOBWEIGHT 'INJECT'

INCOMP WATER-OIL 0.035 0.00 0.0003 0.0 0.0 0.0 0.962 0.0

OPERATE MAX BHP 9999.0 CONT

OPERATE MAX STF 550.0 CONT

TIME 0.310909

TIME 0.332727

**

** Shut in period, shut in for 1 days

**

SHUTIN 'INJECT'

TIME 0.5

TIME 0.75

TIME 1.0

TIME 1.332727

**

** Produce back the tracers

**

DTWELL 0.00001

PRODUCER 'PRODUC'

OPERATE MIN BHP 1200.0 CONT

OPERATE MAX STL 820.00 CONT

** liquid rate in bbl/day

OPEN 'PRODUC'

TIME 1.34

TIME 1.36

TIME 1.38

. .

. .

. 0

TIME 4

Stop